STRAIN DEPENDENT PROPERTIES, INTERCALATION AND ADSORPTION STUDIES OF GRAPHENE LIKE TWO DIMENSIONAL SiC AND SiB

Thesis

submitted in partial fulfillment of the requirements for the degree of

DOCTOR OF PHILOSOPHY

by

MANJU M. S.

DEPARTMENT OF PHYSICS

NATIONAL INSTITUTE OF TECHNOLOGY KARNATAKA,

SURATHKAL, MANGALORE - 575 025

January, 2021

DECLARATION

By the Ph.D Research Scholar

I hereby *declare* that the Research Thesis entitled **"STRAIN DEPENDENT PROPERTIES, INTERCALATION AND ADSORPTION STUDIES OF GRAPHENE LIKE TWO DIMENSIONAL SiC AND SiB"**, which is being submitted to the *National Institute of Technology Karnataka, Surathkal* in partial fulfillment of the requirements for the award of the Degree of *Doctor of Philosophy* in *Physics* is a *bonafide report of the research work carried out by me*. The material contained in this thesis has not been submitted to any University or Institution for the award of any degree.

Manju M. S.
Register No.: 135037PH13F02
Department of Physics
National Institute of Technology Karnataka Surathkal.

Place: NITK - Surathkal

Date: 14/01/2021

CERTIFICATE

This is to *certify* that the Research Thesis entitled **"STRAIN DEPENDENT PROP-ERTIES, INTERCALATION AND ADSORPTION STUDIES OF GRAPHENE LIKE TWO DIMENSIONAL SiC AND SiB"**, submitted by **Manju M. S.** (Register Number: 135037PH13F02) as the record of the research work carried out by her, is *accepted* as the *Research Thesis submission* in partial fulfillment of the requirements for the award of degree of ***Doctor of Philosophy***.

Dr. Ajith K. M.
Research Guide
Head & Associate Professor
Department of Physics
NITK Surathkal - 575025

Chairman - DRPC
(Signature with Date and Seal)

Dedicated to Valsa sir whose loss have created a void but will always be remembered and cherished

ACKNOWLEDGEMENT

Finally I express my gratitude to all of whom directly or indirectly contributed to my research and made this happen.

Manju M. S.

ABSTRACT

This thesis reports the variation in properties of graphene like two dimensional materials SiC and SiB with the application of strain and their properties in being the anode of rechargeable Li-ion batteries. The material was modelled and the calculations were carried out using Density Functional Theory (DFT) using Vienna Ab-initio Simulation Package (VASP) and Quantum Espresso packages. SiC in its pristine case showed isotropic behaviour but the inducing of stress changed it to anisotropic behaviour. On the other hand, SiB was anisotropic in its pristine form and anisotropic behaviour increased with the application of strain. Both the structures were mechanically stable satisfying the Born criteria. The mechanical behaviours showed highly non-linear nature for the case of SiB and the ultimate stress were much higher than their counterpart silicene. The application of strain specifically biaxial onto SiB generated a new structure having a planar architecture very similar to graphene. The experimental synthesis of SiC urged to check its potential in being the anode of Li-ion batteries. Pristine SiC was a poor candidate and was introduced with defects to check for improvement in properties for an anode. Bi vacancy defective configurations showed an interesting characteristic upon optimization. There was a transition from point to topological type of defects forming 5-8-5 rings in the case of C-bi vacancy and Si-C bi vacancy and it was a Li mediated transition in the case of Si-bi vacancy configuration. Among the various defective configurations, Stone-Wales (SW) defective configuration was found to be the best candidate having lowest value of binding energy compared to all the other configurations. The characteristics of SW configurations are specific capacity 501 mAh/g, open circuit voltage 0.11 V, diffusion barrier 0.57 eV which is in accordance with the electrochemical characteristics in being the anode of Li-ion batteries. Therefore, SW defective configuration was proposed to be a prospective candidate for the next generation Li-ion batteries.

Keywords: SiC; SiB; Density Functional Theory; Vienna Ab-initio Simulation Package; Structural properties; Dynamical properties; Electronic properties: Li-ion battery; Diffusion barrier; Binding energy; Specific capacity.

Contents

List of Figures

ii

iv

List of Tables

Chapter 1

INTRODUCTION

Materials pave way back to civilizations. The history of civilization can be described as breakthroughs in materials science progressing from the stone age through Bronze, Iron, Nuclear and Silicon ages (Crabtree et al. 2010). The advancement in materials technology through ages have designed the modern civilization making progressive innovations in industry, agriculture, health, energy and information technology. Materials have been in need for all the technological developments and the urge to develop new technologies need efficient materials. This opened a branch of science called materials science in which technologically advanced and efficient materials are identified and the influence of their microscopical features on the macroscopic behaviour are understood to apply them in various applications (Hafner 2000).

Scrutinizing materials by conducting experiments specially the ones with extreme conditions like high temperature, high pressure etc. lacked time and resources which led to the modelling of materials by theory and simulation. To define, a model is an analogue with various assumptions/approximations of a real system and a simulation is the reaction of the modeled system to external perturbations (LeSar 2013). The rapid development of computational power and the easy availability of softwares for the calculations profundly increased the scientific community to come up with technologically advanced and efficient materials for material processing. This rate of development show no signs of abating which developed models of unprecedented fidelity and speed and made a realistic description of wide range of materials possible. Due to this, com-

putational modelling of materials developed and expanded to all areas of science and engineering and have become an important tool in industrial and academic research.

Computational materials science (CMS) is a scientific field where materials are modelled and simulated to predict the material behaviour using the known concepts of Physics, Chemistry, Mathematics and computer science and are applied numerically. This significantly reduces the designing time, accelerates the deployment of new materials and experimental testing needs (Crabtree et al. 2010). CMS employs various steps to carry out calculations. It first defines what to calculate, makes a prototype of the real system, selects the relevant rule either classical or quantum, specifies the code or package to carry out the job, analyze the results obtained and compare with the experimentally determined data (Lee 2016). These are carried out based on any of the following methods i.e. first principle or *ab-initio*, molecular dynamics, monte carlo, finite-element analysis or QM/MM. The method used in the present thesis is the first-principle calculations.

A material in question consists of atoms or molecules and number of electrons and nuclei and the laws governing the behaviour of these sub atomic particles are well known. Solving Schrodinger equation is the basis of first-principle or *ab-initio* computing method. Rather than solving the simple hydrogen atom whose analytical solutions are well understood, instead many electron system needs to be solved which requires numerous approximations. Electron-electron interactions for a many body system is complex and is replaced with an effective potential considering each electron independent of each other (Ceder 2010). This approach was elaborated and various theorems were formulated by Hartree, Fock, Slater and further Hohenberg, Kohn and Sham reformulated all the above theorems to the much popular Density Functional Theory.

Density Functional Theory popularly known as DFT introduced by the two eminent scientists Hohenberg and Kohn has been a robust tool for predicting the immense varieties of materials and their properties. This has become a substitute for the wide variety of experiments which needs to be conducted for predicting the materials prop-

erties (Saito 2013). DFT is a method of solving the many body Schrödinger equation in which a real system is represented by an effective one body system and the ground-state properties are determined from the ground state density (Fiolhais et al. 2003). DFT specifically can be used to understand the electronic, mechanical, optical, magnetic and dynamical properties with great accuracy. A detailed description on DFT is given in Chapter 2 of this thesis.

The discussions of two dimensional materials age back to few decades. Wallace in 1947 proposed a monolayer of graphite to help deal with the band structure of graphite (Wallace 1947). Semenoff considered the same monolayer of graphite to understand the condensed matter simulation of a three-dimensional anomaly (Semenoff 1984) and Haldane in 1988 used it as a model for quantum hall effect (Haldane 1988). In the same year, Tomanek described a monolayer structure of BC_3 which showed distinct properties from it's bulk structure (Tomanek et al. 1988). In the 90s, carbon nanotubes were discovered and the graphite monolayer was used to understnad the electronic states of carbon nanotubes (Ajiki and Ando 1993). All these gave a prespective that one day a free standing two dimensional material would be possible. But, the Mermin-Wagner theorem says that 2D systems cannot spontaneously break the symmetry and cannot have long range order preventing it from existing unless there is the presence of a strong height fluctuations (Mermin and Wagner 1966). This theorem is valid only for infinite systems and does not rule out the pervalence of finite systems in two dimension.

The pioneering segregation of one atom thick layer of graphene in 2004 therefore came as a huge surprise. Graphene was first synthesized by the two nobel laureates, Novoselov and Geim giving birth to a new era of two dimensional materials (Novoselov et al. 2004). Graphene was exciting because of its unique electronic properties which is originated from its planar honeycomb structure. It has zero band gap with Dirac cones appearing near Fermi level contributing to its exceptionally high carrier charge density with charges behaving like relativistic particles (Novoselov et al. 2005, Ponomarenko et al. 2008). Graphene was also observed with extraordinary mechanical properties with Young's modulus of 1 TPa, fracture toughness of 4MPa (Zhang et al. 2014, Jiang et al.

2009). The advent of graphene with extraordinary electronic properties opened a vast realm of two dimensional materials to the scientific world including hexagonal Boron Nitride (h-BN), silicene, carbon nanotubes, silicon nanotubes, ZnO, MoS_2, germanene etc. (Liu et al. 2003, Nakano et al. 2006, Ajayan 1999, Fagan et al. 2000, Topsakal et al. 2009, Splendiani et al. 2010, Acun et al. 2015).

Among the predicted two dimensional materials, silicene was the next extensively studied candidate and was considered to be of special interest due to its potential application and its compatibility in silicon electronics. Silicene is a monoatomic sheet consisting of silicon atoms arranged in hexagonal lattice with atoms buckling out of plane unlike graphene (Cahangirov et al. 2009). It is a zero band gap semiconductor with linear bands appearing near the Fermi level and charges behaving like massless relativistic quantum particles. Silicene has substantially higher spin orbit coupling strength than graphene owing to sufficiently larger band gap near the Dirac point leading to quantum spin hall effect (Liu et al. 2011). Mechanical properties of silicene fall inferior to graphene with higher value of elastic bending stiffness due to buckling geometry present in silicene (Roman and Cranford 2014). The semimetallic characteristic of silicene hindered its use in electronic devices which requires a sizeable and well defined band gap. This drawback could be overcome to an extent by bandgap engineering which can be done by introducing vacancies or dopants, exposing to external force or fields or strain, confining to lower dimensions etc. (Sahin et al. 2013, Shinde and Kumar 2011, Yan et al. 2015, Gui et al. 2008, Shemella et al. 2007).

Silicene was introduced with various dopants to improve its basic properties. Silicene forms heterosheets of the form SiX and XSi_3 (X=B, C, N, Al and P) which are thoroughly explored by Ding et al. to understand its potential in nanoelectronics and devices (Ding and Wang 2013). Among the SiX type of derivatives, SiC forms a planar sheet analogue to graphene. SiB, SiN and SiAl prefers a washboard like configuration and SiP prefers a buckling pattern (chairlike) similar to silicene. On the other hand, XSi_3 exhibited planar configurations for all the sheets except N and P. NSi_3 and PSi_3 preferred chairlike configuration similar to silicene. Electronic properties of these

4

derivatives showed varied characteristics from silicene. Among SiX, SiC is a wide band gap semiconductor (> 2 eV), and all the others showed metallic character, and among XSi_3, BSi_3 and NSi_3 exhibited metallic nature, PSi_3 and $AlSi_3$ were narrow band gap semiconductors and CSi_3 showed semimetallic characteristics similar to silicene with Dirac-like bands near Fermi level. Phonon calculations of CSi_3, PSi_3 and $AlSi_3$ confirmed their dynamical stabilities. Understanding the basic characteristics of these derivatives would help in pertaining to various applications.

1.1   SiC

SiC is a binary planar sheet of Si and C akin to graphene with a lattice constant of 3.10 Å and Si-C bond length of 1.79 Å (Ding and Wang 2013). The structure of SiC is as shown in Fig. 1.1 with the unitcell marked. SiC is a direct band gap semiconductor with
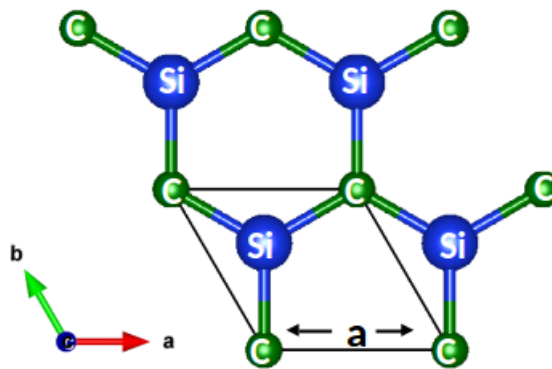
Figure 1.1: Structure of SiC with unitcell and atoms marked.

a band gap of 2.5 eV and high exciton binding energy upto 2 eV making it a futuristic material for electronic and optoelectronic applications (Shi et al. 2015). Monolayer SiC absorbs photons at 3.3 eV which enables it to be a potential material for photonic applications (Lin 2012). It is also assumed to play a major role as metal-free catalyst due to it's higher chemical reactivity towards foreign adsorbates (Wang et al. 2016b). Silicon carbide in layered, single walled (SW) and double walled nanotubes (DWNT) were thoroughly examined by Yu et al. to understand their energetics and the effect of buckling on the strain energy and also the variation in energy band gap along the changes

in tube diameter. They found a planar SiC 2D sheet after an optimization from the precursor buckling sheet. There was also a reduction in buckling when the tube diameter in the case of SWNT and DWNT were increased (Yu et al. 2009). SiC nanowires and nanoribbons were also extensively studied and they were found to be a potential candidate for hydrogen storage, nanodevices and microelectrochemical systems (Bekaroglu et al. 2010).

The synthesis of SiC in various nano-forms started from late 2000. SiC nanoflakes were synthesized in early 2006 by Zou et al. by a carbothermal process associated with a reaction of $SiCl_4$ and CaC_2 at a lower temperature of 180 °C and its structure was verified by X-ray diffraction, Infrared and Raman spectroscopy analysis (Zou et al. 2006). SiC nanomaterials were synthesized from waste plastics which are greatest environmental pollutant mixed with Si powder at temperatures of 350-500 °C in a stainless steel autoclave. This was then passed through $HClO_4$ at 180 °C to finally achieve 3C-SiC nanomaterial (Ju et al. 2009). Kuzubov et al. in 2013 predicted the potential of Mg(0001) and MgO(111) substrates to grow a monolayer of SiC, among which Mg tends to be the superior substrate over MgO (Kuzubov et al. 2013). Chabi et al. also claimed that 2D SiC nanosheet was produced by catalyst free carbothermal reaction and post sonication process (Chabi et al. 2016). Silicon carbide was also synthesized in nanowhiskers (SiCNWs) which was known for its exceptional electronic properties, thermal stability and chemical inertness. SiCNWs were synthesized by heating the blends of palm kernel shell (PKS) and silica in the ratio of 5:1 in a microwave furnace (Voon et al. 2016). Nanograins of SiC was accumulated in the pores of disordered graphene oxide (GO) which was confirmed by the scanning transmission electron microscopy images revealing the existence of planar two dimensional SiC (Susi et al. 2017).

Having a route to the experimental synthesis of 2D-SiC, various practical applications are thought of among which the capability of SiC to be the anode of Li-ion batteries was among the first preference. Rechargeable Li-ion batteries (RLIBs) have come as a remedy to the non-renewable fossil fuels usage and increasing need for electronic

devices in transportation, domestic applications and in consumer electronics (Meng and Arroyo-de Dompablo 2009, Goodenough and Park 2013, Islam and Fisher 2014). Carbon based materials specially graphite was the conventional electrode used in Li-ion batteries from its very beginning dealing with its safety primarily (Pistoia et al. 1994). Li intercalation into graphite was much easier because of its layered structure. Every six Carbon atoms could hold one Li atom forming LiC_6 giving a capacity of around 372 mAh/g (Dahn et al. 1995). This low capacity cannot fetch the high energy densities required for the present day electric vehicles. This was its greatest disadvantage urging its replacement for better and efficient materials.

Silicon was considered to be a promising material to be the anode of Li-ion batteries. It was known to have storage capacity of 4200 mAh/g and low discharge potential and is also abduntantly available in nature and environmental friendly (Franco Gonzalez et al. 2017). Whilst the charge capacity was much higher than the persisting graphite anode, volume change by 400% and low electrical conductivity resulted in capacity decay limiting its practical applications (Ryu et al. 2004). On the other hand, Li metal was found to be a superior candidate for anode of Li-ion batteries with a theoretical capacity of 3860 mAh/g and a smallest electrochemical potential. But the dendrite formation and volume expansion occurring in the batteries raised safety issues eventually looking for another candidate (Beaulieu et al. 2001). The advent of two dimensional materials and their exciting electronic and electrochemical properties showed potential in being the anode of Li-ion batteries. Graphene and silicene rather than in the pristine form showed superior capacity in the defected and in the doped form (Fan et al. 2012, Setiadi et al. 2013).

Being a wide band gap semiconductor, we expect less electrical conduction of pristine SiC which would in general reduce the capacity. This generated interest to look for possible alternatives and SiC was introduced with various kind of defects. Defects have improved the semiconducting nature and have finally enhanced the elctrical conduction in phosphorene and silicene (Guo et al. 2015, Setiadi et al. 2013). Previous studies reported that the introduction of defects can enhance the adsorption energy and lower Li

diffusion barrier in silicene thus making it a useful material in Li-ion batteries (Setiadi et al. 2013). This also causes a change in electronic bands further causing a change in electrical conduction in silicene (Li et al. 2014). Introduction of defects thus efectively promotes and improves the adsorption capacity of various adsorbants like graphene, h-BN sheets and nanotubes, MoS_2 etc (Fan et al. 2012, Shevlin and Guo 2007, Sun et al. 2015).

1.2   SiB

The elements silicon and boron are carbon's neighbours in the periodic table and are found to possess two dimensional monolayer structures. Silicene is very well described in the beginning of the introduction section. Boron atoms on the other hand, gave an indication of existence of monolayer with the successful experimental synthesis of single walled and multi walled nanotubes (SWBNT and MWBNT). The experimental characterization and theoretical prediction of these nanotubes revealed a conducting nature implying metallic characteristics of boron sheets if they exist (Liu et al. 2010, Bezugly et al. 2011). Later on, boron in many low dimensional forms were predicted specially boron fullerenes, α sheet, β sheet, γ sheet, etc (Tang and Ismail-Beigi 2007, 2010, Ozdogan et al. 2010). All these appeared flat and metallic except the α boron sheets which exhibited a buckled geometry with a narrow band gap. Boron is a prominent p-type dopant utilized in silicon industry due to which silicon-boron compounds have drawn ample importance. Silicon-boron compound prediction date back to 1900. Moisson and Stock were able to prepare SiB_3 and SiB_6 compounds (Moissan and Stock 1900). After these, SiB_4 (Silicon boride) was predicted in 1960 by Cline and group (Cline and Sands 1960). Structure of the compound was found to have resemblance to boron icosahedra. All the predicted compounds showed higher mechanical hardness which was again a reason for the interest in silicon-boron compounds.

Hansson et al. in 2012 predicted a graphene-like planar structure made of Silicon and Boron atoms. He thoroughly examined the structural and electronic properties of SiB and reported a flat conformation of SiB. The calculated total energy plotted against

the buckling parameter indicated lowest energy when the buckling was zero i.e. flat conformation. Later in 2013, Ding et al. studied various derivatives of silicene, along with the two dimensional SiB. SiB was reported to be having a low buckled washboard configuration by analysing their cohesive and formation energies. The washboard conformation was supposed to be having more stability than the flat conformation of SiB (Ding and Wang 2013). Si and B atoms are arranged alternatively in a hexagon with a lattice parameter of 3.41 Å(=a) and 5.74 Å(=b) and Si-B bond length of 1.95 Å. The washboard conformation of SiB reduces the symmetry leading to a rectangular unitcell with a≠b. The structure of SiB is as depicted in Fig. 1.2 showing the unitcell considered for study and the buckling of atoms present. Ding et al. confirmed the metallic nature

(a)

(b)
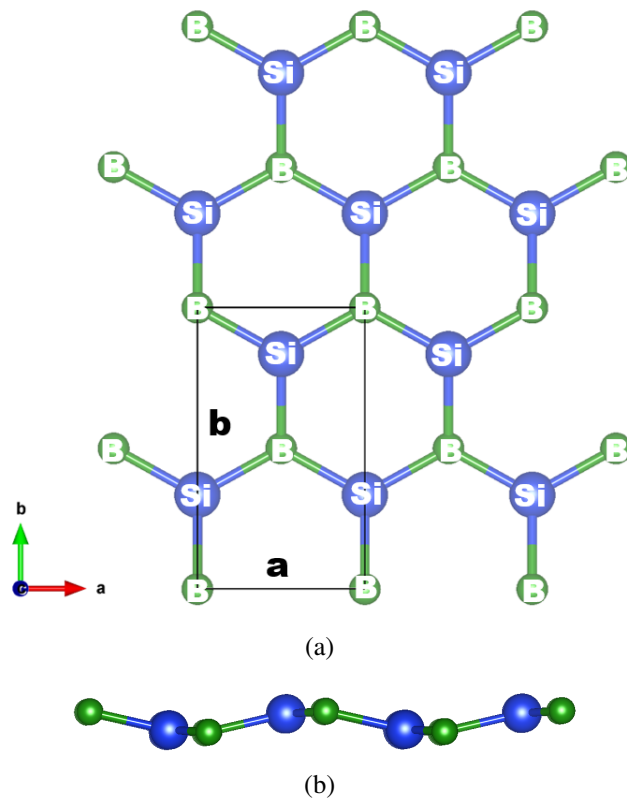
Figure 1.2: Structure of SiB with unitcell marked in fig. (a) and (b) shows the buckling of the Si and B atoms. Blue spheres are the Si atoms and green are the B atoms.

of SiB along with the determination of elastic constants signifying mechanical stability. The magnitudes of elastic constants obtained indicated SiB to be mechanically superior than silicene and the presence of anisotropy (Ding and Wang 2013).

SiC and SiB in nanostructures are predicted to be potential candidates for various applications being a derivative of silicene (Gori et al. 2012, Wang et al. 2016b). Thus, this thesis presents a thorough study of these (SiC and SiB) derivatives specially to understand the effect of strain on the structural, mechanical and electronic stabilities and also to understand the efficiency of these materials in being the anode of Li-ion batteries.

1.3 Scope and Objectives of the present research work

1.3.1 Scope

Excellent efficiency and long life Li-ion batteries and electric vehicles are required by the next generation automobiles and industries. The present day research predicts many nanomaterials which doesn't have even a route to its synthesis. In this context, SiC which is being experimentally synthesized plays a crucial role if it can overcome the capacity of the present graphite anode. Most of the two dimensional materials are assembled on a suitable substrate during their synthesis which can exert a strain on the material. So, it is also evident to look at the variation in properties with the implementation of strain in these materials and to understand their stabilities in the strain regimes. SiC being a wide band gap semiconductor would contribute less to electrical conduction due to which defects are introduced into the material to look for transitions in the mechanical and electronic properties and to evaluate the modification in adsorption and capacity. The characteristics of a good anodic materials are

- Lack of cluster formation of the intercalate on host material

- Lack of structural deformation of the host

- Low binding energy of intercalate with the host

- Low barrier potential and low voltage to intercalate through the host

1.3.2 Objectives

The basic properties of the two dimensional materials under study are determined using density functional calculations as implemented in VASP. Based on the above scope, the objectives for the present research work are designed in the following way.

- To apply strain in 2D-SiC and understand its effect on structural, mechanical and electronic properties.

- Strain is applied on 2D-SiB and understand the stability of SiB in various strain regimes. Undeformed SiB in its ground state is dynamically unstable and efforts are done to see if a dynamically stable configuration can exist with the application of strain.

- Plausible studies to test SiC and SiB to understand its potential in being the anode of Li-ion batteries.

- Introduce defects and see if there is alteration in basic properties (mechanical, electronic) and understand the defective configuration for the anode capability of Li-ion batteries.

1.4 Organization of the Thesis

- **Chapter 1** gives an introduction to the materials in general along with a broad idea about two dimensional materials. The importance of two dimensional materials on the present day research and their potential practical applications are thoroughly dealt in this chapter. The materials which are of our interest and their scope are discussed in detail.

- **Chapter 2** describes the methodology used in the present study in detail. A thorough description on Density Functional Theory and VASP software is carried out.

- **Chapter 3** presents the uniaxial and biaxial strain dependent changes in the structural, mechanical and electronic properties of 2D-SiC .

- **Chapter 4** discusses the changes in properties of 2D-SiB along with the application of uniaxial and biaxial strain.

- **Chapter 5** demonstrates the inefficiency of pristine SiC in being the anode of Li-ion batteries. This is then introduced with various kinds of defects (mono-, bi- and Stone - Wales) and the transformation in properties along with the efficiency of defective configurations in being the anode are thoroughly explained.

- **Chapter 6** points the major conclusions of the present study and the further opportunity in the study of these materials are discussed.

Chapter 2

COMPUTATIONAL METHODOLOGY

Carrying out expensive experiments to predict materials in fewer dimensions and under various extreme conditions like high temperature, high pressure etc. is an exhaustive process. Similarly, the less human intervened and the places inaccessible to human being like the extra terrestrial needs to be studied and understood. There is lack of time and resources to explore all the possible options experimentally. Advanced materials and processes are critical pacing elements for progress in advanced energy systems and virtually in all industrial technologies. Theoretical prediction through computer simulations has become an alternative for these tiring process. Perhaps, the most spectacular increase in capability has been demonstrated in high performance computing. Over the past decade, computational power has increased by a factor of million due to advances in hardware and software. This progress in computer technology made a realistic description of a wide range of materials possible. The present work deploy Density Functional Theory (DFT) calculations to find out the properties of materials under consideration.

2.1 Background

Classical Mechanics that ruled the universe for decades were found inadequate when the material was taken to subatomic levels. Atom was considered to be the smallest known entity until the discovery of electrons by J. J. Thomson. The atomic model persisted until then was reworked by Niels Bohr where he proved that the electrons revolve around nucleus without emitting radiation in specific energy known as orbitals. This picture of atom prevailed but was unable to completely explain all the characteristics (multi electron atoms, Stark effect, Zeeman effect) of atoms. On the other hand, quantum theory of radiation by Max Planck considered that the atoms could emit or absorb energy only in specific packets of energy known as quanta. This gave birth to the field of quantum mechanics, which understands the science behind elementary particles. This was followed by the introduction of wave-particle duality by de Broglie. All the above understanding of elementary particles led to the conclusion that they could be taken as a wave to completely understand their characteristics.

Erwin Schrödinger in 1926 first brought out his very famous wave equation for which he shared Nobel prize with Paul A. M. Dirac in 1933 (Pauling and Wilson 2012). This equation appeared extremely important as it contained all the information about a system.

$$\hat{H}\Psi(r_i, r_I, t) = E\Psi(r_i, r_I, t) \tag{2.1}$$

Here, $\hat{H}$ is the Hamiltonian operator, Ψ is the wave function, r_i is the coordinates of electron and r_I is the coordinates of nucleus. Unfortunately, the materials in question would contain several hundreds or thousands of atoms in it which in turn contributes majorely to the material properties and finding solutions to Schrödinger equation is a big hurdle and is almost futile and increases exponentially with the number of electrons present. This limits its extensive use confining it to solving small number of electronic systems. For example, a system containing single electron has three degrees of freedom but if the system contains n number of electrons then the degrees of freedom turns out to be 3n. Schrödinger equation needs to be solved in this case to completely understand the system. This becomes impractical and needs many approximations.

The first simplification is that of neglecting gravity and relativity assuming very little mass of electrons and its speed negligible compared to the speed of light. The relativistic efects for heavier atoms are incorporated in the development of pseudopotential. Time can be discarded if we restrict ourselves to ground state energy of electrons therefore the potential energy being constant over time. Taking away time from the Schrödinger equation, the modified equation becomes,

$$\hat{H}\Psi(r_i, r_I) = E\Psi(r_i, r_I) \tag{2.2}$$

2.1.1 Born Oppenheimer approximation

Nuclei being heavier makes the electrons respond spontaneously to nuclear motion and it occupies the ground state of that nuclear configuration. Thus the position of nuclei is assumed stationary in Born Oppenheimer approximation and therefore the kinetic energy of nuclei can be neglected and the Coulomb repulsion between them can be considered constant. This approximation allows in writing the Schrödinger equation in terms of electronic coordinates alone.

$$\left(-\frac{\hbar^2}{2m}\sum_i \nabla_i^2 + \sum_i V_n(r_i) + \frac{1}{2}\sum_{ij}\frac{1}{|r_i - r_j|} \right)\Psi_i = E\Psi_i \tag{2.3}$$

Here, The first term represents the kinetic energy, second term the external potential and the third is the electron-electron interaction term.

2.1.2 Hartree Method

To bring down the complexity in solving the Schrödinger equation, Hartree in 1928 proposed a one electron model in which each electron is considered independent of each other and interacts with others in a mean-field Coulomb potential. Hartree dealt with one electron at a time and the one electron Schrödinger equation turns out to be of the form

$$\left(-\frac{\hbar^2}{2m}\nabla^2 + V_{ext}(r) + V_H \right)\Psi(r) = E\Psi(r) \tag{2.4}$$

15

Here, $V_{ext}(r)$ denotes the interaction between electrons and nuclei, V_H is the Hartree potential arising from the interaction between electrons and the mean field. The total energies appear to be the summation of individual electron energies assuming the independent nature of electrons considered in this method and also the wave function tends to be the product of individual wave function.

$$E = E_1 + E_2 + E_3 + ... + E_n \tag{2.5}$$

$$\Psi(r_1, r_2, r_3, ..., r_n) = \Psi_1(r_1)\Psi_2(r_2)\Psi_3(r_3).....\Psi_n(r_n) \tag{2.6}$$

This method results in rough estimates of energies because it neglects the antisymmetry principle and Pauli's exclusion principle and also the exchange-correlation energies resulting from the electron interactions. Soon, this was improved to Hartree-Fock method.

2.1.3 Hartree - Fock Method

The improved HF method compared to Hartree method, considers the n-electron wave function as a slater determinant, the linear combination of noninteracting one electron wave functions. The ideology of slater determinant brings the missing anti-symmetry and Pauli's exclusion principle into the light. Now the Schrödinger equation takes the following form,

$$\left(-\frac{\hbar^2}{2m}\nabla_i^2 + V_{ext}(r) + V_{ij}\right)\Psi_i(r) = E\Psi_i(r) \tag{2.7}$$

The new term appearing in the equation V_{ij} is the electron-electron interaction term which has two components namely; the Coulomb energy between two electrons i and j (Hartree energy) and also the exchange energy appearing from the anti-symmetric nature of wave function thus making the energy calculation much more approximate compared to the preceding method. The eletrons with same spin are encountered in the above method but electrons with the opposite spins also needs to be accounted for better determination of ground state energy. This is the correlation term which is missing in the above method but HF helped in calculating the materials with few number of atoms

in it. Density functional theory developed by Kohn and Sham gave a breakthrough accounting all the missing terms from the above two methods.

2.2 Density Functional Theory

The major breakthrough in the theoretical calculation happened with the introduction of two theorems developed by Hohenberg and Kohn in 1964 which was later formulated as Density Functional Theory (DFT) by Kohn and Sham (1965). The theorems dealt with electron density and energy functional as the two essential entities in resolving a material under study.

Kohn-Sham uses electron density as the main entity to solve the many body Schrödinger equation containing n-electrons. This electron density approach cuts down the 3n-dimensional problem to n-3-dimensional problem and further to 3-dimensional density of electrons (ρ(x,y,z)). Now in the new approach, one needs to be worried only about electron density rather than wave function thus helping in analyzing large number of materials making computational science stream progress to a large extent. Electron density, $\rho(\mathbf{r})$ is basically the number of electrons per unit volume at a point $\mathbf{r}$. Now going back to the many electron Schrödinger equation, the total energy of the system can be written as :

$$E = < \Psi | \hat{H} | \Psi > = \int \Psi^*(r_1, r_2, ..., r_n) \hat{H} \Psi(r_1, r_2, ..., r_n) dr_1 ..... dr_n \qquad (2.8)$$

Here

$$\hat{H} = -\frac{\hbar^2}{2m} \nabla^2 + V_n(r_i) + \frac{1}{2} \frac{1}{|r_i - r_j|} \qquad (2.9)$$

Kinetic energy term and the electron-electron interaction term considered within the exchange and correlation in the above Hamiltonian is universal and therefore the Hamiltonian depends only on the $V_n(\mathbf{r})$ term implying the external potential which rely on ionic coordinates. This denotes that V_n uniquely determines the ground state wave function and thus ground state density. From this, it can be understood that the ground state wave function and ground state energy can be established from ground state electron density

17

n(**r**).

Hohenberg and Kohn in 1964 proposed two theorems which gave a precise ground for the definition of electron density as the fundamental entity in DFT. This theorems links between electron density, external potential, Hamiltonian and wave function. The first Hohenberg-Kohn theorem put forward that the ground state energy determined from the Schrödinger equation is a unique functional of electron density (Proof in Appendix A). Mathematically,

$$E = E[n(\mathbf{r})] \tag{2.10}$$

The theorem thus implies that knowing electron density can solely determine all the properties of a system including energy E[n(**r**)] and wave function $\Psi(r_1, r_2, r_3, ..., r_n)$ of the ground state. This brings down the problem of solving 3n variables, the wave function to 3 spacial variables, the electron density. But, the exact form of this functional is unknown for a general many body system. So, it is now necessary to understand how the functional actually look like. This was described in the second Hohenberg-Kohn theorem which specifies that it is the ground state electron density that minimizes the total energy of the system corresponding to the full solution of the Schrödinger equation (Proof in Appendix B).

$$\frac{\delta E[n]}{\delta n}\Big|_{n_0} = 0 \tag{2.11}$$

This theorem identifies a method to find out the minimum energy of the system and proves that this can be done through variational principle. For a given V_n, if we can reduce the system energy by varying the electron density and reach the minimum possible system energy, yet not below it, then this is the principle of variation in the scheme of DFT. Therefore, the functional takes the form

$$E[\Psi_i] = E_{known}[\Psi_i] + E_{xc}[\Psi_i] \geqq E_{gs} \tag{2.12}$$

Where E_{known} includes electron kinetic energies, Coulomb interaction between electron and nuclei,Coulomb interaction between pairs of electrons and pairs of nuclei and E_{xc}

includes all the other effects not included in the E_{known} term like the exchange energy, correlation energy etc. The search for the minimum energy can start from any initial guess usually this is done by taking the electron density generated by atomic orbital overalpping.

Kohn-Sham introduced a method to find out the right electron density by implementing an approach of reducing the N-interacting electrons to N non-interacting electrons moving in an effective potential. Kohn-Sham equation can now be written as

$$\left(-\frac{\hbar^2}{2m}\nabla^2 + V_n(\mathbf{r}) + V_H(\mathbf{r}) + V_{xc}(\mathbf{r})\right)\varphi(\mathbf{r}) = E\varphi(\mathbf{r}) \qquad (2.13)$$

Here, $V_n(\mathbf{r})$ is the interaction term considering the electrons and nuclei, $V_H(\mathbf{r})$ is the Hartree potential given by $\int \frac{n(r)n(r')}{|r-r'|}dr dr'$, $V_{xc}(\mathbf{r})$ represents the exchange and correlation contributions from the electrons. The above equation appears similar to Schrödinger equation with the summation missing in the present form just because the Kohn-Sham equations are single-electron equations depending on the three spatial coordinates. In order to solve the above equation (2.13), one needs to find out the Hartree potential which requires the knowledge of electron density. In order to define the electron density, the single particle wave function must be known and to determine the single electron wave function, one must solve the Kohn-Sham equation. This is done through an iterative process which can be defined the following way,

Kohn-Sham equation :

$$[-\frac{\hbar^2}{2m}\nabla^2 + V_{KS}(\mathbf{r})]\varphi(\mathbf{r}) = \epsilon\varphi(\mathbf{r}) \qquad (2.14)$$

Kohn-Sham effective potential :

$$V_{KS} = V_n(r) + V_H(\mathbf{r}) + V_{xc}(\mathbf{r}) \qquad (2.15)$$

$$V_n(r) = -\Sigma_I \frac{z_I}{|\mathbf{r} - \mathbf{R}_I|} \qquad (2.16)$$

$$\nabla^2 V_H(\mathbf{r}) = -4\pi n(\mathbf{r}) \qquad (2.17)$$

19

$$V_{xc}(\mathbf{r}) = \frac{\delta E_{xc}[n(\mathbf{r})]}{\delta n(\mathbf{r})}\Big|_{n_0} = 0 \tag{2.18}$$

$$n(\mathbf{r}) = \Sigma_i |\varphi_i(\mathbf{r})|^2 \tag{2.19}$$

- Define an initial trial density n($\mathbf{r}$).

- Substitute n($\mathbf{r}$) in eqn. 2.17 and obtain Hartree energy, V_H.

- Also, substituting in eqn.2.18 and using LDA or GGA schemes evaluate V_{xc}.

- Substitute the obtained V_n, V_H, V_{xc} in the KS equation and solve the equation to get $\varphi_i(\mathbf{r})$.

- Use the above $\varphi_i(\mathbf{r})$ and find out the new n($\mathbf{r}$).

- The obtained $\varphi_i(\mathbf{r})$ is placed in eqn. 2.19 and a new n($\mathbf{r}$) is determined and is compared with the old n($\mathbf{r}$) and the cycle is continued until both the n($\mathbf{r}$)'s reaches the specified accuracy.

2.2.1   Pseudopotential

When the atoms are brought close to form a solid, the valence electrons take part in atomic interactions and the core electrons remain mostly unaffected by their influence. This inspires in considering the valence and core elctrons into two different groups based on their contribution to atomic interactions. Core electrons and nucleus are considered together and is taken away from the calculations and this approach is called frozen core approximation. The remaining valence electrons are replaced with an effective potential, which is the pseudopotential. This concept replaces the actual wave functions with a pseudo wave function which reproduces the effects of the original wave function. This approach reduces the number of electrons needed explicitly thus saving the computational cost.

2.2.2   Exchange Correlation Functional

The XC term from the KS equation (E_{xc}) can be written as a sum of E_x and E_c, where E_x represents the exchange energy between the electrons with similar spin, is associated

with Pauli exclusion principle, antisymmetric nature of wave function and E_c represents the correlation between the electrons with opposite spin, can occupy the same orbital but repels each other because of same charge. Kohn-Sham equations are easily solvable if the exact form of exchange-correlation functional is known but defining this is extremely difficult. But we know that there is a functional which gives the exact ground-state energy and density, the various ways in which it can be approximated are

2.2.2.1 Local Density Approximation

Under this approximation, electrons are assumed to be distributed in a homogenous gas system in which electrons sees the overall density as the local density. So, the whole system is divided into many fragments containing uniform density and the total XC energy can be assumed to be the sum of all the energies coupled with the local fragments (Ceperley and Alder 1980). This approximation is local density approximation (LDA). This approximation is precise only when the density vary slowly or in the homogenous electron gas limit.

2.2.2.2 Generalized Gradient Approximation

Systems in reality are obviously not homogenous and have electrons in varying density terrains. To grab the effect of the inhomogenous density prevailing in the system, this approximation captures both the local electron density and its gradient at that point. This would contain more physical information than LDA but does not mean that this functional is accurate for all the physical real systems. There are many ways in which the gradient of electron density can be included in GGA functional. Most widely used GGA functionals are Perdew-Wang functional (PW 91) and Perdew-Burke-Ernzerhof (PBE) functional (Perdew et al. 1992, 1996).

2.3   Simulation method

In the present thesis work, DFT as implemented in Vienna *Ab-initio* Simulation Package (VASP) and Quantum ESPRESSO were used to carry out all the calculations. VASP and

Quantum ESPRESSO uses Kohn-Sham density functional approach (KSDFT) to solve the many body Schrödinger equation (Giannozzi et al. 2009). These are based on plane wave basis set and pseudopotentials (Kresse and Hafner 1993, Kresse and Furthmüller 1996). Generalized gradient approximation (GGA) parametrized by Perdew-Burke-Ernzerhof (PBE) was used for the calculation of exchange-correlation potential (Perdew et al. 1996). The valence electrons were considered explicitly for the calculations and the core electrons are incorporated using projected augmented wave (PAW) method based pseudopotential. The kinetic energy cutoff was maintained at 900 eV in the case of SiC and 700 eV in the case of SiB. Gamma-centered kpoint meshes were used to sample the Brillouin zone and it was found that a $20\times20\times1$ grid is sufficient to ensure convergence of energy for SiC and 21x21x1 for SiB and other physical properties. An interlayer spacing of 15 Å for SiC and 20 Å for SiB was found to be sufficient to make interlayer interactions, that arises because of the usage of periodic boundary conditions in VASP, to be negligible so that, for all practical purposes, the calculations being done pertain to a film of the material considered. The energy was converged to 0.001 eV/atom between two ionic steps and a convergence of 10^{-8} eV was kept for each electronic self-consistency (SC) loop. To apply strain on the material, lattice parameters of the unitcell were changed corresponding to compression or elongation in both uni and biaxial directions and the stress required to equilibrate the system to a varied unit cell was considered as the applied stress. Stress was applied uniaxially both in zigzag and armchair directions and biaxially and the variation in structural, mechanical and electronic properties were noted for both compressive and tensile regimes. The structure with equilibrium lattice parameter is considered as the undeformed structure here, and the lattice parameters were varied, increased and decreased up to 20% from the undeformed lattice parameter.

2.3.1 Elastic constants and mechanical properties

The elastic constants of a material gives its response to external mechanical perturbation. It is important to know the response of a material towards mechanical deformation for its practical synthesis and applications. The accurate calculation of elasticity helps

to understand the mechanical properties of solids thus helping the scientific world design new materials. When a force is applied to a continuum either internal or external, every point of the continuum is influenced by this applied force. This causes deformation of the medium. The basic law that relates this applied force to the resulting deformation is the Hooke's law. In order to study the higher order elastic constants, elastic properties of a material are described within Lagrangian theory of elasticity in which a solid is viewed as a homogenous and anisotropic medium [16]. When stress and strain are uniform, in the linearilized regime, they are related by Hooke's law.

$$\eta_{ij} = C_{ijkl}\tau_{kl} \tag{2.20}$$

Where C_{ijkl} is the stiffness tensor which in general is the elastic constants of the medium. Elastic properties of a material is obtained by Taylor expanding the internal energy as a function of strain, η,

$$E(S_0, \eta_{ij}) = E(S_0, 0) + \frac{S_0}{2!}\sum_{ijkl=1^3} C_{ijkl}\eta_{ij}\eta_{kl} + \frac{S_0}{3!}\sum_{ijklmn} C_{ijklmn}\eta_{ij}\eta_{kl}\eta_{mn} + ... \tag{2.21}$$

Where $E(S_0, 0)$ is the corresponding ground state internal energy, S_0 is the area of the unstrained system, C_{ijkl} is the second order elastic constants (SOEC), C_{ijklmn} is the third order elastic constants (TOEC). To simplify the above equation, Voigt notation [1] is used which cuts each pair of indices to single index and the simplified equation can be written as,

$$E(S_0, \eta_i) = E(S_0, 0) + \frac{S_0}{2!}\sum_{ij} C_{ij}\eta_i\eta_j + \frac{S_0}{3!}\sum_{ijk} C_{ijk}\eta_i\eta_j\eta_k + ... \tag{2.22}$$

Here C_{ij} and C_{ijk} are the second and third order elastic constants. According to the above equations (1) and (3), elastic constants can be defined as,

$$C_{ij} = \frac{1}{S_0}\frac{\partial^2 E}{\partial\eta_i\partial\eta_j}\Big|_{\eta=0} \tag{2.23}$$

---

[1]

ij	11	22	33	23	13	12
i	1	2	3	4	5	6

23

$$C_{ijk} = \frac{1}{S_0} \frac{\partial^3 E}{\partial \eta_i \partial \eta_j \partial \eta_k} \big|_{\eta=0} \tag{2.24}$$

Elastic constants play a significant role in providing information on the stability and stiffness of the material. They also play a crucial role in determining the strength of the material. Mechanical properties are divided into four strain domains based on loading : linear elastic, nonlinear elastic, plastic and fracture. Linear and nonlinear strain domains are reversible i.e., they are brought back to equilibrium after the removal of loads. Plastic and fracture domains are irreversible i.e., increase in strain nucleates and accumulates defects resulting in rupture (Peng et al. 2013a). Previous studies on various two dimensional materials have shown that they possess large non-linear elastic deformation in the tensile regime up to the intrinsic strength of the material and then strain softening until fracture (Peng et al. 2013b, Wang et al. 2010). Higher order elastic constants determine non-linear elastic response, anharmonic properties like phonon-phonon interactions, thermal expansion, Gruneisen parameter etc. Second order elastic constants (SOEC) model the linear elastic response.

By applying small specific elastic strains (α = 1–6 (six finite distortions in directions like xx, yy, zz, yz, xz, xy)) to the equilibrium unit cell, a set of elastic constants were obtained from the corresponding change in energy. The elastic constant tensors were calculated within VASP by performing finite distortions of the lattice and utilizing the relationship between stress and strain by Hooke's law, which represents the elastic constants. VASP uses finite difference method to compute the Hessian matrix, which is the second derivative of energy with respect to atomic positions. Finite difference method involves displacement of each ion in the direction of cartesian coordinates and the Hessian matrix is determined from the forces involved. Ibrion = 6 in the case of VASP, considers symmetry inequivalent displacements and symmetry is utilized in filling the rest of Hessian matrix. Elastic tensor in the case of VASP is computed by carrying out six finite distortions of the crystal lattice and obtaining the elastic constants via stress-strain relationships.

In order to determine the third order elastic constants of SiC, ElaStic was the tool used incorporated with Quantum ESPRESSO to determine the third order elastic constants (Golesorkhtabar et al. 2013). The solutions of density functional theory (DFT) calculations is obtained using Quantum ESPRESSO which is based on plane-wave (PW) basis set and pseudopotentials (PPs) to incorporate electron-ion interactions. Pbe (GGA) was used to account for exchange-correlation functional (Perdew et al. 1996). Kinetic energy cut-off was maintained at 60 Ry and kpoints at $17 \times 17 \times 1$. Vacuum region was maintained at around 28 Bohr to avoid any interaction between the layers. The code ElaStic requires the information on lattice parameters and crystal structure which was set in the code quantum ESPRESSO. Once the crystal is set, then ElaStic determines the space group and further sets the deformation type and energy for each of the deformation is calculated through ESPRESSO density functional set up. The energy obtained against each deformation or strain is polynomially fit and the elastic constants are determined by least square fit method with an appropriate polynomial.

2.3.2   Density Functional Perturbation Theory

The initial advancement in DFPT were done by Baroni, Giannozzi and Testa in 1987 and were later on followed by many of them. This method was then utilised in many of the DFT softare packages including VASP. In order to understand the interesting physical properties, it is necessary to study the response of a system against external perturbation which is dealt in density functional perturbation theory (DFPT). It is necessary to obtain the response functions which are second, third, or higher order derivatives of total energy with respect to applied pertubation. Assume a system is perturbed by applying an external force, where we define λ as the parameter defining the strength of perturbation. The new perturbed Hamiltonian appears in the following way and

$$H(\lambda) = H^{(0)} + V_{ext}(\lambda) \tag{2.25}$$

the Schrödinger equation for the perturbed system becomes

$$H(\lambda) |\psi_i(\lambda)\rangle = E_i(\lambda) |\psi_i(\lambda)\rangle \tag{2.26}$$

Now the total energy can be written as a power series in λ as

$$E(\lambda) = E + \lambda\frac{\partial E}{\partial \lambda} + \frac{\lambda^2}{2}\frac{\partial E^2}{\partial \lambda^2} + ... \tag{2.27}$$

So as to estimate the first order derivative of energy, it is only essential to calculate the unperturnbed wave functions and the first order change in external potential. This is the famous Hellmann-Feynman theorem (Proof in Appendix C). This also states that the first order energy derivative does not require the derivative of electron density to be known. So, we have

$$\frac{\partial E}{\partial \lambda} = \int n(\mathbf{r})\frac{\partial V(r)}{\partial \lambda}d\mathbf{r} \tag{2.28}$$

This makes it easier to calculate the second derivative of energy knowing the first derivative of electron density which is

$$\frac{\partial^2 E}{\partial \lambda^2} = \int \frac{\partial V_{ext}(\lambda)}{\partial \lambda}\frac{\partial n(\mathbf{r})}{\partial \lambda}d\mathbf{r} + \int n(\mathbf{r})\frac{\partial V_{ext}(\lambda)}{\partial \lambda}d\mathbf{r} \tag{2.29}$$

This gives an inference that to estimate the 2n+1$_{th}$ derivative of energy it is enough to know the n$_{th}$ order change in energy. This is known as the (2n+1) theorem which is useful in calculating the nonlinear response of materials. DFPT as implemented in VASP determines the interatomic force constants which is then diagonalized to obtain the dynamical matrix. This dynamical matrix helps in finding out the phonon frequencies, which can be utilized to understand the dynamical stability of the given system (Baroni et al. 1987)(Baroni et al., 2001). The obtained force constants are supplied in phonopy code to finally obtain the phonon dispersion curve (Togo et al., 2008).

2.3.3 Nudged Elastic Band Method

Atoms or any other matter will always follow lowest energy paths if they are introduced with some force under given conditions. Nudged Elastic Band (NEB) is a method helping to find the saddle point (SP) along minimum energy paths (MEP) between known reactants and products. NEB is a chain of states method which uses string of images connected by springs between an initial and final states (Henkelman and Jónsson 2000).

For carrying out the method efficiently, it is necessary to have a continuity in the band and also the images should be equally spaced which is assured by fixing a fictitious spring force through which the images are connected. Now, the process starts from the initial state and passes through each intermediate image which is simultaneously optimized to the MEP. In the normal elastic band method, the intermediate image doesn't necessarily fall to the saddle point and so was slightly modified by making one of the image to nudge to the saddle point which is the Climbing Image Nudged Elastic Band (CI-NEB) method(Henkelman et al. 2000). In the present case, CI-NEB was carried out using VASP considering 5 intermediate images between initial and final configurations. MEP : It is roughly a line connecting an initial and final states (minimum states) passing through the saddle point (SP).

SP : It is the highest point in the MEP that gives the value of activation energy barrier. SP energy is the minimum energy needed for a reaction to take place.

To analyse the Li-ion binding energy, the formula defined is as follows

$$E_{bind} = (E_{Li+SiC} - E_{SiC} - nE_{Li})/n$$

where E_{Li+SiC} is the energy of the Li adsorbed SiC, E_{SiC} is the ground state energy of SiC and E_{Li} ground state energy of the Li atom and n is the number of Li ion adsorbed onto SiC. To understand Li ion transport through SiC, Climbing Image Nudged Elastic Band (CI-NEB) method using 5 images was implemented using VASP. The minimum energy pathway and the diffusion barrier were obtained from the CI-NEB calculations. Theoretical specific capacity, barrier potential via NEB and open circuit voltage (OCV) are the prime factors which determine the validation of anode for the Li-ion batteries to be suitable for the next generation energy resources. Theoretical capacity and open circuit voltage (OCV) can be calculated considering the following relations :

$$Capacity, C = \frac{xnF}{MW}$$

Here, n is the number of Li ions, F is the Faraday constant, MW is the molecular weight of the material under consideration.

$$V_{oc} = -\frac{\Delta G}{\Delta nzF} = -\frac{\Delta E_{ads}}{\Delta nzF} = -\frac{(E_{ads(n_2)} - E_{ads(n_1)})}{F(n_2 - n_1)}$$

Here, ΔG is the Gibbs free energy of the system, z is the charge of Li ions, F is the Faraday constant, also, $E_{ads(n_2)}$ and $E_{ads(n_1)}$ are the adsorption energies of Li incorporated structures with n2 and n1 number of Li atoms (Butler et al. 2019).

2.3.4 Ab-initio Molecular Dynamics

Ab-initio molecular dynamics (AIMD) is a unique technique which helps in the realistic simulation of complex systems, i.e. how it evolves over time. The basic idea of ab-initio molecular dynamics simulation is to solve the quantum Schrödinger equation using the real physical potentials. Here atoms are moved in discrete time steps using Newtonian classical mechanics and the forces are obtained using the quantum mechanical methods. Various ensembles can be used like NVE, NVT, etc. In order to do a molecular dynamics simulation using VASP, the method involved is on the exact evaluation of the electronic ground state at finite temperature at each MD step using matrix diagonalization schemes and Pulay mixing schemes. To have a constant temperature, a canonical ensemble with a thermostat algorithm of the kind Nosé-Hoover must be used. Nosé- Hoover thermostat employs an extra degree of freedom into the Hamiltonian, a fictitious coordinate and a heat bath which is an integral part of the system.

Chapter 3

STRAIN DEPENDENT MECHANICAL AND ELECTRONIC PROPERTIES OF STABLE SILICENE DERIVATIVE SiC

A silicene derivative of the form SiC was thoroughly investigated on its behavior with changes in stress varying from around 140 N/m to around 20 N/m and strain from -0.2 to 0.3. Uniaxial stress (both zigzag and armchair) brought structural changes which reduced the symmetry of the system but biaxial stress brought no change in symmetry and shape of the material. Mechanical stability of the system was maintained upto a considerable stress in both uni- and biaxial cases and the system showed anisotropic behaviour with stress variations. Electronic structural variations showed strain engineering is a convenient method to tune the band gap very effectively causing semiconducting SiC to transform to metallic one at large stresses and direct to indirect bandgap in the semiconducting phase at lower stress. Charge density analysis showed a significant ionic nature of the material in the semiconducting phase.
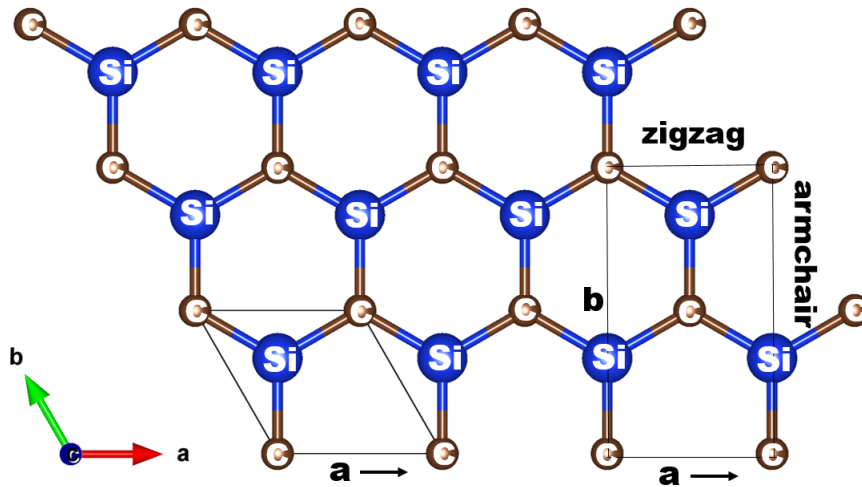
Figure 3.1: Unitcell of SiC considered for Uniaxial and Biaxial stresss. The cell in the form of a rhombus is used for biaxial stress and the cell in the form of rectangle for uniaxial application. The direction of zigzag and armchair is as marked.

3.1 RESULTS AND DISCUSSION

3.1.1 Structural Properties

The structure of SiC used for the stress is depicted as shown in Fig. 3.1. A system with hexagonal symmetry can be represented by an orthorhombic non-primitive unitcell which was considered for the application of uniaxial stress and the simulation cell was compressed and elongated along 'a'and 'b'thus obtaining zigzag direction along 'a'and armchair direction along 'b'and for biaxial the original unitcell with two atoms was considered as shown in Fig. 3.1. If a and b are equal, equal amount of stress is required to impart same amount of deformation along both directions. If a and b are terminated at 90° (non-primitive unitcell), the amount of stress required to deform would be different leading to different physics.

Energy per atom of the system in the whole range of stress studied confirms the energetical stability of SiC when it is subjected to uniaxial stress along zigzag and armchair directions as well as under biaxial stress. SiC being planar in structure maintains hexagonal symmetry with a space group of P-6m2. The symmetry of the system is broken to orthorhombic when the stress is applied uniaxially along zigzag and armchair direction leading to different physics but biaxial stress maintains the symmetry of the material.
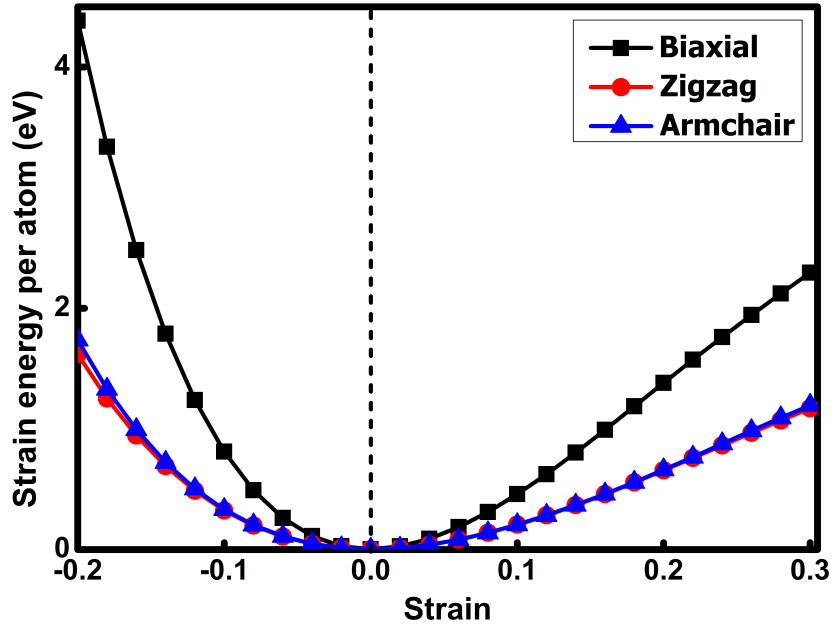
Figure 3.2: Variation in strain energy per atom with strain for zigzag, armchair and biaxial cases. Strains are varied from -0.2 to 0.3 and all the three curves represents anharmonicity and anisotropy present in the material.

Strain energy is the amount of energy stored in the system under deformation. Lagrangian strains ranging from -0.2 to 0.3 with an increment of 0.02 is considered for all three types of deformations. Strain energy per atom is defined as $E_s = (E_{tot} - E_0)/n$ where E_{tot} is the energy of the strained system, E_0 is the energy of the unstrained or undeformed system and n is the total number of atoms present in the unitcell. The variation of strain energy per atom for zigzag, armchair and biaxial stress is plotted in Fig. 3.2. Variation in strain energy with strain is almost identical for uniaxial zigzag, uniaxial armchair and biaxial stresses but the values of biaxial stress being higher compared to the other two. The curve representing the variation in strain energy per atom with strain implies that the strain energy is asymmetric along compression and tension in all the three cases signifying the anharmonicity and anisotropy present in the system. The stresses are basically the derivatives of strain energies, in the harmonic region they maintain a linear relationship. But, in the anharmonic region stresses are non-linear with respect to strain energies (Peng et al. 2013a).

3.1.2 Mechanical Properties

The elastic constants are crucial for the determination of the mechanical properties of materials, providing important information on their mechanical response, stability, stiffness and strength (Wang et al. 2012a). Second order elastic constants (SOEC) model the linear elastic response. Anisotropic elastic solids in three dimensions have 21 SOEC which reduces to 5 independent SOEC for a hexagonal structure due to the crystal symmetry (Mouhat and Coudert 2014). The deformations in 2D material can be solely approximated as an in-plane deformation neglecting all the out of plane components (Cooper et al. 2013). This implies that the in-plane components are non-zero and out of plane deformations are ideally zero. This implies that the number of independent SOEC reduces to three, i.e., C_{11}, C_{22} and C_{12} for the general case, and two, i.e., C_{11} = C_{22} and C_{12} for systems with hexagonal symmetry. The mechanical stability of a two-dimensional sheet is confirmed by Born-Huang stability criteria (Bom and Huang 1954), according to which a mechanically stable sheet with hexagonal symmetry should satisfy $C_{11} > C_{12}$ and C_{11}^2-$C_{11}C_{12} > 0$ (Born criteria). Young's modulus (E) and Poisson's ratio (ν) are calculated using the following equations

$$Y_s = \frac{C_{11}^2 - C_{12}^2}{C_{11}} \tag{3.1}$$

and

$$\nu = \frac{C_{12}}{C_{11}} \tag{3.2}$$

Elastic constants of SiC at ambient conditions are C_{11} = 179.2 N/m and C_{12} = 54.5 N/m which matches with the values reported by Ding et al. (2012) as tabulated in table 3.1. Bulk SiC has polytypes and they exist in more than 250 crystalline forms. One of the most studied polymorph is α-SiC which is hexagonal in symmetry which is used here for comparison. The Young's modulus and Poisson's ratio of 2D-SiC are

162.7 N/m and 0.30. SiC is found to be satisfying the above stability criterion thus confirming its mechanical stability. The variation in elastic constants with stress needs to be taken care for its practical applications. Figure 3.3 below shows the variation in elastic constants as a function of uniaxial zigzag, uniaxial armchair and biaxial stresses.

	SiC*	Graphene**	Silicene[†]	α-SiC[‡]
C_{11}	179.2	358.1	71.3	397
C_{12}	54.5	60.4	23.2	136

Table 3.1: Elastic constants of SiC along with graphene, silicene and bulk α-SiC. The values of C_{11} and C_{12} are in terms of N/m in the case of SiC, graphene, silicene and that of bulk α-SiC is represented in GPa. *Present study, **Shao et al.(2012), [†]Ding et al.(2013) and [‡]Malakkal L. et al.(2017)

The values of second order elastic constants are consistent with mechanical stability of the system in general and their values are plotted in Fig. 3.3. In the case of uniaxial zigzag stress, the magnitudes of C_{11} and C_{12} increase as the compressive stress increases and they maintain the Born stability criteria till around 35 N/m. The system tends to resist the deformation which in turn is reflected in the higher magnitudes of elastic constants. It can be seen that $C_{11} = C_{22}$ only when the stress is equal to zero and as the stress changes this equality is no longer valid because of the presence of anisotropy as could be observed from Fig. 3.3 in the case of uniaxial stress along zigzag and armchiar directions. C_{22} also increases with increasing compressive stress. Young's modulus increases with increasing compressive stress making the system stiffer. Poisson's ratio also shows an increasing trend along compressive regime. As the stress increases further to around 77 N/m, the mechanical stability is lost as C_{12} becomes greater than C_{11} violating Born criteria. The values of C_{11} and C_{12} tend to decrease as we increase the tensile stresses which corresponds to the less resistance offered by the system to deform itself. C_{22} also follows the same trend. Also, Young's modulus and Poisson's ratio decreases as expected. Similar trend could be observed when uniaxial armchair stress is applied. SiC maintains mechanical stability up to the highest stress of 85 N/m confirming the elastic resistance of the material till this stress in the compressive regime and around 19 N/m in the tensile regime. Young's modulus shows an increasing trend
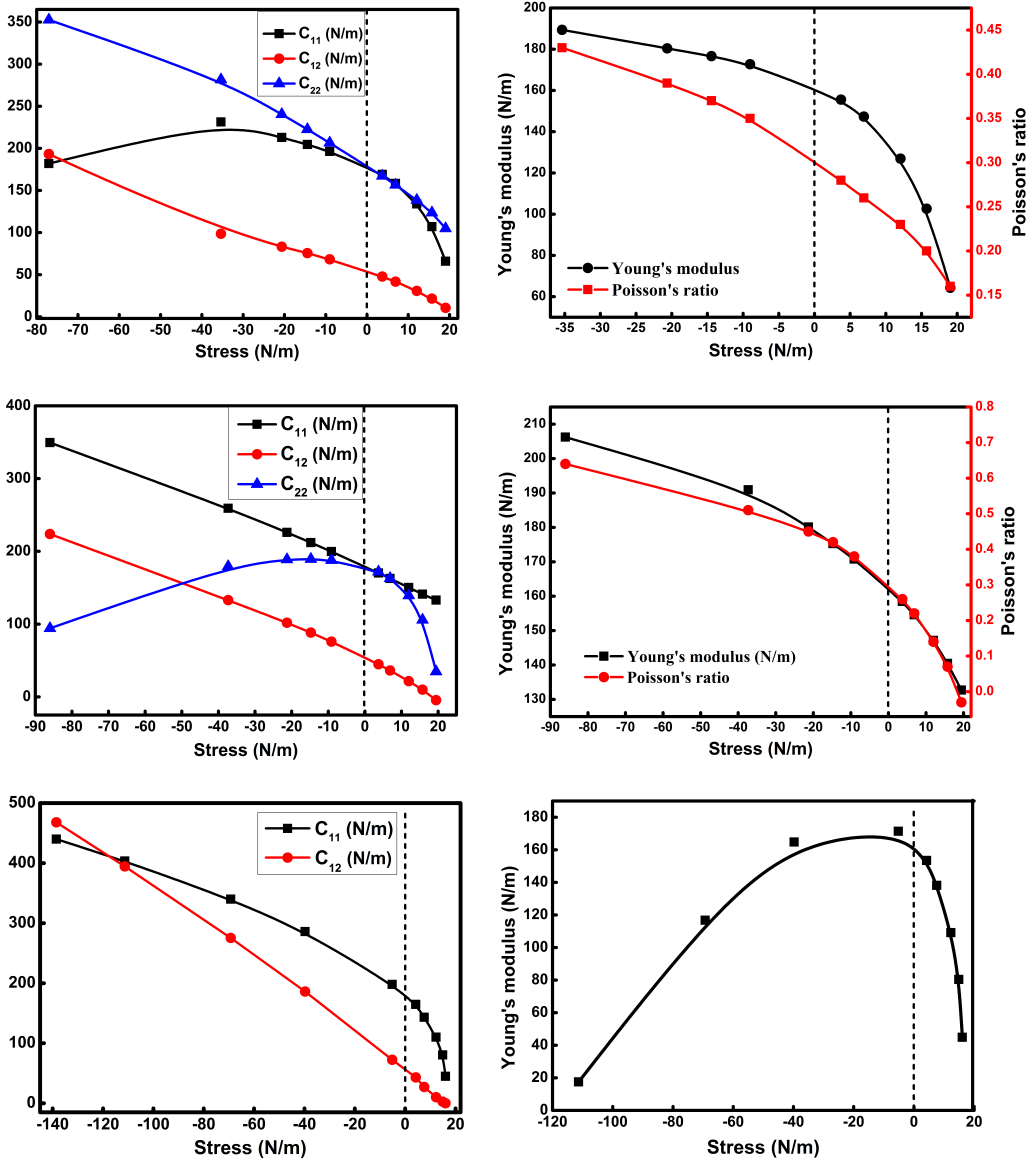
Figure 3.3: The graphs represents the variation in elastic constants, Young's modulus and Poisson's ratio along zigzag, armchair and biaxial directions. The three graphs on the left represents the changes in elastic constants with stress and on the right represents changes in Young's modulus and Poisson's ratio with stress.

implying that the system on increasing the stress, tries to become stiff and strong.

Similar trend in the case of elastic constants could be observed in the case of equi-biaxial stress also. SiC maintains mechanical stability until around 111 N/m confirming the elastic resistance of the material till this stress in the compressive regime and around 16 N/m in the tensile regime. When the material is further compressed, to around 135

34

N/m the mechanical stability is lost as C_{12} becomes greater than C_{11}. Young's mudulus tends to decrease along the compressive regime and tensile regime. The value of C_{12} increases substantially compared to C_{11} which in turn reduces the value of Young's modulus in the compressive regime. Poisson's ratio in the case of equi-biaxial stress is irrelevant as this is the phenomenon in which a material tries to expand in a direction perpendicular to the direction of application of stress. In a 2d material this perpendicular direction becomes the z-axis direction which is immaterial in these materials.

To have a complete non-linear behavior of 2D-SiC, we have done an extensive calculations with unequal biaxial stress which means, strains of different magnitudes were applied in the material simultaneously within a range of -0.1 to 0.1. A grid of increments 0.02 was considered for both strains along X and strains along Y and elastic constants were calculated at each grid points. The obtained elastic constants were plotted as a contour plot as shown in Fig. 3.4. The colour gradation in the contour plot of C_{11} and C_{22} clearly signifies that C_{11} and C_{22} are not equal in all ranges of strains indicating an anisotropic behavior of SiC in all ranges of strains applied.

Higher order (>2) elastic constants of a material are an important quantity which helps to determine the non-linear elastic response of the material and also the measure of anharmonicity of crystal lattice (Peng et al. 2012b). The third order elastic constants (TOEC) become important in describing the mechanical properties of a material under large stress or strain and also describes the anharmonic properties like thermal expansion, interaction of thermal and acoustic phonon, etc. Similar to SOEC's, there are 56 TOEC for an anisotropic material reducing to 10 for a hexagonal structure because of the crystal symmetry, further reducing to 3 (C_{111}, C_{112} and C_{222}) due to the geometry confinements in 2D materials. C_{111} and C_{222} are the longitudinal modes and C_{112} is the shear mode elastic constants . The values of TOEC are all negative because of the large positive strain energies for the negative strains compared to the positive strains. The values of TOEC of SiC are also tabulated in Table 3.2. The longitudinal modes of elastic constants are much larger in magnitude than the shear modes which is well understood from the fact that we deal with two dimensional materials whose z-direction
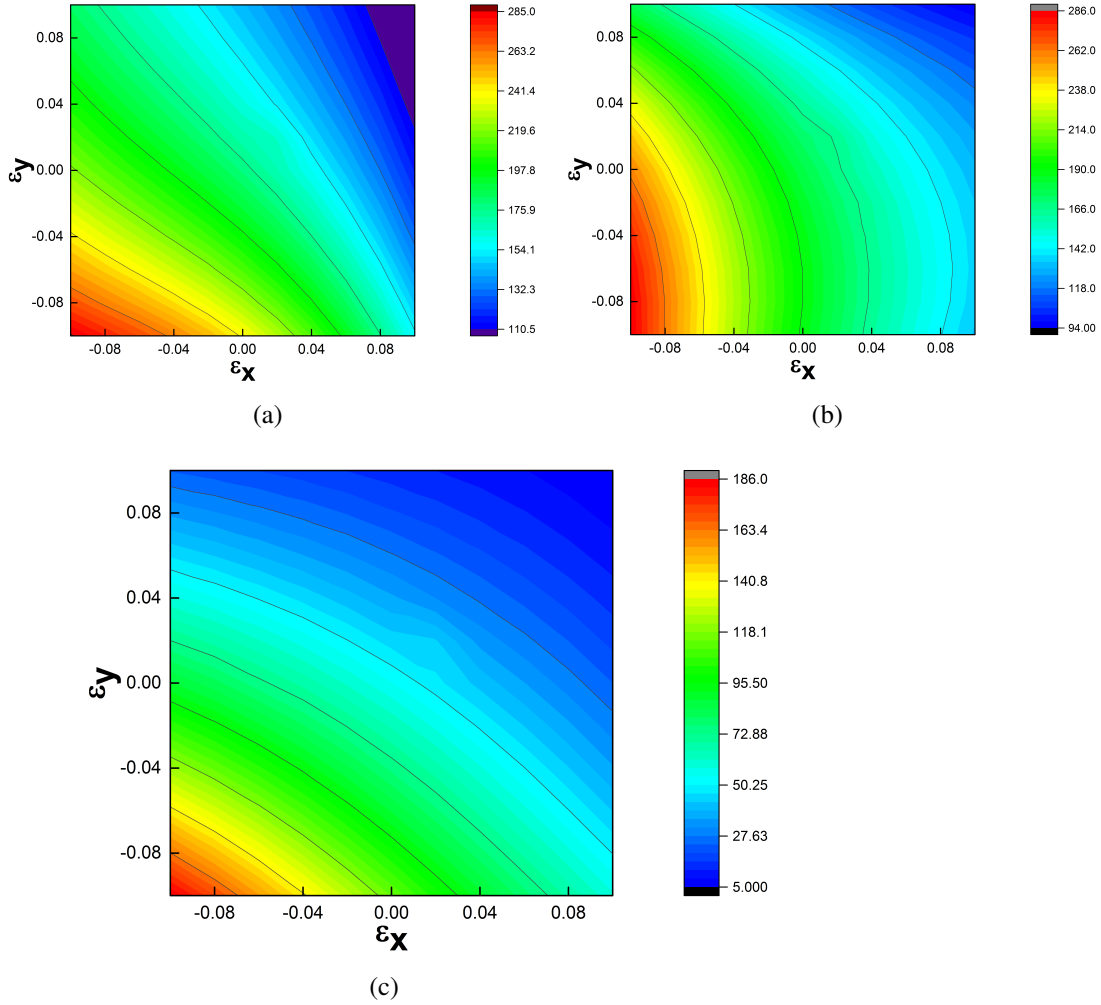
Figure 3.4: Contour plot of (a) C_{11}, (b) C_{22} and (c) C_{12}. Strains along X and Y is plotted along X and Y axes respectively. The colour gradation from red to blue implies values in the descending order.

is arbitrary. The magnitudes of TOEC show much higher magnitudes compared to silicene in the case of SiC as tabulated in table 3.2. This implies that the non-linearity and anisotropy goes up with the introduction of C atoms into the isotropic sheet of silicon.

	C_{111}	C_{112}	C_{222}
SiC	-1320.19	-312.49	-1150.63
Silicene*	-397.6	-14.1	-318.9

Table 3.2: Third order Elastic constants of SiC and silicene ((Peng et al. 2013b))* in units of N/m

Determination of elastic moduli experimentally requires the determination of compressional and shear wave velocities that passes through the medium. Understanding these waves helps to understand the elastic characteristics of that medium. Waves generating compressions are compressional waves or p-waves in which particles move in the direction of propagation of wave and those generating shear deformations are shear waves or s-waves in which particles move perpendicular to the direction of propagation of waves. Knowledge of second order elastic constants can be helpful in theoretically determining the compressional and shear waves giving an idea of propagation of sound waves through these media. This static calculation helps in determining the frequencies of the long wavelength vibrational modes, on the other hand, lattice dynamics (Quasi harmonic approximation) determines the frequencies of all vibrational modes which is beyond the scope of this work.
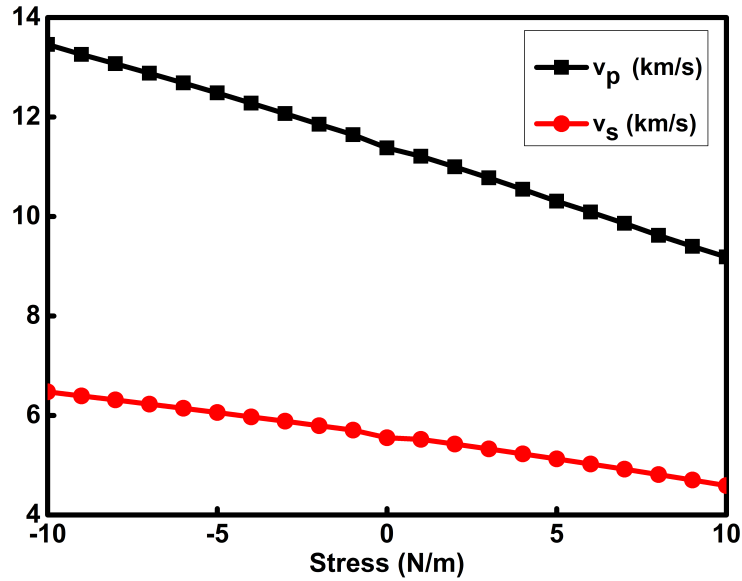
Figure 3.5: Variation in p- and s- waves with changes in in-plane stress of SiC.

The equations to determine the velocities of s- and p- waves are as follows.

$$v_p = \sqrt{\frac{Y_s(1-\nu)}{\rho_m(1+\nu)(1-2\nu)}}$$ (3.3)

and

$$v_s = \sqrt{\frac{C_{12}}{\rho_m}}$$ (3.4)

37

Where Y_s is the Young's modulus, ν is the Poisson's ratio and ρ_m is the mass density of the material. The mass density of a two dimensional material could be calculated using $\rho_{2D} = 4m_{SiC}/3a^2$ where m_{SiC} is the atomic mass of SiC and a is the lattice parameter of SiC.
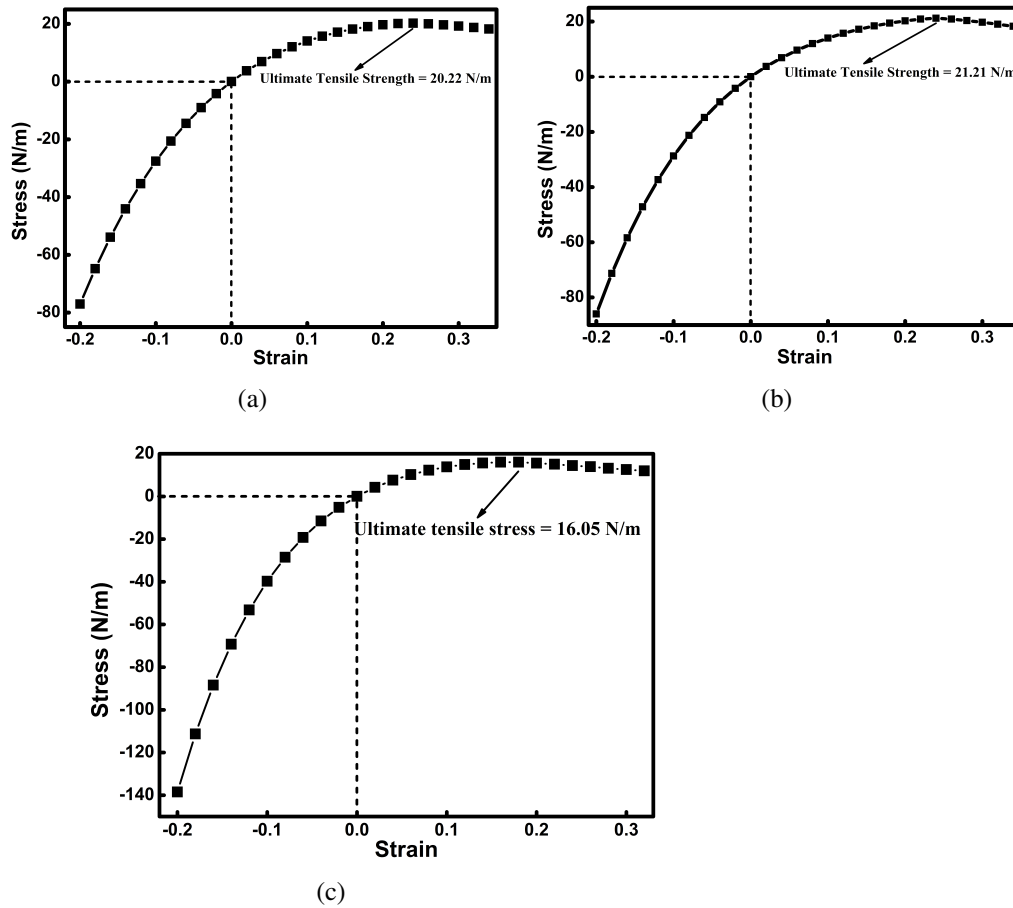
Figure 3.6: Stress-strain curves of (a) uniaxial zigzag (b) uniaxial armchair (c) biaxial stresses. The untimate tensile stress in each case is marked in the graph and toughness of the material is also calculated from the graph.

The two-dimensional mass density of SiC was calculated to be 16×10^{-7} kg/m^2 which is about twice than that of graphene due to the higher mass of Si. The magnitudes of p- and s- waves decreases with in-plane pressure for SiC is shown in Fig. 3.5. The velocities of p- and s- waves increases with increasing in-plane pressure during compression and decreases along tension in the case of SiC.

Stress-strain curve is an important graphical representation of a material's mechanical properties. Stress increases linearly with strain in the harmonic region and Hooke's law is obeyed in this regime. Anisotropic region is the one where stress-strain relationship is no longer valid and the higher order terms become significant. With larger strain, stress will increase enormously and ultimately the system fails. The maximum stress a material bear before breaking itself is known as the ultimate stress point or ultimate tensile strength (UTS) point. When the material undergoes stress beyond this point permanent damage occurs to the material and it can no longer restore its original shape. The typical stress - strain curves of SiC within uniaxial zigzag, uniaxial armchair and biaxial stresses are as shown in Fig. 3.6. Here, the ultimate stress and strain is 20.22 N/m and 0.24 for uniaxial zigzag, 21.21 N/m and 0.24 for uniaxial armchair and 16.05 N/m and 0.18 for biaxial direction respectively. UTS values of graphene, silicene is also tabulated in Table 3.3 along with SiC to have a comparison on the mechanical strength of these materials. The values imply that SiC may be considered as a strong material. The values of stress in the compressive regime is larger compared to that in the tensile regime as compression brings the atoms closer which makes the system in need of larger stress to compress than to expand. Also, compression makes the atomic orbitals repel making the stress almost double in the case of biaxial stress. The whole area under stress-strain curve upto fracture gives the toughness of the material. It is actually the energy required or stored by the material before fracture. The calculated value of toughness is around 3.8 GPa implying that the material is quite tough compared to graphene having a value of 4.4 GPa.

	SiC	Graphene	Silicene
Σ^z	20.22	30.4	5.9
Σ^a	21.21	28.6	6.0
Σ^b	16.05	32.1	6.2

Table 3.3: Ultimate Tensile Strength of SiC along with graphene and silicene in units of N/m. Σ^z - uniaxial zigzag, Σ^a - uniaxial armchair and Σ^b biaxial directions.

3.1.3 Electrical Properties

The electronic band structure of undeformed SiC is shown in Fig. 3.7. It is a wide direct band gap semiconductor having a direct band gap of 2.35 eV.

(a)

(b)
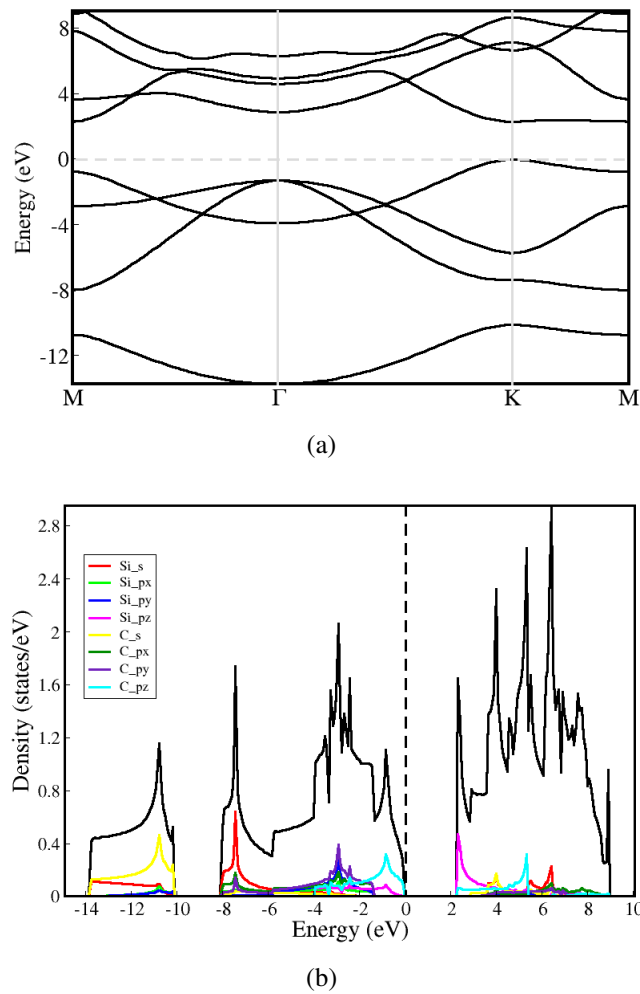
Figure 3.7: (a) Electronic bands and (b) Dos diagram confirming the semiconducting nature of SiC. The contibution of partial dos is shown in the dos plot.

Applying or inducing stress is an efficient method to tune the band gap of any material. Here, changes in electronic structure was determined with respect to varying stress. In the case of uniaxial zigzag stress, band gap decreases continuously in the compressive regime and the nature of the transition changes from direct to indirect with a slight change in stress value, the band gap reduces further and becomes metallic at the highest stress of 77 N/m. It shows a decreasing trend in the tensile regime maintaining

40
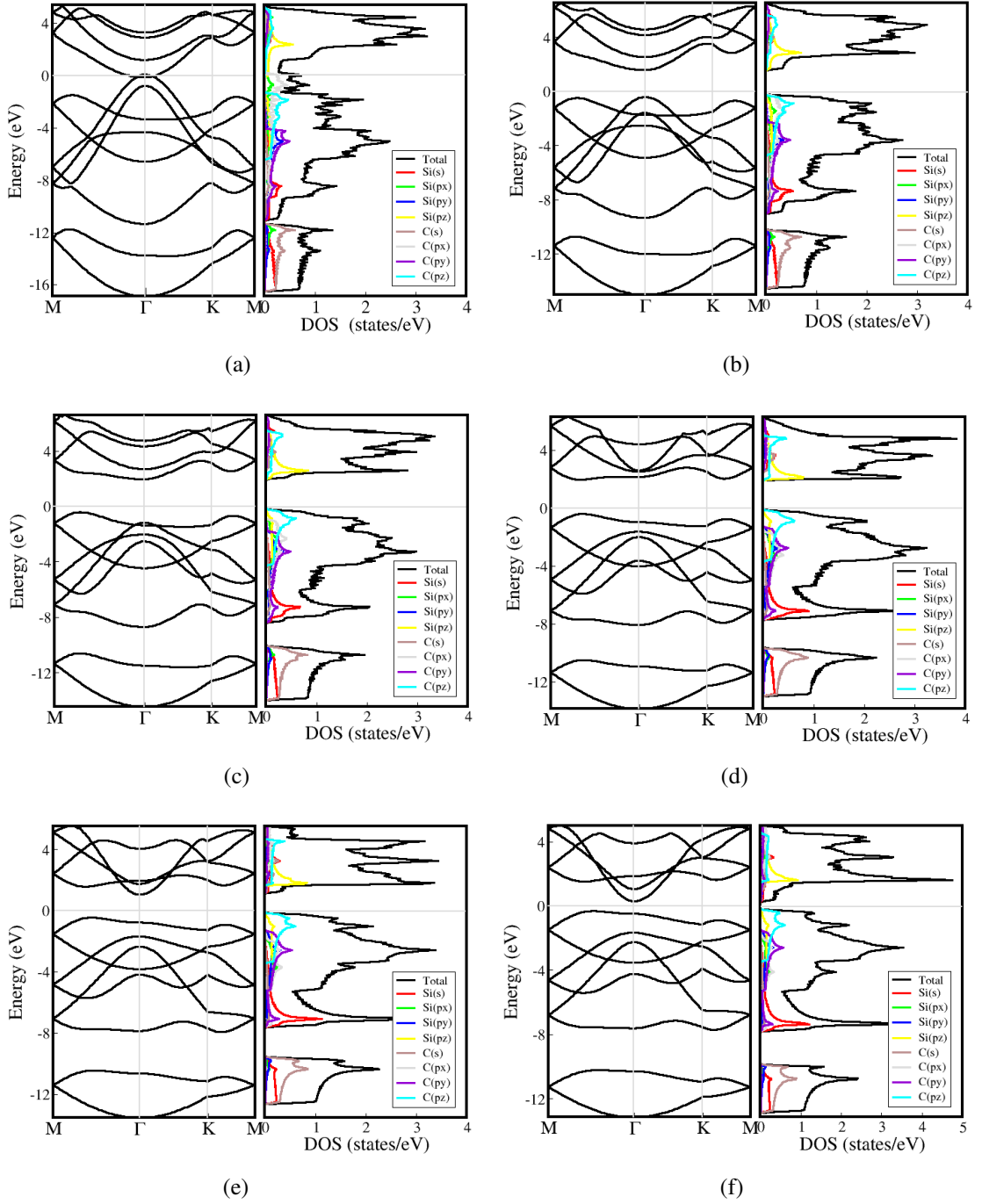
Figure 3.8: Electronic band and dos plot variations with respect to uniaxial zigzag stress. (a), (b) & (c) represents compressive regime and (d), (e) & (f) represents tensile regime. The band gap values are (a) Metallic, (b) E_g = 1.98 eV, (c) E_g = 2.38 eV, (d) E_g = 2.34 eV and (e) E_g = 1.48 eV and (f) E_g = 0.57 eV.

the direct nature till 12 N/m and then transforming into an indirect band gap semiconductor at 15 N/m as seen from Fig. 3.8. With increasing stress both in compressive
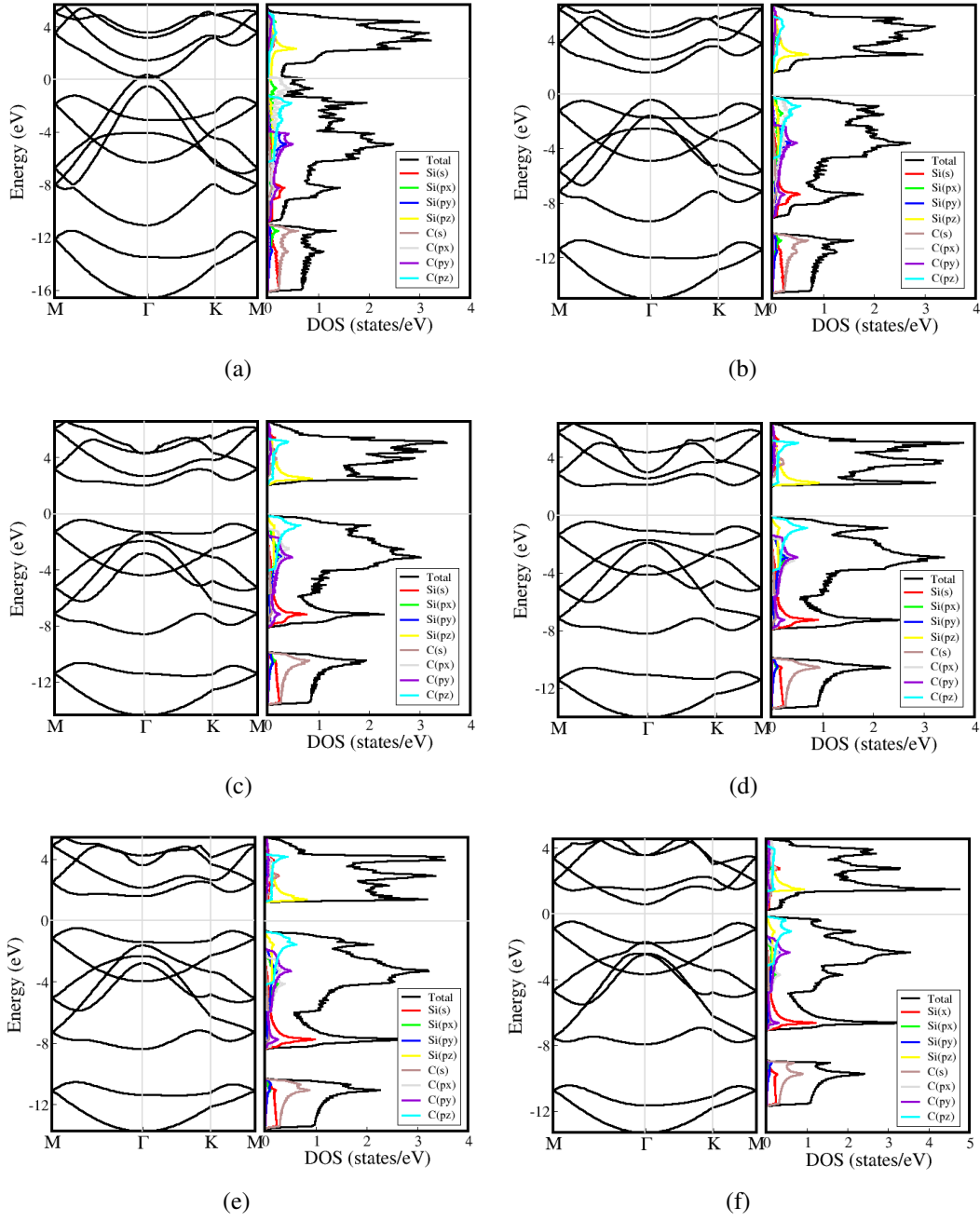
Figure 3.9: Electronic band and dos plot variations with respect to uniaxial armchair stress. (a), (b) & (c) represents compressive regime and (d), (e) & (f) represents tensile regime. The band gap values are (a) Metallic, (b) E_g = 1.85 eV, (c) E_g = 2.34 eV, (d) E_g = 2.35 eV and (e) E_g = 1.95 eV and (f) E_g = 0.91 eV.

and tensile regime, the valence and conduction bands shift causing a decrease of the band gap. The change in inter atomic distance and bond length due to the applied stress causes different superposition of Kohn-Sham orbitals causing a decrease of band gap.
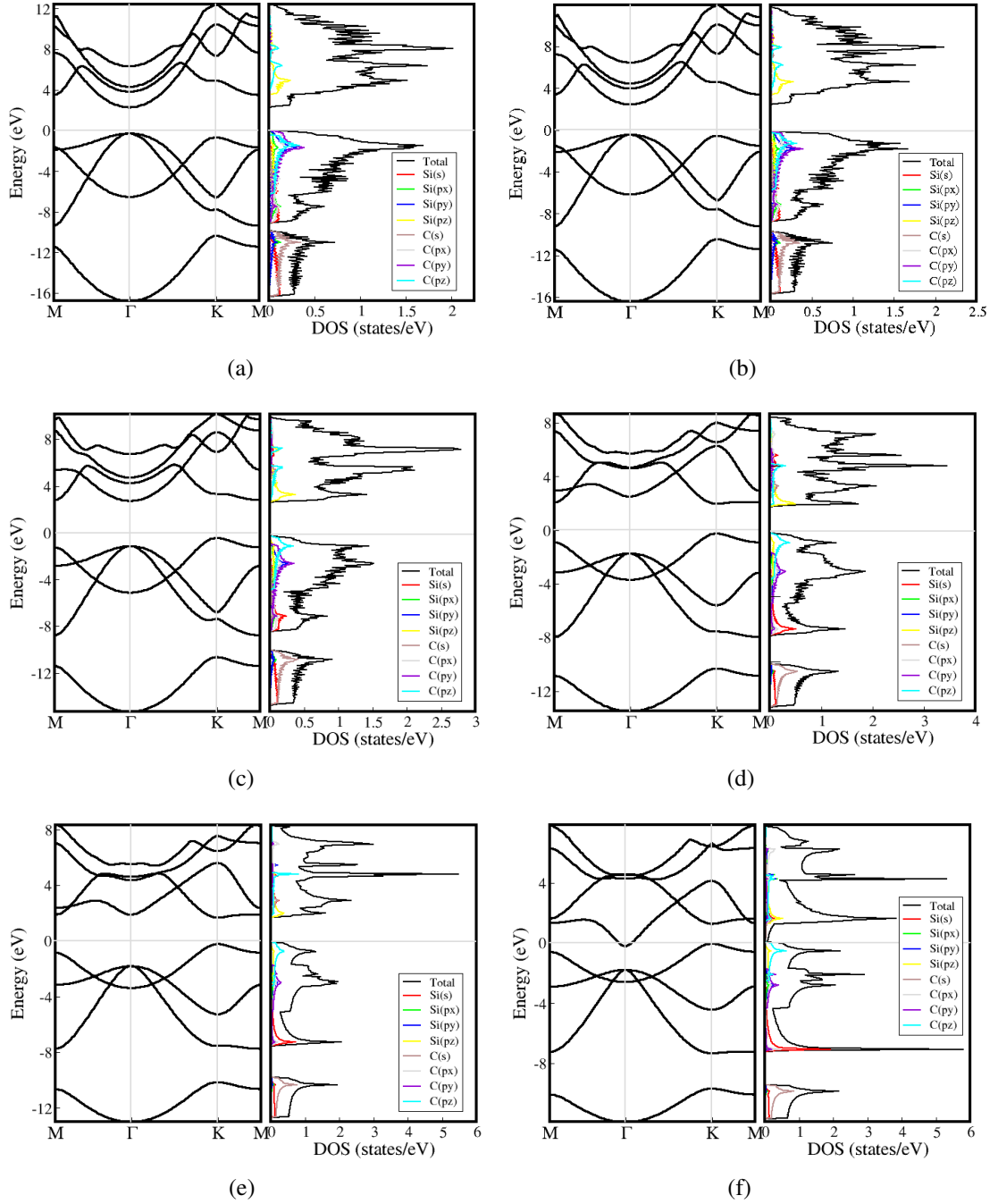
Figure 3.10: Electronic band and dos plot variations with respect to biaxial stress. (a), (b) & (c) represents compressive regime and (d), (e) & (f) represents tensile regime. The band gap values are (a) E_g = 2.56 eV, (b) E_g = 2.88 eV, (c) E_g = 3.12 eV, (d) E_g = 2.65 eV, (e) E_g = 1.83 eV, and (f) Metallic.

In the tensile regime, as the stress increases valence and conduction bands shift towards Fermi level reducing the band gap. As the stress increases more and more Kohn-Sham orbitals come closer to the Fermi level contributing to the reduction in band gap. The

43

observation on band gap reduction could also be confirmed by looking at the DOS plot as shown in Fig. 3.8. Similar trend is observed in uniaxial armchair stress (Fig. 3.9) with the transition from direct to indirect with a slight compressive stress. The system turns metallic at the highest stress of 85 N/m as observed. The indirect nature is maintained in the whole tensile regime.

In the case of biaxial stress, the band gap shows an increasing trend upto 40 N/m and then shows a decreasing trend. With increasing compressive stress upto 40 N/m, the atomic orbitals that contribute to the band gap are mainly the $Si(p_z)$ and $C(p_z)$ orbitals which could be seen from the DOS plot (Fig. 3.10). Further increase in stress induces other atomic orbitals also to come closer to the Fermi level which in turn makes the system metallic at the highest applied stress (139 N/m), p_x, p_y, p_z orbitals of Si and C contribute more towards the Fermi level thus reducing the band gap. Here, system transforms to indirect band gap semiconductor at a very small stress of around 5 N/m and then transforms to direct after 40 N/m. In the tensile regime, band gap decreases continuously maintaining the direct nature and the system turns metallic around 16 N/m. Thus, application of stress is a convenient way to easily tune the band gap of materials.
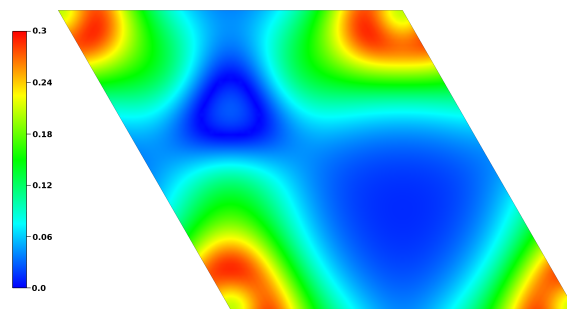
Figure 3.11: Charge density plot of undeformed SiC. The red to blue represents maximum to minimum levels of charge distribution. This plot shows the maximum charge accumulation around C atom instead of a uniform distribution pointing towards the ionic nature of the 2D-SiC.

Charge density coutours helps to understand the interactions between different atoms. The charge density contour was plotted for the undeformed SiC and for the maximum compressive and tensile stresses in zigzag, armchair and biaxial directions. The charge
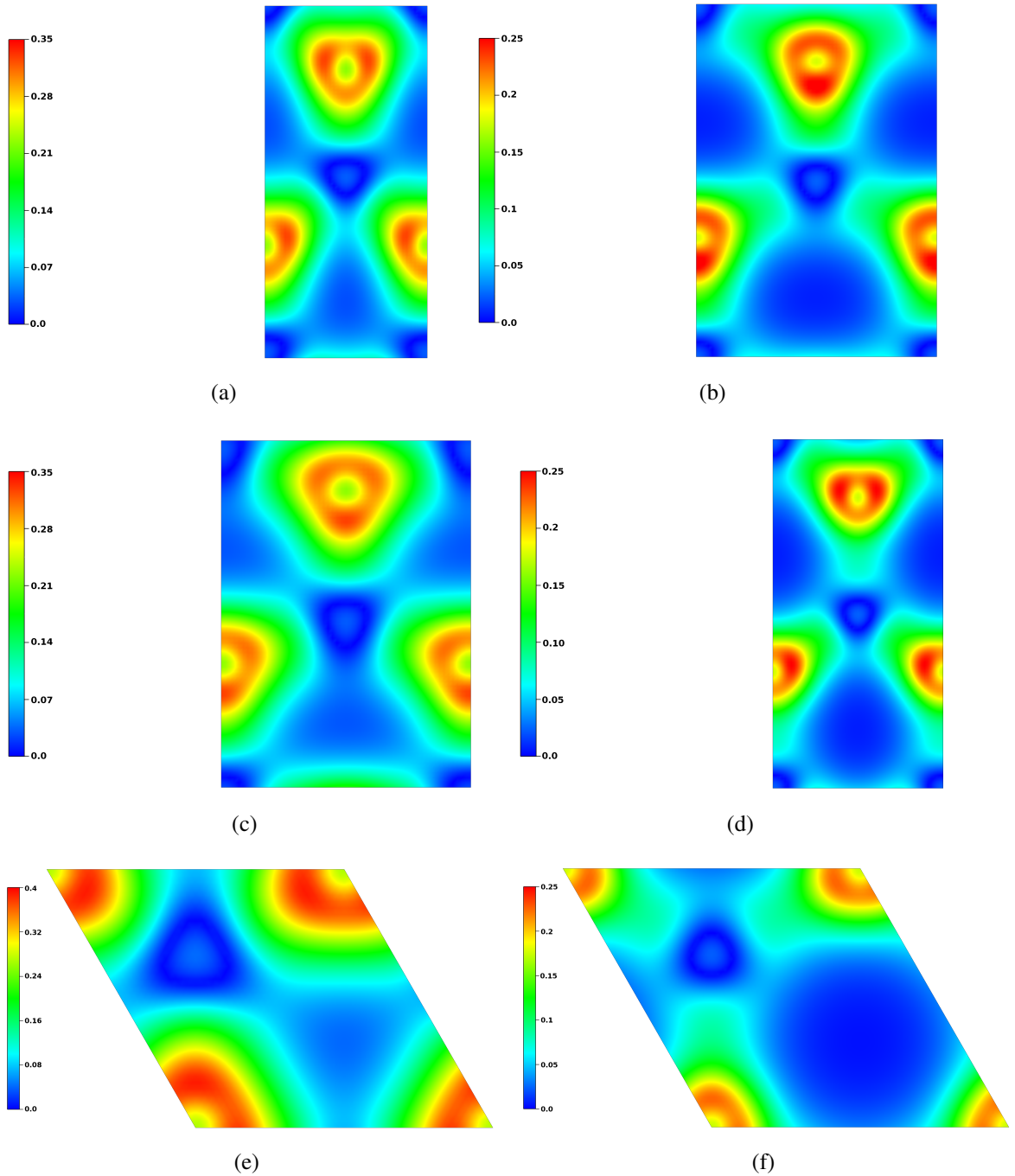
Figure 3.12: Charge density plot for (a) and (b) uniaxial zigzag, (c) and (d) uniaxial armchair, (e) and (f) biaxial. Plots for maximum compressive and maximum tensile are plotted in each case. Red to blue represents the maximum to minimum levels of charge distribution.

density plot for the undeformed SiC shows a maximum charge density around C atom implying an ionic character by SiC rather than a covalent nature which may be because of the higher electronegativity of C compared to Si. Charge density on each atom

was calculated using Bader analysis by partitioning the charge density along zero-flux surfaces (Henkelman et al. 2006). Zero-flux surface is a 2D-surface where the charge density is minimum perpendicular to the surface. Bader analysis done on SiC also confirms this observation and the charge density value obtained was $7.99/\text{Å}^3$. The charge density plot of SiC is as shown in Fig. 3.11.

Figure 3.12 shows the charge density plots for the maximum compressive and maximum tensile stresses for uniaxial zigzag, uniaxial armchair and biaxial directions respectively. In the case of compressive stress, the bond length reduces which causes orbitals to overlap to a greater extent thus increasing the extent of charge density. But in the case of tensile regime, the bond length increases causing reduced overlapping of orbitals thus the extent of charge density decreases but in all the cases the maximum charge density is accumulated around C atom which is also confirmed by the Bader charge analysis.

Chapter 4

STRAIN DEPENDENT MECHANICAL AND ELECTRONIC PROPERTIES OF SILICENE DERIVATIVE SiB

Two-dimensional monolayer SiB is a silicene derivative exhibiting buckling of atoms similar to that seen in silicene. Here, a systematic study of the strain-dependent variation of the structural, mechanical, and dynamical properties of SiB was carried out. Strain was applied in the uniaxial armchair, uniaxial zigzag, and biaxial directions within the range of -0.2 to 0.3. The resultant strain energy plot indicates anisotropic behavior of SiB in these directions. The SiB showed a mechanical strength that was higher than its counterpart, silicene, by an order of 30%. The elastic constant data from the undeformed SiB indicated an anisotropic nature, which was also seen with all the strain directions. Charge density contours, along with Bader charge analysis, confirmed the ionic nature of SiB in its original form. This nature became covalent as the strain varied from the compressive to the tensile regime in the uniaxial zigzag and biaxial directions. The major finding described here is a new flat conformation having orthorhombic symmetry in contrast to the buckled structure. In addition, this material was observed to attain stability with the application of uniaxial tensile armchair

and zigzag directional strains. Ab-initio molecular dynamics simulation confirmed the thermal stability of SiB in its new conformation.

4.1   RESULTS AND DISCUSSION

4.1.1   Structural properties

The structure of SiB resembles that of silicene with buckling as shown in Fig. 1.2. The simulation cell marked in the figure 4.1 represents both the equilibrium unit cell and the cell considered for the application of strain. A system in hexagonal symmetry can be described by a non-primitive orthorhombic unit cell, which is the equilibrium unit cell for SiB. The presence of buckling prevents in considering the primitive unit cell in this case.
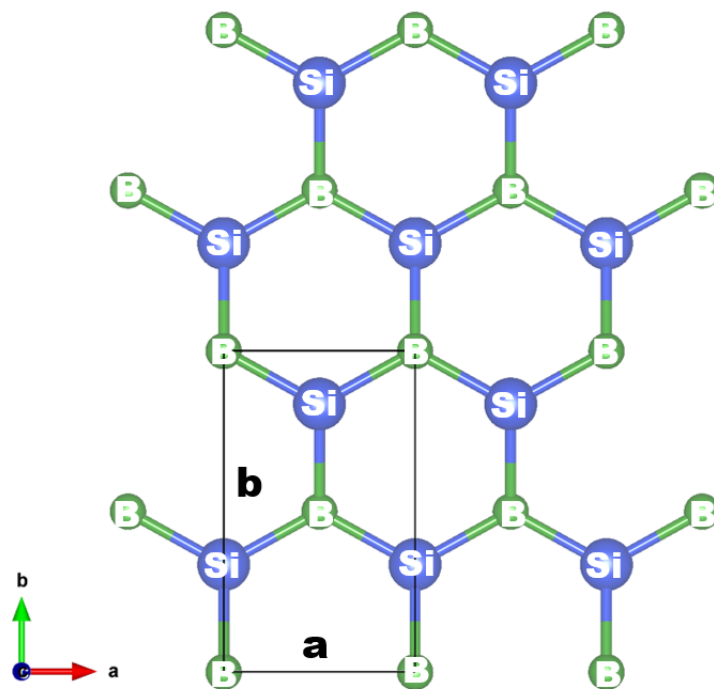
Figure 4.1: Structure of SiB with unitcell marked in fig. Blue spheres are the Si atoms and green are the B atoms.

The rectangular simulation cell marked in the figure is the unit cell considered for all calculations. The direction along 'a' is the zigzag direction and along 'b' is the armchair

direction. Strain applied equi-biaxially induces different stresses along both directions. Strain was applied uniaxially and biaxially to the SiB within the range of -0.2 to 0.3 in increments of 0.02. VASP computes the total energy with respect to the energies of the constituent atoms comprising the material, and therefore the total energy given by VASP is negative of the cohesive energy. Therefore, the cohesive energy values of SiB in all strain directions from the compressive to the tensile regime were negative, implying the energetical stability of strained SiB in the uniaxial and biaxial directions.
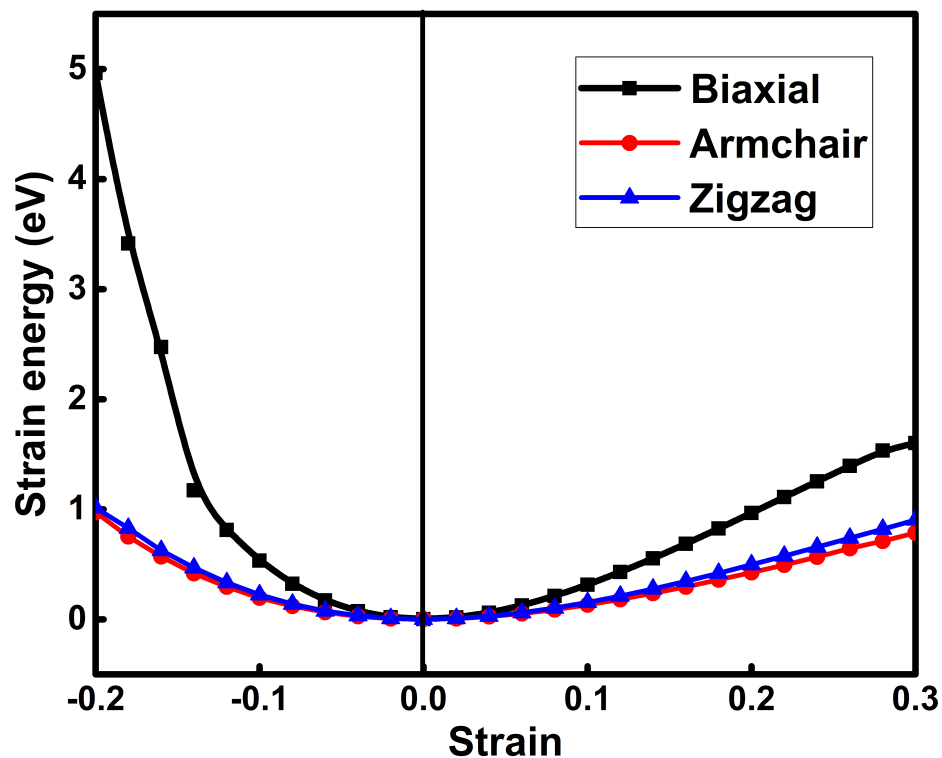
Figure 4.2: Strain energy per atom vs strain for uniaxial armchair, uniaxial zigzag, biaxial implying the presence of anisotropy and anharmonicity present in the system.

The strain energy per atom plotted against strain (see Fig. 4.2) indicates that the strain energy per atom is not symmetric in the compressive and tensile regimes, implying the presence of anisotropy in the material (Peng et al. 2012a). Asymmetry is identified in all cases of the biaxial, armchair, and zigzag directions. The curves representing the armchair and zigzag directions are identical, but that for the biaxial direction shows larger values. This variation arises from the fact that equal applied strains produce a

much larger energy variation in the compressive regime than in the tensile regime, in the biaxial direction compared to the uniaxial direction very similar to that of SiC.

4.1.2   Mechanical properties

Our material of interest has orthorhombic symmetry due to the presence of buckling, which in three dimensions has nine independent elastic constants. These reduce to four in two dimensions. Therefore, C_{11}, C_{12}, C_{22}, and C_{66} are the four independent elastic constants for the system under consideration. Young's modulus and Poisson's ratio are calculated using the relations as in eqn 3.1 and 3.2:

Table 4.1: Second order elastic constants of SiB compared with silicene

	C_{11}	C_{12}	C_{22}	C_{66}
SiB	101.35	32.56	47.60	19.68
Silicene*	71.3	23.2	71.3	-

In ambient conditions, SiB has elastic constant values higher than silicene, implying higher mechanical stability and better resistance to in-plane strains (Table 4.1). The values of C_{11} and C_{22} are no longer equal, indicating that SiB is anisotropic in its original undeformed state. Being orthorhombic in symmetry, SiB has C_{66} as an elastic constant. But silicene, being hexagonal, only requires the elastic constants depicted in Table 4.1. The Young's moduli and Poisson's ratios for SiB and Silicene are 90.89 N/m and 0.32 and 60 N/m and 0.4, respectively. Strain was applied uniaxially in the armchair, zigzag, and biaxial directions, and the effect of the elastic constants have been noted for each case. Fig. 4.3 shows the variation in elastic constants along with Young's modulus and Poisson's ratio for all three cases considered in the present study. As expected, when strain was applied in the uniaxial armchair direction (see Fig. 4.3(a) and 4.3(b)), C_{11} decreased from the maximum compressive strain until the maximum tensile strain was reached, implying that the system tends to most resist deformation caused by the applied strain in the compressive regime. The value of C_{12}, on the other hand, shows an

increasing trend in the compressive regime and a decreasing trend in the tensile regime. This indicates that the applied strain has a significant effect on C_{12}, lowering its value to the minimum possible. And then decreasing the strain, the system shows mechanical resistance which continues until the maximum tensile strain. The value of C_{22} tends to increase with increased compressive and tensile strain, and increases beyond the value of C_{11} after a tensile strain of 0.06. The values of C_{11} and C_{22} are not equal at zero strain, and there is a large variation in the magnitudes of these elastic terms which again indicates the anisotropic characteristics of SiB. Young's modulus shows a decreasing trend from the maximum compressive to the maximum tensile strain. Poisson's ratio shows an increasing trend in the compressive regime because of the large difference in the magnitudes of C_{11} and C_{12}. In an isotropic solid, Poisson's ratio can reach a maximum of 0.5, but in anisotropic solids, it can have values of up to 1 or beyond. This implies that the material is highly anisotropic under strained conditions (Akinwande et al. 2017).

In the zigzag direction (Fig. 4.3(c) and 4.3(d)), C_{11} shows a decreasing trend until -0.1, then increases until 0.1, and then decreases again until the maximum tensile strain. The magnitude is highest at the maximum compressive strain which indicates the resistance of the material to deformation. The values of C_{12} show an increasing trend in the compressive regime and decrease in the tensile regime. The decrease of C_{12} in the compressive regime shows that the material has less resistance to deformation. The values of C_{22} increase from the maximum compressive regime to the maximum tensile regime. The anisotropy present in the material is implied by the values of C_{11} and C_{22} at zero strain. Young's modulus has a very high value at the maximum compressive strain because of the higher magnitude of C_{11}. The system tends to be mechanically stronger under the maximum compressive strain. Poisson's ratio shows an increasing trend in the compressive regime, then decreases from the compressive to the tensile regime.

In the biaxial case (Fig. 4.3(e) and 4.3(f)), C_{11} shows much lower values at the maximum compressive strain, indicating the material's inability to withstand applied strains beyond -0.05. The magnitude tends to decrease in the compressive regime, indicating
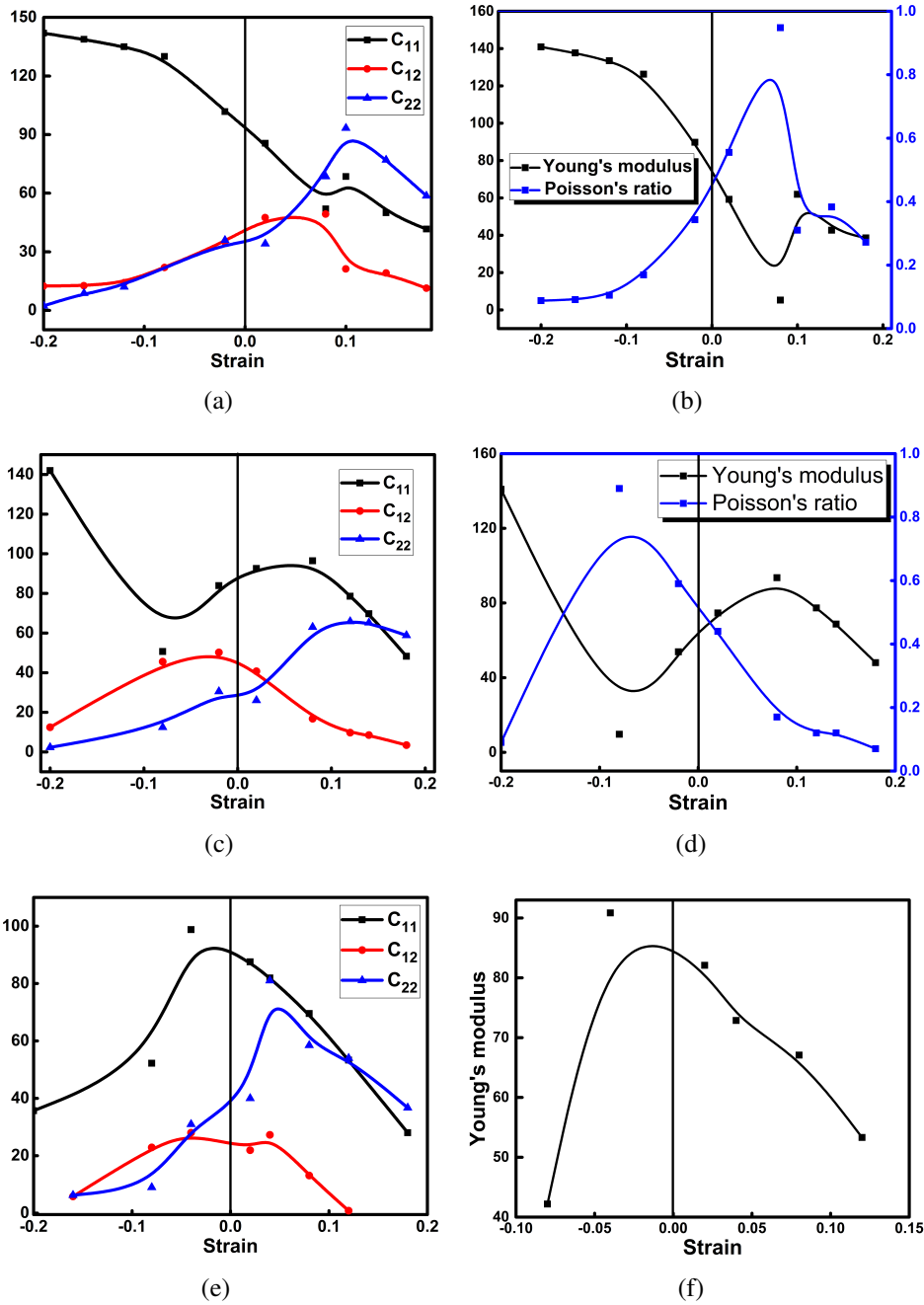
Figure 4.3: The graphs represents the variation in elastic constants, Young's modulus and Poisson's ratio along (a) and (b) armchair, (c) and (d) zigzag and (e) and (f) biaxial directions. The three graphs on the left represents the changes in elastic constants with strain and on the right represents changes in Young's modulus and Poisson's ratio with strain.

that the material may be mechanically unstable. As expected, C_{11} decreases beyond -0.05 up to the highest tensile strain (0.2). The magnitude of C_{12} also decreases in the compressive and tensile regimes. The unequal values of C_{11} and C_{22} at the consid-

ered strains imply that SiB has a highly anisotropic nature. Young's modulus shows a decreasing trend as expected, starting from a very low value for the maximum compressive strain. Poisson's ratio, in the case of biaxial strain, becomes insignificant as the biaxially-applied strain causes a strain in the perpendicular direction (z direction) which is irrelevant in two-dimensional materials.
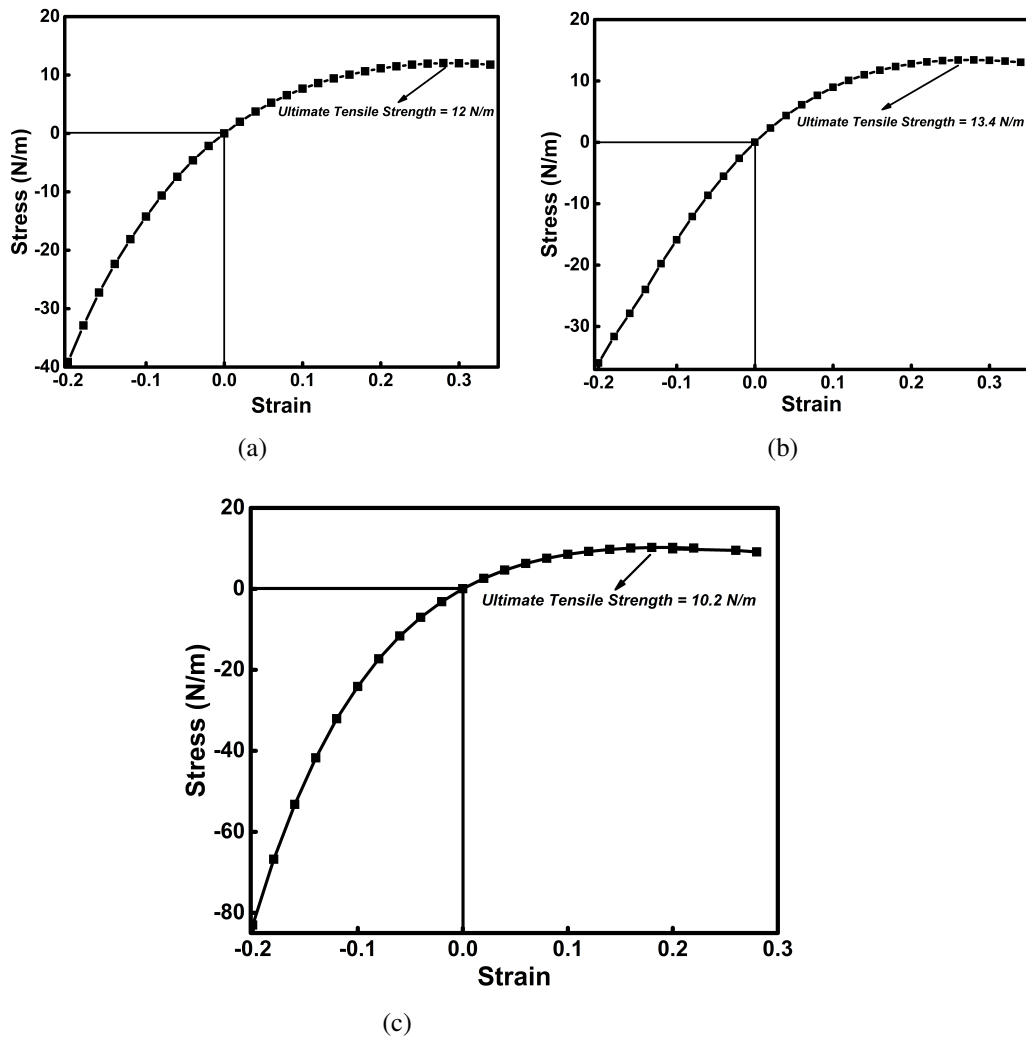
Figure 4.4: Stress-strain curves of (a) uniaxial armchair (b) uniaxial zigzag (c) biaxial stresses. The ultimate tensile strength in each case is marked in the graph and toughness of the material is also calculated.

Further, the stress-strain graph was plotted for the uniaxial armchair, uniaxial zigzag, and biaxial cases, and are shown in Fig. 4.4. The mechanical properties of a material can be understood by observing its stress-strain curve also. The ultimate stress and

	SiB	Silicene	SiC
Σ^a	12.0	6.0	21.21
Σ^z	13.4	5.9	20.22
Σ^b	10.2	6.2	16.05

Table 4.2: Ultimate Tensile Strength of SiB along with silicene and SiC in units of N/m. Σ^a - uniaxial armchair, Σ^z - uniaxial zigzag and Σ^b biaxial directions.

strain values for the uniaxial armchair, uniaxial zigzag, and biaxial cases are 12 N/m and 0.28, 13.4 N/m and 0.26, and 10.2 N/m and 0.18, respectively. The values are compared with silicene and monolayer SiC, and tabulated in Table 4.2. SiB has better mechanical strength than silicene, and is inferior to monolayer SiC. The stress values are higher in the compressive regime than in the tensile regime due to the larger resistance offered by the material when the distance between atoms decreases due to compression.
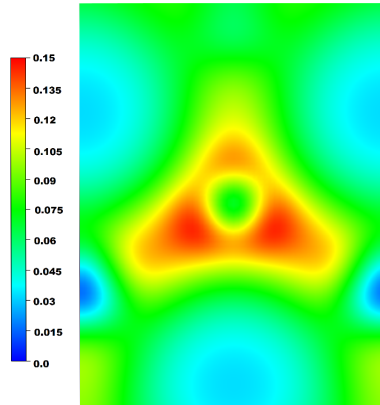
Figure 4.5: Charge density contour plot of SiB. Red to blue represents the maximum to minimum level of charge distribution. Charges are being concentrated around the center B atom.

The contour plot for charge density was obtained for the undeformed SiB and is shown in Fig. 4.5. The charge density distribution shows a uniform distribution of charges across the entire unit cell with a slight increase near the Si-B-Si bond connecting two hexagons of the material. Bader charge analysis performed on SiB implies that it has an ionic nature, with all charges ($7.000/\text{Å}^3$) accumulating around the B atom.

The contour plots for the maximum compressive and tensile strains in the uniaxial armchair, uniaxial zigzag, and biaxial directions were determined. The contour plots

for all three cases are shown in Fig. 4.6. The charge density contour plot for the maximum compressive uniaxial armchair direction (see Fig. 4.6(a)) shows a reduced distribution near the B atoms which occupy the four corners of the unit cell. The charges are concentrated toward the center, with the maximum distribution seen near the B atom (at the center). This indicates that SiB has an ionic nature, which was also calculated using Bader charge analysis ($7.000/Å^3$). In the tensile case (Fig. 4.6(b)), charges tend to be distributed throughout the unit cell, with the maximum concentration around the B atom (at the center), which shows it to be ionic from the Bader charge calculations ($7.000/Å^3$).

In the uniaxial zigzag direction, charges are concentrated towards the center of the unit cell, with the highest density of charges being concentrated at the B atom, implying an ionic nature in the compressive regime (Fig. 4.6(c)). The tensile regime (Fig. 4.6(d)) shows a more uniform distribution of charges, and the Bader analysis (for Si, $2.05 /Å^3$ and for B, $4.95 /Å^3$) indicates a transfer of charges from B to Si, showing a transition from an ionic to a covalent nature. The uniaxial zigzag direction shows a transformation from an ionic to a covalent nature as we move from the compressive to the tensile regime. The compressive regime of biaxial strain (Fig. 4.6(e)) has an ionic nature, with charges concentrating around the B atom. As we move to the tensile regime, the material transforms from having an ionic to a covalent nature (Fig. 4.6 (f)). This was also confirmed by Bader analysis, which showed the ionic nature seen in the maximum compressive regime converting to covalent when the strain reached the maximum tensile point (for Si, $3.49 /Å^3$ and for B, $3.50 /Å^3$). When moving from the compressive to the tensile regime in the uniaxial zigzag and biaxial directions, there is a transition from an ionic to a covalent nature.

4.1.3 Phonons and new SiB conformation

In general, SiB showed energetical and mechanical stability in a wide range of compressive and tensile strain regimes. However, SiB in its buckled pristine form showed slight
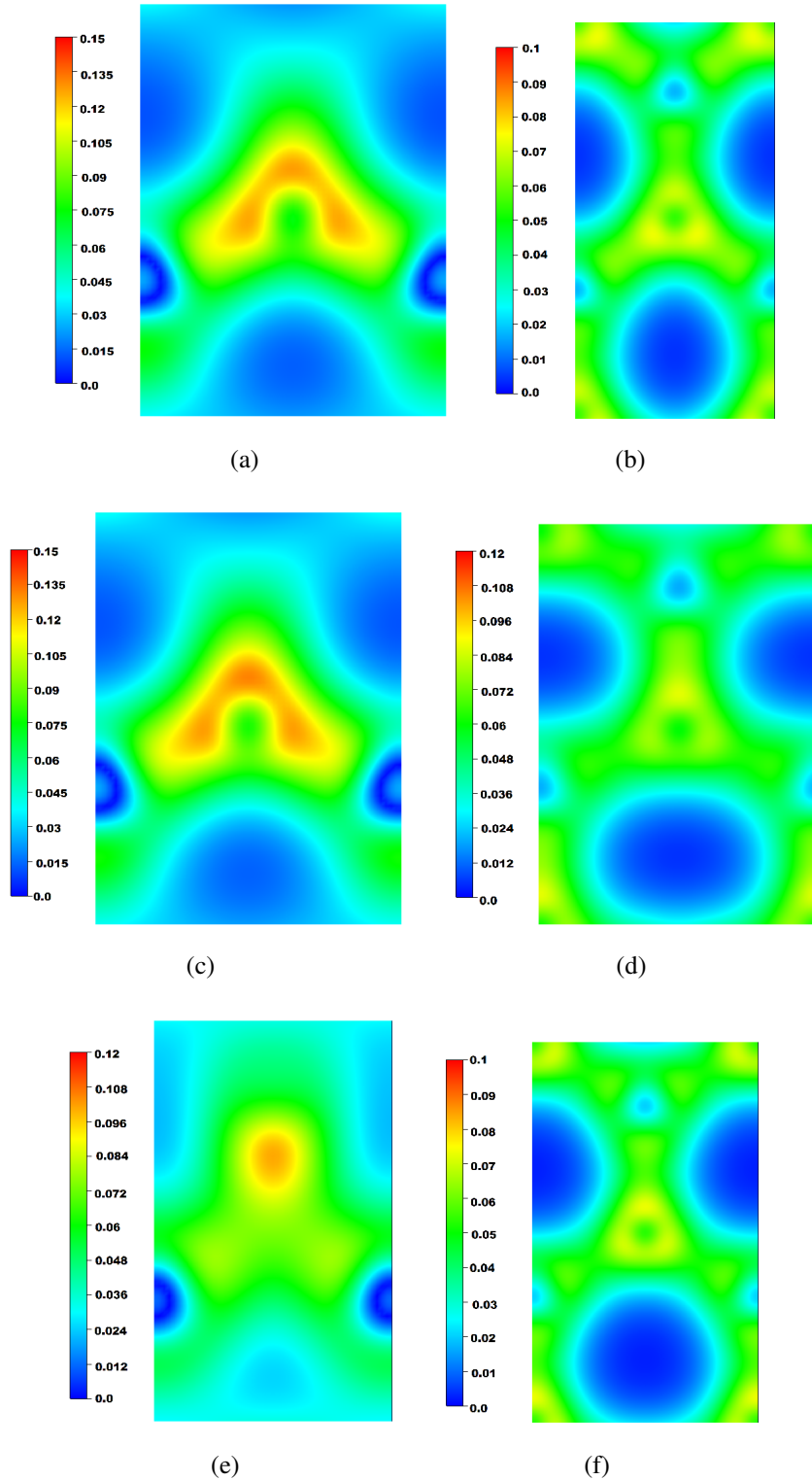
Figure 4.6: Charge density plot for (a) and (b) uniaxial armchair, (c) and (d) uniaxial zigzag, (e) biaxial. Plots for maximum compressive and maximum tensile are plotted in each case. Red to blue represents the maximum to minimum levels of charge distribution..
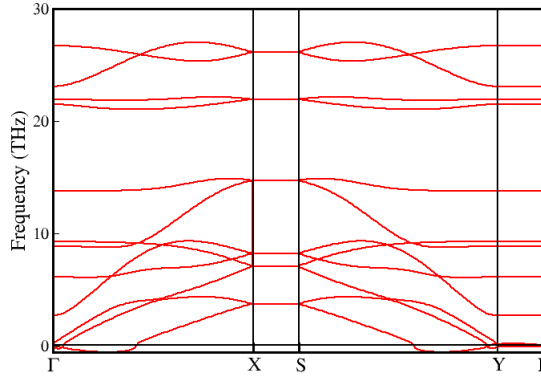
Figure 4.7: Phonon dispersion curve of buckled undeformed SiB

negative frequencies as shown in Fig. 4.7. A system is said to be dynamically stable only if all phonon modes have real frequencies for all wave vectors. The pristine SiB exhibited slightly negative frequencies in the ΓX and SY directions, implying the phonon instability of the system. Since the calculations are performed at absolute 0 K, there is a possibility that these negative phonon modes turn positive when the experimental realization of the system is achieved at room temperature or higher. The unstable nature of buckled pristine SiB encouraged an investigation into the dynamical stability of these systems along varied strains. Phonon dispersion curves were computed for all strain directions, but only cases which showed improved negative frequencies are discussed here. The phonon dispersion analysis is performed along the biaxial direction with respect to compressive strain values of -0.2 and -0.04. We found that there exist large negative frequencies in the phonon spectrum with respect to the applied strain. The phonon dispersion curves for compressive strains showed dynamical instability with larger negative frequencies for the phonon modes (Fig. 4.8 (a) and (b)). Under compressive strain, the in-plane lattice parameter falls below the equilibrium value, which results in negative frequencies for the low-lying acoustic modes. This has been already observed in graphene (Anees et al. 2015).

The phonon dispersion curves for the uniaxial tensile armchair and uniaxial tensile zigzag cases are shown in Fig. 4(c) and (d). The curves for a tensile strain of 0.08 are depicted for both the armchair and zigzag directions. The magnitudes of the negative frequencies have significantly decreased. These would become positive with temper-

57

(a)

(b)

(c)

(d)

(e)

(f)
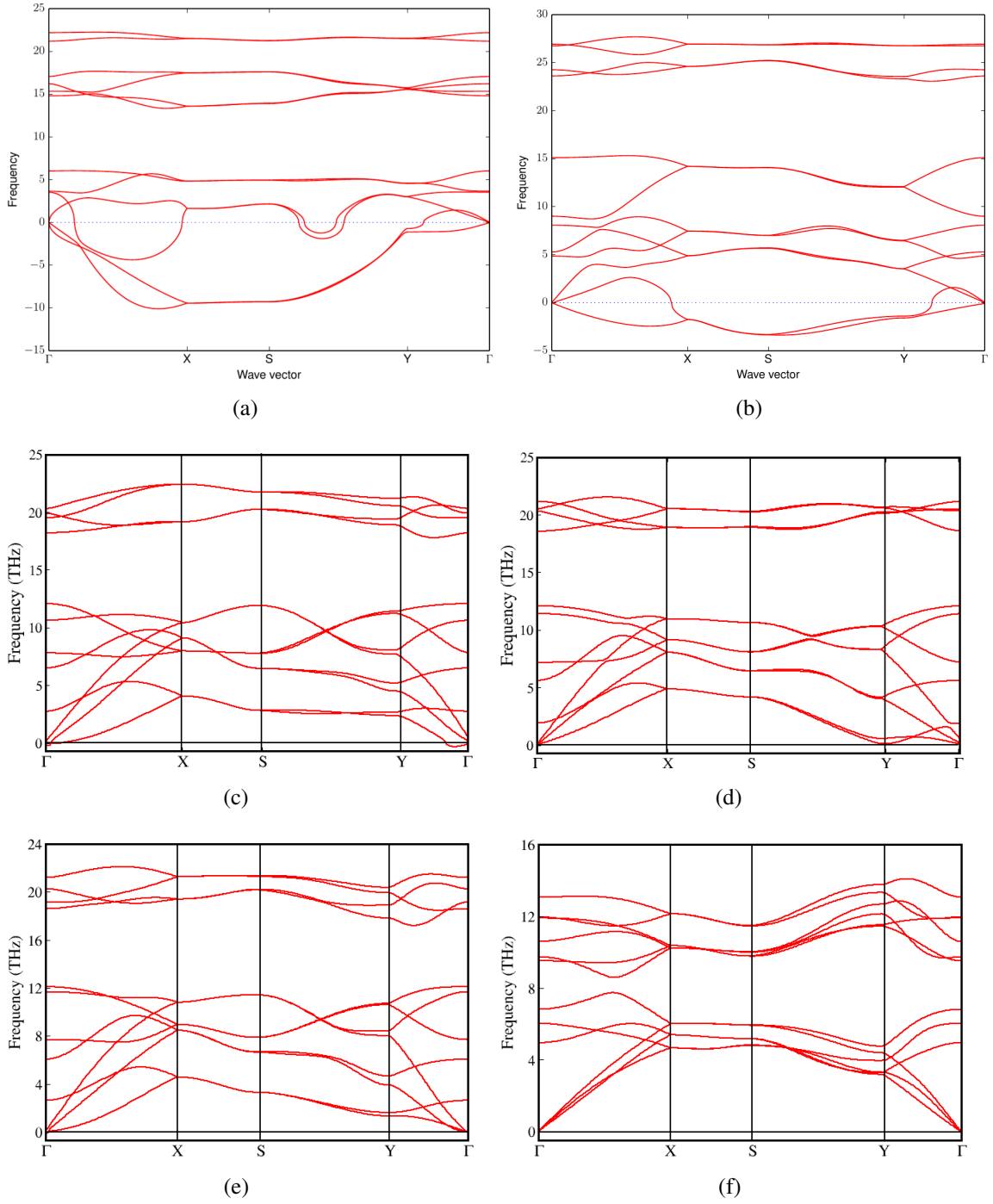
Figure 4.8: Phonon dispersion curve of SiB along different strain directions. (a)and (b) Compressive biaxial strains (c) uniaxial armchair and (d) uniaxial zigzag directions.(e) Slight negative frequency near Γ point due to biaxial tensile strain of 0.04.(f) Transition to positive phonon frequencies at the biaxial tensile strain of 0.18.

ature effects or temperature-dependent electron-phonon interactions (Sa et al. 2014).

In general, a 2D material which is buckled in its ground state and shows a negative

frequency becomes dynamically stable after a strain is applied. We did not find much discussions of this phenomenon in the literature. A similar observation was made by Wang et al., indicating a stable state of borophene in the uniaxial tensile strain state (Wang et al. 2016a). Also, Zhang et al. observed structural stability enhancement by the application of tensile strain (Zhang et al. 2017).

Further, for a biaxial tensile strain of 0.04, only a slight negative frequency appearing near the Γ point was observed, as shown in Fig. 4.8 (e). In general, two-dimensional materials are synthesized on any suitable substrate and this imparts a strain on the material. Also, note that the present calculations were performed at a temperature of absolute zero. When the temperature effect is considered, the synthesis of 2D materials is also achieved by utilizing the thermal coefficient of expansion (TEC) mismatch between the substrate and the adsorbent material. The strain engineering of 2D materials can be achieved via chemical vapor deposition (CVD) growth while simultaneously maintaining high material quality, by utilizing the TEC mismatch between the 2D material and the growth substrate. Experimentally, electron diffraction of strained monolayers grown directly onto transmission electron microscopy (TEM) windows are utilized to unambiguously quantify strain. In real applications, the residual strain usually exists in nanoscale devices, and the conduction of heat plays an important role in real-world devices (Ahn et al. 2017). Therefore, it is interesting and necessary to investigate strain effects on phonon transport in newly proposed 2D materials. Since the DFT calculation mainly deal with 0 K calculations, we studied the strain effect on SiB and found that the application of tensile strain provides structural stability to SiB. Based on the previous reports (Henkelman et al. 2006), we also concluded that the enhanced structural stability of SiB by tensile strain may shed light on the experimental fabricability of SiB on a suitable substrate.

The important observation for the biaxial strain regime is that dynamically stable SiB is observed at a tensile strain of 0.18 (see Fig. 4.8(f)), in contrast to the unstable pristine SiB. The new structural symmetry of the strained SiB is depicted in Fig. 4.9. There was a structural transition from a buckled to a flat conformation which maintained

(a)   (b)
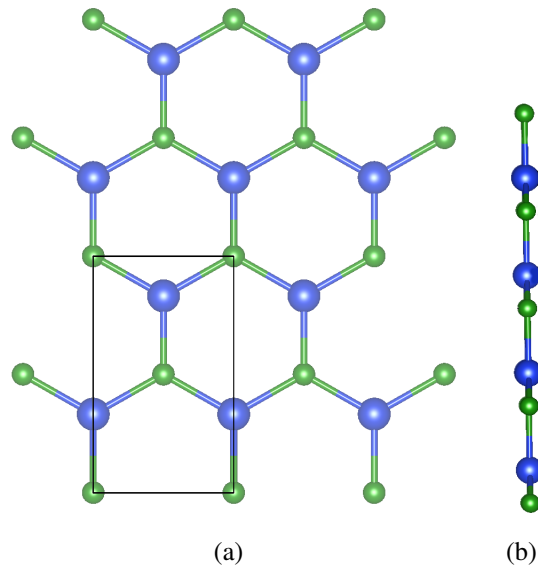
Figure 4.9: SiB in its stable new configuration. Fig. (b) showing atoms lying in a plane forming a flat conformation.
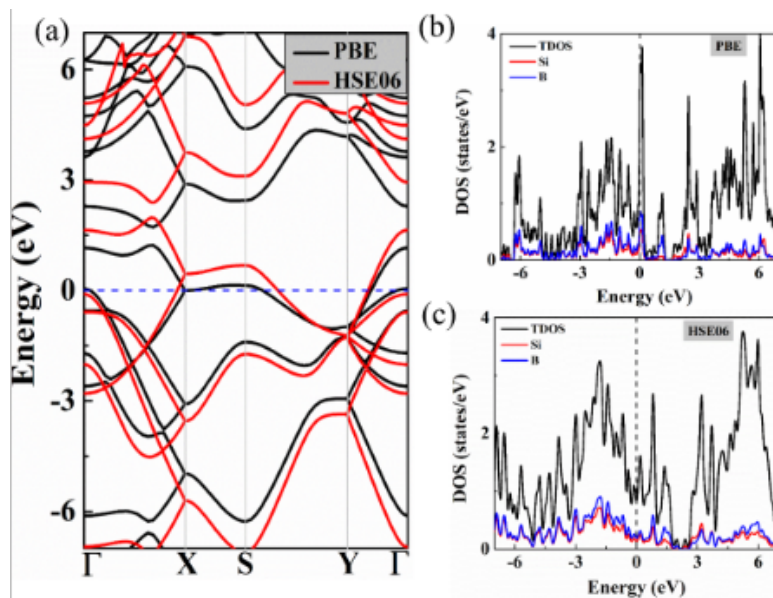
Figure 4.10: (a) Electronic band structure of the stable SiB using the PBE and HSE functional. The total and partial density of states using (b) PBE and (c) HSE functional. The electronic band and DOS analysis confirming the metallic nature of SiB.

orthorhombic symmetry. This was confirmed via phonopy which showed a difference in structure previously reported by Hansson et al. and Ding et al. (Hansson et al. 2012, Ding and Wang 2013). The new lattice parameters are a = 4.03 Å and b = 6.78 Å. The electronic band structure and density of states (DOS) plot of stable SiB are shown in

Fig. 4.10. The band structure indicates the metallic nature of SiB. One can see from the diagram that there are bands present near the Fermi level. The single conduction band starting from the Fermi level and across implies the metallic nature of SiB.
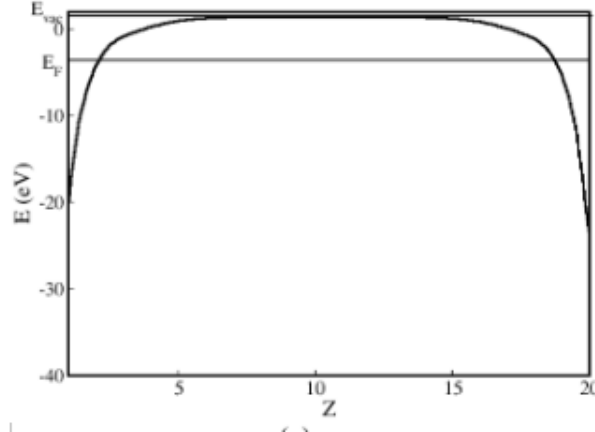
Figure 4.11: Electrostatic potential averaged along the vacuum direction plotted against the vacuum region z.

We also analyzed the work function which is defined as the minimum energy required to eject an electron from the bulk to the vacuum region outside the surface of the material at absolute zero. It can be calculated by taking the difference between the vacuum level and the Fermi level, and is given by

$$\phi = E^{vac} - \epsilon_F$$

, where E$_{vac}$ is the vacuum potential and ϵ_F is the Fermi level of the material (Ashcroft and Mermin 1976).

Knowledge of the work function is crucial in designing electronic devices. In computational and numerical calculations, the work function can be obtained by integrating the density of states from the lowest energy level to the Fermi level, thus giving the total number of electrons in the unit cell. A plot showing the electrostatic potential averaged against the vacuum direction is shown in Fig. 4.11. The Fermi level and vacuum level are marked in the figure. The vacuum potential E$_{vac}$ is the electrostatic potential averaged along the vacuum direction. The calculated value of the work function ϕ for SiB is 4.85 eV.
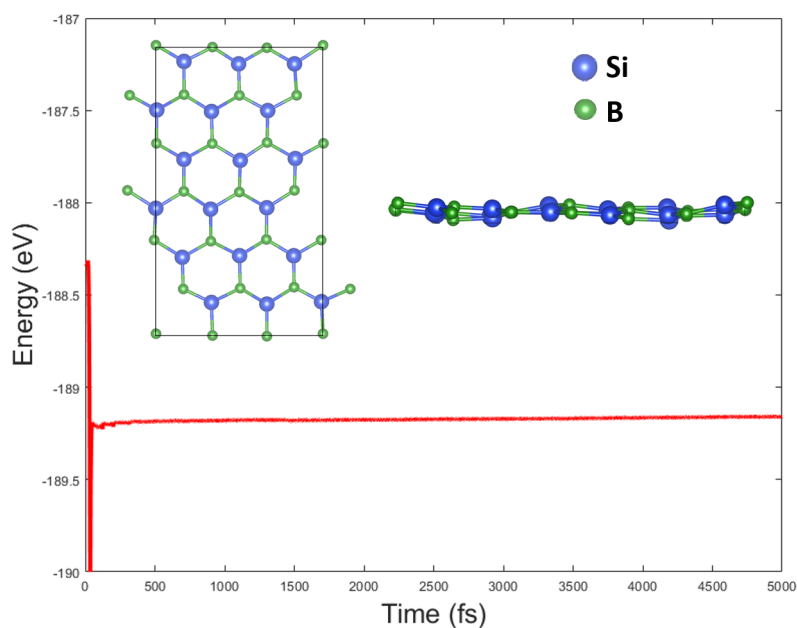
Figure 4.12: The fluctuation of the total potential energy during the AIMD simulation at 300 K for a supercell of fully lithiated SiC with Stone-Wales defect. The snapshots of the top and side views of the structure at the beginning and at the end of AIMD simulation is shown in insets.

Further, to understand the thermal stability of the new structure at room temperature, an ab-initio molecular dynamics (AIMD) simulation was carried out on a 3x3 supercell. The variation in potential energy was less than 0.2 eV, confirming the thermal stability of the new flat conformation, as shown in Fig. 4.12. Heating the system at 300 K for 5 ps led to slight buckling (0.2 Å) of the structure, without much changes in the bond length.

Chapter 5

Li ATOM ADSORPTION CAPABILITY OF PRISTINE AND DEFECTIVE SiC

First-principles density functional theory (DFT) computations are carried out to assess the potential application of a monolayer Silicon carbide (SiC) with the presence of topological and point defects. Results show that the unstable binding of pristine SiC makes it a poor candidate for the anode material. However, the introduction of vacancy and Stone-Wales type topological defect in SiC possesses a stable Li binding property. Besides, all the defective configuration showed higher electrical conductivity, superior mechanical robustness and stable formation energy. We also observed a structural re-orientation from point to topological defect with a 5-8-5 ring formation in C and Si-C bi-vacancy and a Li-mediated phenomenon in the case of Si bi-vacancy. All the configurations under consideration exhibited low open-circuit voltage (0.1 V), a low Li diffusion barrier (0.77 eV), and a fairly high specific capacity (501 mAh/g for Stone-Wales) compared to the conventional graphite anode. Besides, the ab initio molecular dynamics calculations confirmed the thermal stability and structural integrity of the defective SiC. Based on these findings, the present study suggests that SiC with a Stone-Wales defect be a forthcoming candidate for the anode of LIBs.

5.1   Li atom adsorption on pristine-SiC

Our computation correctly predicts the structural properties of SiC and the results are comparable with earlier reports using the same method. This validated our DFT method and also prompted us to follow the same approach for further analysis of SiC (Ding and Wang 2013).

A supercell of 2×2 was considered to understand the Li-ion adsorption mechanism in SiC. Li was placed at four different locations on top of SiC sheet. Li was placed on top of Si (T1), on top of C (T2), on top of Si-C bond (B), at the center of the hexagon (C) as shown in Fig. 5.1. The side views of the Li adsorption is also represented beside each of the top views. Fig. 5.1 shows geometrically optimized configurations for all the cases with a slight orientation of Li towards C rather than being at the center of the Si-C bond in the case of B (see Fig. 5.1 (c)). Each configuration was initially introduced with a single Li atom and each of them were optimized to find out the energetical stability of host SiC with Li. Insertion of Li ions onto the different positions of SiC did not show much effect on the bond length ($<$ 0.05 Å). The bond length change was only from 1.797 Åto 1.84 Å. The bond length variation occurs only on the bonds which were in the vicinity of Li ions. The cases of (a) Li on top of Si showed only a meagre change in bond length of 1.797 Å, (b) Li on top of C showed a bond length of 1.81 Å(change from original Si-C is 0.02 Å), (c) Li on top of Si-C bond showed a bond length of 1.83 Å(change from original Si-C is 0.04 Å), (d) Li in middle of the Si-C hexagon showed a change of 1.84 Å(change from original Si-C is 0.05 Å). The Li-Si distance when Li is placed on top of Si is 2.76 Å, Li-C distance when Li is placed on top of C is 2.14 Å, Li shifts towards C top from the initial position of Si-C bond after the geometrical optimization, the Li-C distance is 2.11 Åand when Li is in the middle of the hexagon, the Li-Si distances are 2.62 Å, 2.62 Å, 2.54 Åand Li-C distances are 2.54 Å, 2.54 Å, 2.23 Å. Also, insertion of Li caused a slight buckling of atoms in the case of (c) Li on top of Si-C bond (0.2 Å) and (d) Li in middle of Si-C hexagon (0.5 Å). The total energy obtained from VASP confirmed the energetical stability of all the four Li-SiC configurations and the lowest energy was found when Li was placed at the center of the
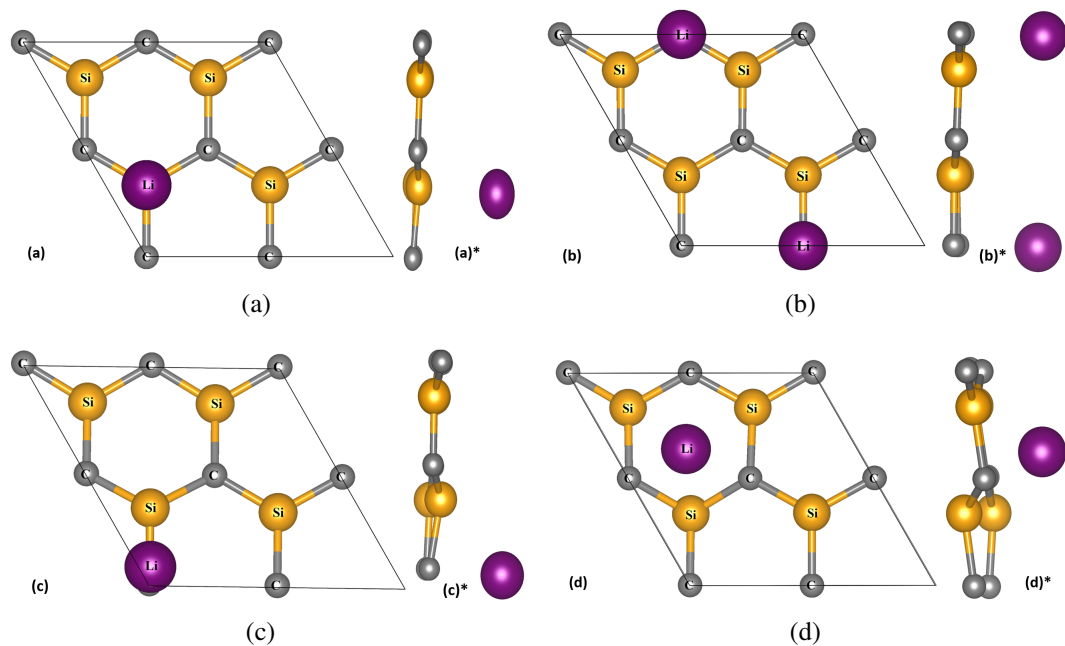
Figure 5.1: Li placed at four diferent positions on SiC. (a) Li on top of Si (b) Li on top of C (c) Li at the Si-C bond (d) Li at the middle of the hexagon and * gives the side views.

hexagon pointing to the fact that this could be the position which could have the least energy for Li adsorption which is found by determining the binding energy.

Mechanical stability and integrity of LIBs is a major concern with intercalation and de-intercalation of Li atoms. The occurrence of mechanical failure of the electrodes during the Li intercalation and de-intercalation process is a major threat for the smooth functioning of batteries. Li infusion induces stresses in the electrodes thus leading to their fracture and failure finally in the loss of battery capacity. Diffusion of Li atoms through the battery can cause phase transition, volume expansion, stresses etc. which could completely rupture the electrodes leading to battery deterioration (Wu and Zhang 2015). Li atom insertion into the host SiC can perturb the mechanical stability which can be checked by calculating the elastic constant values of Li-SiC systems. The values of elastic constants are tabulated for all the four configurations along with the values of Young's modulus and Poisson's ratio with a single Li atom (see Table 5.1).

	C_{11} (N/m)	C_{12} (N/m)	C_{22} (N/m)	C_{66} (N/m)	Y (N/m)	ν
T1	169.77	51.87	169.77	58.95	153.92	0.31
T2	156.95	53.80	156.95	51.58	138.51	0.34
B	162.31	47.97	159.13	56.08	148.13	0.3
C	145.81	33.30	135.44	51.91	138.20	0.23
Pristine SiC	179.2	54.5	179.2	62.24	162.62	0.30

Table 5.1: Elastic constants when Li is placed at T1, T2, B and C configurations

The obtained values for all the four configurations satisfy Born criteria implying the mechanical stability of Li intercalated SiC systems (Bom and Huang 1954). The values obtained were compared with the elastic values of pristine SiC. The magnitudes of elastic constants tend to decrease slightly for the Li-SiC configurations showing a slight reduction in mechanical robustness. The elastic constants C_{11} and C_{22} are equal in the case of T1 and T2 whereas it is different when its B and C configuration signifying the presence of anisotropy with the addition of Li on top of Si-C bond and in the middle of the hexagon configurations.

In order to understand the adsorption of Li on the surface of SiC, the binding energy of Li on SiC needs to be determined. The calculated values of binding energy for all the four configurations are tabulated in Table 5.2. A negative value of binding energy confirms the adsorption of Li onto the host material whereas a positive value implies a Li clustering and dendrite formation rather than adsorption (Sun et al. 2016). The positive values of binding energy in the case of SiC indicates there could be formation of Li clusters and dendrites rather than adsorption and therefore the positive value of adsorption energy for all the cases makes pristine SiC a poor material for the anode of Li-ion batteries.

	T1	T2	B	C
E_{bind}(in eV)	1.97	1.94	1.92	1.89

Table 5.2: Binding energies of T1, T2, B and C configurations of pristine SiC indicating a positive value in all the four Li atom positions.

5.2 Mono-, bi- and Stone-Wales defects and Li atom adsorption in defective SiC

Defects are ubiquitous. Most of the practical synthesis of 2D-SiC are performed at high temperatures. This would result in the formation of inevitable defects. Therefore, this section presents the changes in properties of bare 2D-SiC with the introduction of defects. There are three types of defects which are discussed here namely, mono- and bivacancy which has reduced number of atoms and are considered to be point defects and Stone-Wales type which is a topological defect preserving the number of atoms (Stone and Wales 1986). The inability of pristine SiC to be the anode urged us to look for the possible changes with the addition of defects onto the host SiC.

Defects were introduced in different ways- by removing Si, C, Si and C and Stone-Wales types. Mono-vacancy can occur by removing a single Si or C atom from the host SiC (designated as M1 and M2 respectively). Bi-vacancy occur when two Si or two C or one Si and one C atoms are removed from the host designated as B1, B2 and B3 respectively. And a Stone Wales defect is formed when a Si-C bond is rotated at an angle of 90° forming a pentagonal-heptagonal (5-7) pair in the hexagonal network (designated as SW). The structure of defective SiC along with the electron localization function (ELF) are schematically represented in Fig. 5.2.

ELF for the M1 depicts a maximum at the Si-C bond leaving a minimum at the defective region (see Fig. 5.2 (a)) whereas the absence of Si in M2 has accumulation of electrons in the defective region around the vacancy created by C as could be seen from Fig. 5.2 (b). In the defective region of bivacancy, there is minimum around the B1 whereas it shows a slight more distribution towards C atom in the case of B2 and a combination of minimum and maximum is observed in the case of B3. SW on the other hand shows an accumulation of electrons around Si pointing towards an ionic character. As a general trend observed from the ELF, there is more tendency of electrons to get accumulated around C atom, pointing towards an ionic nature. All the types of defects at the outset doesn't show any buckling and maintains a planar structure. The
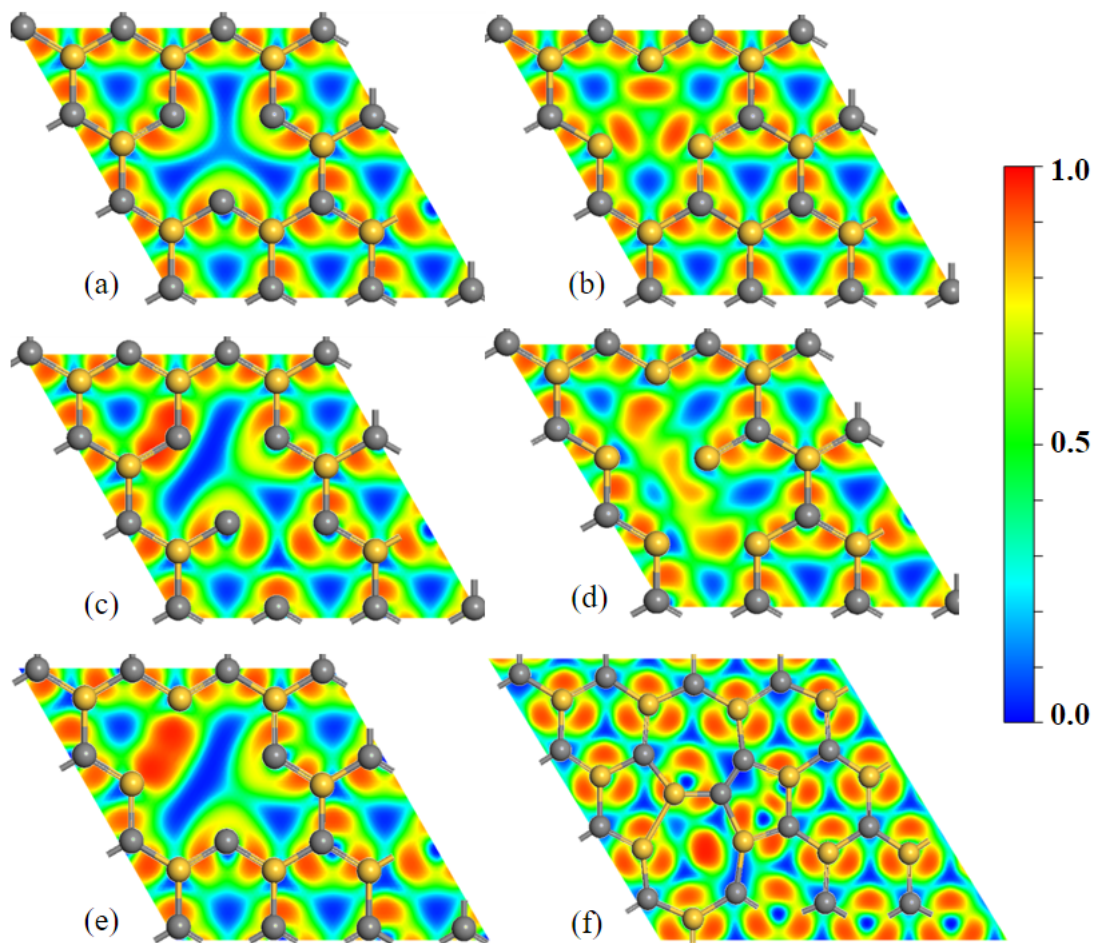
Figure 5.2: Electron localization function along with the representation of struture for (a) Si-monovacancy, (b) C-monovacancy, (c) Si-bivacancy, (d) C-bivacancy (e) Si-C-bivacancy and (f) Stone-Wales defect. Red to blue indicates the maximum to minimum electron density distribution.

obtained total energy confirms the energetical stability of all the configurations. The basic understanding on how SiC would behave with the introduction of defects on their electronic and charge density are compared with pristine SiC.

A remarkable observation in the case of bivacancy was obtained when the vacancy introduced structure was undertaken an optimization. There was a transformation from point to topological defect. The vacancy created was healed in the case of B2(C bivacancy) and B3 (Si-C bivacancy) forming a 5-8-5 ring very similar to the case of graphene (depicted in Fig. 5.3). These kind of bivacancy which is a type of multivacancy defect appear even in graphene and an extensive work on the properties of these

kinds of defects were carried out (Kochnev et al. 2014, Wang et al. 2015, Tian et al. 2017). A slight different type of healing occur in the case of Si bivacancy (B1), instead of a 5-8-5 ring structure, they reorient themselves into varied number of ring structure i.e. 5-10-7 rings. The structure of this special ring structure is given in Fig. 5.3 (c).
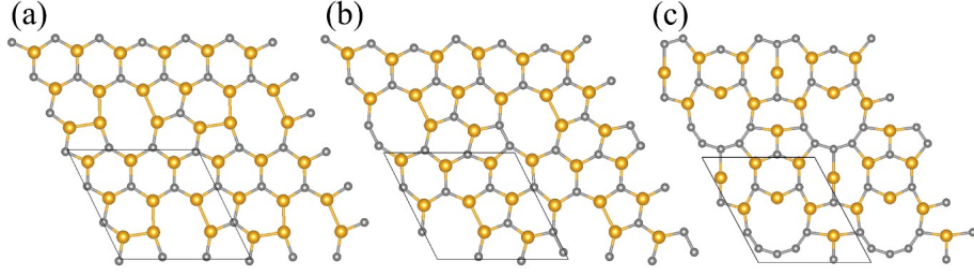
Figure 5.3: (a) and (b) 5-8-5 ring structure of C bivacancy and Si-C bivacancy, (c) 5-10-7 ring structure of Si-bivacancy

Defect formation energy is the difference in energies before and after the formation of defects. Presence of vacancy causes reduction in number of atoms thus defect formation energy can be written in the form

$$E_{form}^{vacancies} = E_{defect} - E_{perfect} + N\mu_i \tag{5.1}$$

$$E_{form}^{vacancies} = E_{defect} - E_{perfect} + nE_C + mE_{Si} \tag{5.2}$$

where E_{defect} is the total energy of the crystal having (m no. of Si), (n no. of C) vacancies in it, $E_{perfect}$ is the energy of the perfect crystal and μ_i is the chemical potential which is taken here as the total energy of graphite (E_C) and bulk silicon (E_{Si}). In the case of Stone-Wales where the number of atoms remain unaffected, the defect formation energy (E_{form}^{SW}) is calculated using the following equation.

$$E_{form}^{SW} = E_{SW} - E_{perfect} \tag{5.3}$$

Defect formation energy was determined for all the configurations and were tabulated in Table 5.3. The values of SiC are compared with that of graphene and silicene. Formation energy values of SiC in the case of Si-monovacancy (M1) shows a slightly lesser

value compared to graphene whereas M2 and bivacancy type shows higher magnitudes. Comparing the E_{form} of SW on the other hand shows low value compared to both mono-vacancy and bivacancy implying that the formation of SW defect is thermodynamically favored over mono and bi vacancies. We also noticed that the computed E_{form} of SiC with SW defect is smaller than that of graphene, h-BN and BCN and higher than that of silicene. Besides, as shown in Table 5.3, the computed defect formation energy of SiC is comparable and or smaller compared to that of experimentally synthesized h-BN and BCN 2D materials (Thomas et al. 2015) implying that these structures are more accessible to an experimental group.

	SiC (E in eV)	Graphene* (eV)	Silicene*(eV)
Monovacancy	M1=7.26		
	M2=6.22	7.62	2.87
Bivacancy	B1=6.40		
	B2=8.22		
	B3=5.42	7.48	3.24
Stone-Wales	4.23	4.87	1.84

Table 5.3: Defect formation energies of SiC compared with graphene and silicene

Pristine SiC is a wide band gap semiconductor as depicted in Fig. 3.7. The bands diagram for all the defective configurations are plotted in Fig. 5.4. Fig. 5.4 (a) and 5.4 (b) represents the band diagram for M1 and M2 configurations. Fig. 5.4 (c), 5.4 (d) and 5.4 (e) represents the band diagram for B1, B2 and B3 configurations and 5.4 (f) represents the band structure for SW configuration. The band diagram for M1, M2, B1 and B2 configurations show a metallic nature confirming a semiconducting-metallic transition. The bands which were away from the Fermi level in the pristine SiC came closer to the Fermi level with few bands overlapping with each other and falling into the conduction band. B3 on the other hand, shows a very low band gap of 0.4 eV and SW shows a band gap of around 1 eV but much less than pristine SiC. The direct nature of pristine SiC is now changed to an indirect band gap nature when the defects are SW. The lowest of conduction band lie at Γ point and the highest of valence lie at K thus making it an indirect band gap semiconductor.
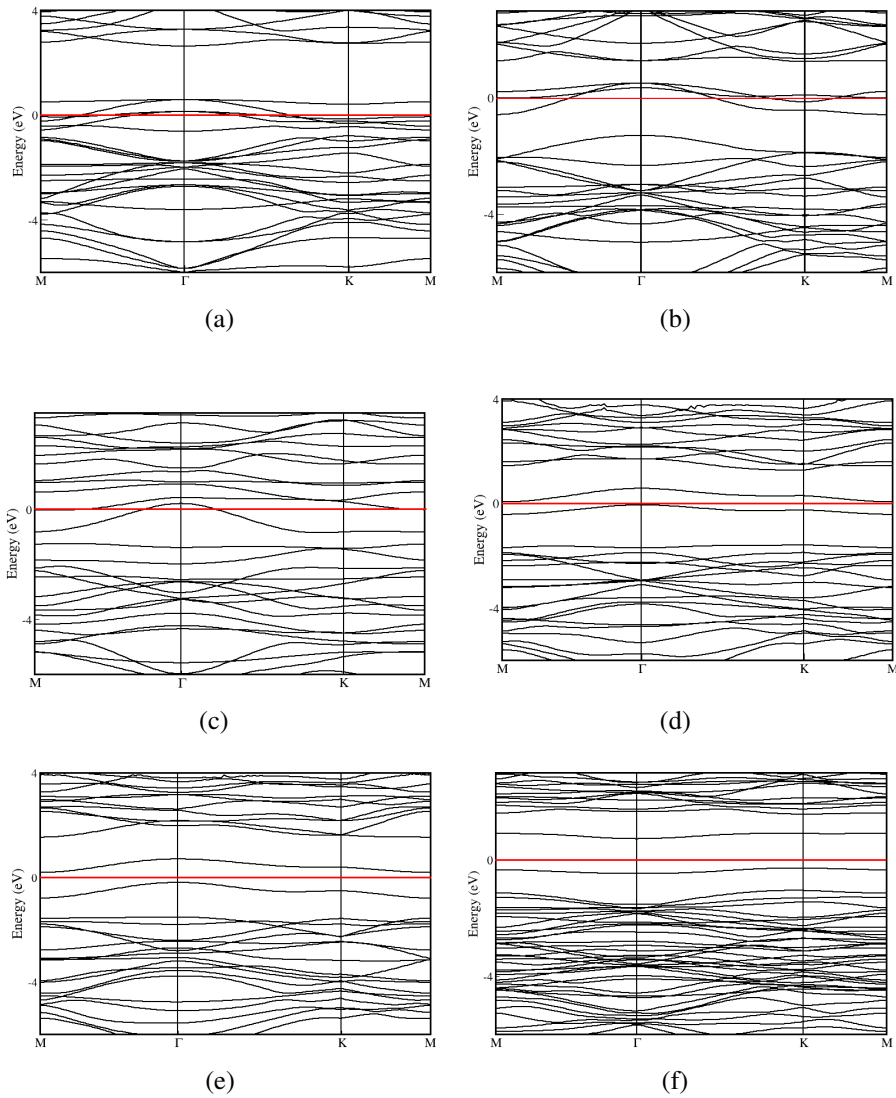
Figure 5.4: Electronic band structure for Monovacancy (a) Si removed (b) C removed, Bivacancy (c) 2Si removed (d) 2C removed (e) 1Si-1C removed, (f) Stone-Wales defect. (a) - (d) characterizes metallic nature and (e) and (f) characterizes semiconducting nature. The horizontal red line is the Fermi level maintained at zero.

Electronic density of states (DOS) plot along with partial DOS contribution for all the vacancy configurations are depicted in Fig. 5.5. Compared to the pristine SiC which was semiconducting, all the mono- and bi- vacancy (except B3) depicted in Fig. 5.5 showed metallic nature as seen also from the electronic bands diagram. DOS plot in the case of B3 and SW showed empty DOS at the Fermi level. In the pristine case, the contribution near the Fermi level was notably from the p_z orbitals of both Si and C. With the creation of monovacancy, the p orbitals namely p_x, p_y and p_z of both Si and

C approaches towards the Fermi level causing a decrease in band gap finally making it metallic. In the case of bivacancy, the major contribution in the Fermi level region is from the Si(p_y), C(p_y) and C(p_z) converting semiconducting SiC to metallic. Thus, vacancy creation is a feasible method for the tuning of band gap in 2D-SiC.
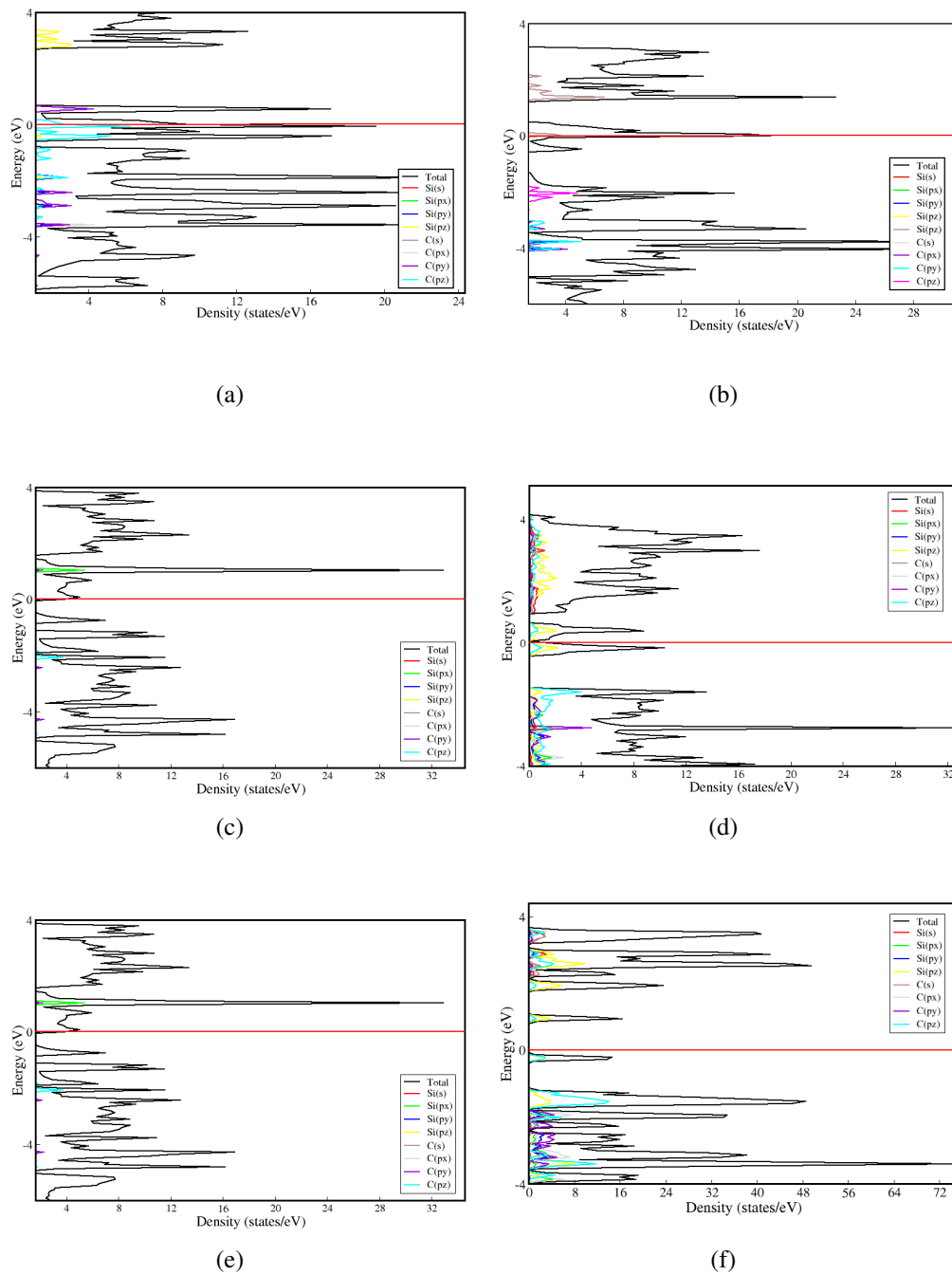
Figure 5.5: Electronic dos structure for Monovacancy (a) Si removed (b) C removed, Bivacancy (c) 2Si removed (d) 2C removed (e) 1Si-1C removed, (f) Stone-Wales defect
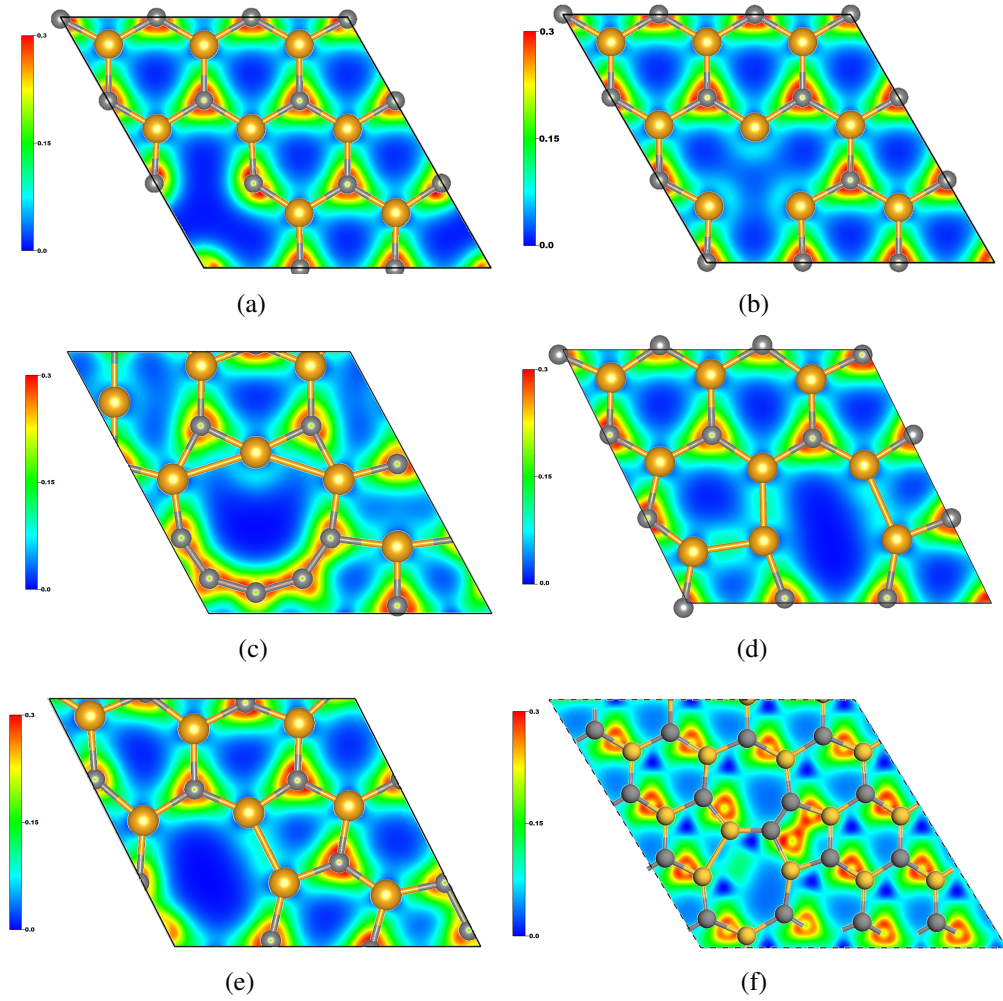
Figure 5.6: Charge density contours (a) Si-monovacancy (M1), (b) C-monovacancy (M2), (c) Si-bivacancy (B1), (d) C-bivacancy (B2), (e) Si-C bivacancy (B3) and (f) SW. Contour plot of all the defective configurations confirming the ionic nature in general.

Charge density contour was plotted for all the vacancy induced configurations along with the confirmation using Bader charge analysis (Henkelman et al. 2006). The contour plots are depicted in Fig. 5.6. Charge density contours at the outset shows an accumulation of charges around C atom with a reduced distribution slightly farther away from the atom. Monovacancy configurations show maximum distribution around C ($8/\text{Å}^3$) and zero at the defective region. Bader analysis shows a complete ionic nature in the case of M1 and a slight magnitude of charge is observed on Si atoms ($1/\text{Å}^3$) but being the greater on C atoms in the case of M2. In the case of bivacancy, much variation in charge distribution pattern is not observed but still charges tend to spread more compared to the monovacancy configurations as B1 has a charge density of $1.31/\text{Å}^3$ around

Si and 5.28/Å^3, 7.98/Å^3, 8.23/Å^3 around C atoms, B2 has a distribution of 1.11/Å^3, 2.98/ Å^3 around Si and 7.98/Å^3, 8.04/Å^3 around C, B3 has 1.12/Å^3 around Si and 6.86/Å^3, 7.95/Å^3, 8.03/Å^3 around Si atom. And the Bader analysis shows a tendency of few charges to slightly move towards and accumulates around Si atoms (2.40/Å^3) but the ionic nature is predominant in general which is also the case with SW (6.77/Å^3, 8.02/Å^3 around C atom).
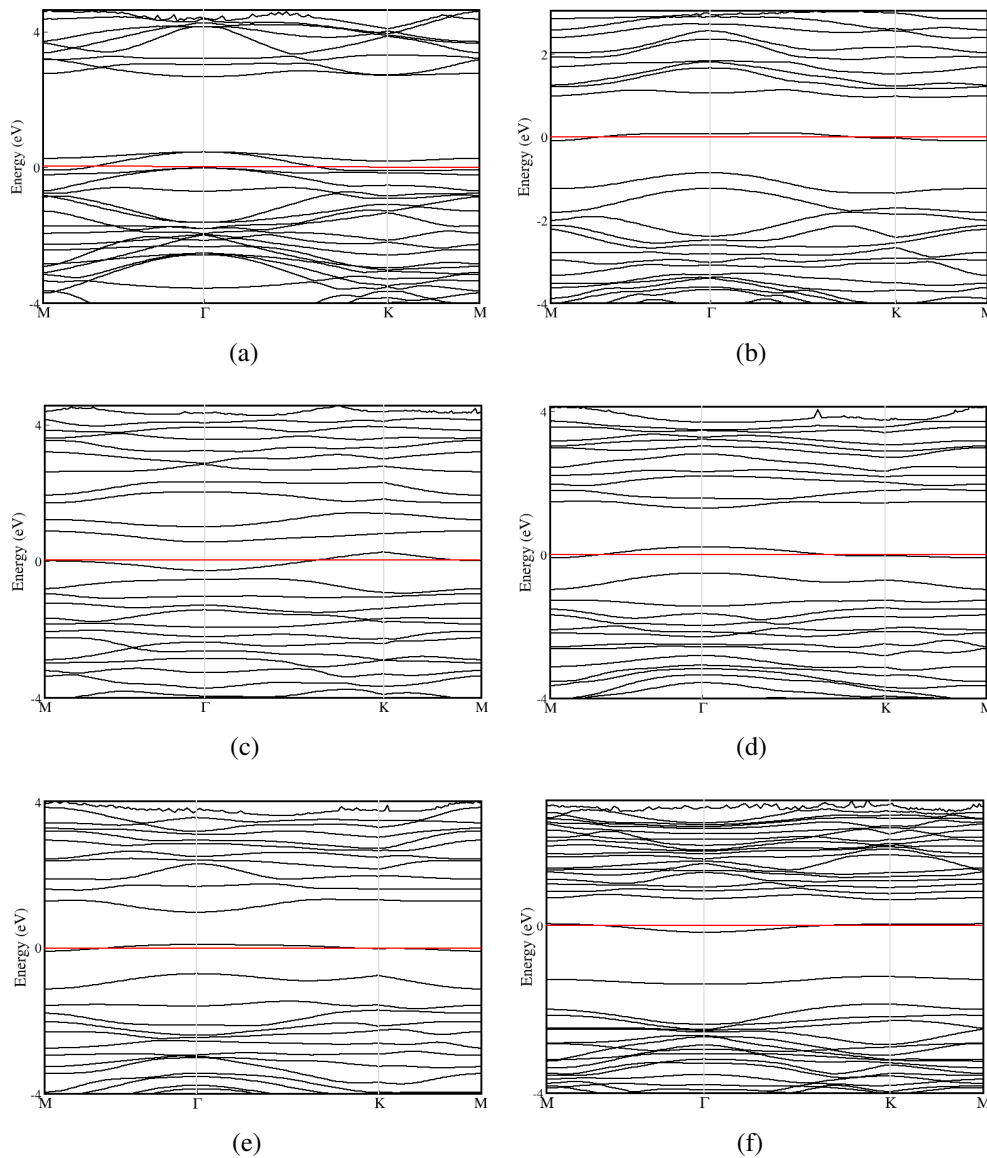
Figure 5.7: Electronic bands plot with the presence of Li for Monovacancy (a) Si removed (M1) (b) C removed (M2), Bivacancy (c) 2Si removed (B1) (d) 2C removed (B2) (e) 1Si-1C removed (B3), (f) Stone-Wales defect (SW)

We noticed that the charge transfer from Li to the SiC monolayers is $\sim 0.9 \, |e|$ leading to the substantial shifting of the Fermi energy level, which also ensures the semiconductor to metal transition during Li adsorption. Thus the observed transformation from semiconducting to metallic in the case of mono- and bivacancy and also the reduction in band gap for SW results in higher electrical conduction in defective SiC. This reduction in band gap would in turn make it a plausible material for the anode of LIBs compared to the bare SiC. So, to figure out the adsorption pattern of Li ions, the binding energy was calculated for all the defective configurations (see Table 5.5). A negative value of binding energy indicates the adsorption of Li ions onto the SiC surface rather than the Li cluster formation. This also means that the adsorption process is spontaneous and exothermic which is vital for the functioning of LIBs. According to the above criterion, Li would get adsorbed onto the surface of all the studied defective configurations without Li metal cluster formation. Among the monovacancy defected configurations, Si-monovacancy (M1) has a higher binding energy implying a strong binding of Li with M1 host than the C-monovacancy (M2) configuration. In the case of bivacancy, C-bivacancy (B2) appears to be having higher binding energy compared to Si-bivacancy (B1) and Si-C-bivacancy (B3). Stone-Wales (SW) have the least value of adsorption energy compared to mono- and bivacancy. Now, to understand the effect of Li on the defects, electronic bands of all the configurations were plotted. The bands diagram are as depicted in Fig. 5.7. Metallic nature portrayed by M1, M2, B1 and B2 is maintained as such and B3 and SW is now transformed into metallic with the addition of Li.

Now, a notable observation was made with the addition of Li atom into Si-bivacancy structure (B1). The addition of Li atom causes a structural reorientation of the 5-10-7 rings in B1 and forms a 5-8-5 ring structure as in C-bivacancy (B2) and Si-C-bivacancy (B3). It is interesting in the case of Si-bivacancy because this reorientation is a Li-mediated transformation. So, Li acts as an agent which helps in reorienting the ring structure to form a stable 5-8-5 ring structure in the case of Si-bivacancy configuration. And the other two types of bivacancy maintains the 5-8-5 ring structure with the insertion of Li atoms into it. The structure of this new ring conformation with Li inserted are depicted in Fig. 5.8.

Figure 5.8: Figure showing the 5-8-5 rings after the addition of Li into the host matrix for the three bivacancy configurations. (a) B1, (b) B2 and (c) B3. 5-8-5 rings of B2 and B3 remain unaffected with the introduction of Lis into it. B1 attains the stable 5-8-5 rings with the Li mediation. Yellow, grey and green atoms represent Si, C and Li respectively.

An insight into the mechanical properties are crucial in developing structures for practical applications thus providing an information on the mechanical strength of the material (Wang et al. 2012b). Determination of second order elastic constants (SOEC) are necessary for understanding the mechanical stability of any material thus modelling the linear elastic response. Second order elastic constants of all the six configurations are determined to understand the effect of Li on the mechanical stabilities of defective SiC. The magnitudes of elastic constants along with Young's modulus and Poisson's ratio are tabulated in Table 5.4. The computed values of elastic constants satisfy the Born stability criteria signifying the mechanical stability of all the configurations with the presence of Li atom. The elastic constants in general shows mechanical robustness in all the configurations under consideration. The values of defective SiC are compared with pristine SiC which indicates a reduction in magnitude of SOEC suggesting

a reduction in mechanical stability with the insertion of Li. Carefully observing these values suggest an isotropic behaviour in the case of M1 defect with $C_{11} = C_{22}$ and an anisotropic behaviour is observed in all the other configurations in which $C_{11} \neq C_{22}$. For the monovacancy cases specially M1, the Poisson's ratio is nearly 0.5 (0.51 for M1) signifying the incompressible nature meaning there will be no volume change under any applied deformation which is a positive gesture that can be utilized in battery applications, also higher Poisson's ratio is observed in the case of M2 and SW. But bivacancy cases, show reduced value of Poisson's ratio nearing 0.1, pointing to the fact that there is very less transverse expansion when compressed. Observing the magnitudes of SOEC implies higher mechanical robustness in the case of SW in comparison to all the mono- and bivacancy configurations. From the earlier work on defective planar carbon allotropes (Thomas et al. 2019) and BC3 monolayer (Thomas et al. 2020), we found that the computed elastic constants satisfy the criteria for mechanical stability; but experienced a reduction in the mechanical stiffness after Li intercalation. The same trend is also observed in the case of SiC with SW and vacancy defects and the details are presented in Table 5.4.

	C_{11} (N/m)	C_{12} (N/m)	C_{22} (N/m)	C_{66} (N/m)	Y (N/m)	ν
M1	89.38	45.60	89.38		66.12	0.51
M2	77.15	30.69	83.21	33.8	64.94	0.40
B1	118.42	13.64	56.74	39.80	116.85	0.12
B2	115.44	8.03	59.49	33.23	114.88	0.07
B3	109.93	11.32	70.30	39.00	108.76	0.10
SW	162.02	51.53	169.15	55.42	145.63	0.32
Pristine SiC	179.2	54.50	179.2	62.24	162.7	0.3

Table 5.4: Elastic constants of defective SiC with the insertion of Li - Mono-vacancy (M1, M2), bi-vacancy (B1, B2, B3) and Stone-Wales (SW) defect configurations.

Specific capacity is very crucial to consider a material as an anode of LIBs. Capacity in general was determined for all the six configurations under consideration. Li was added one by one to the defective SiC matrix and the binding energy for each configuration were calculated. For the monovacancy case, the structures showed buckling
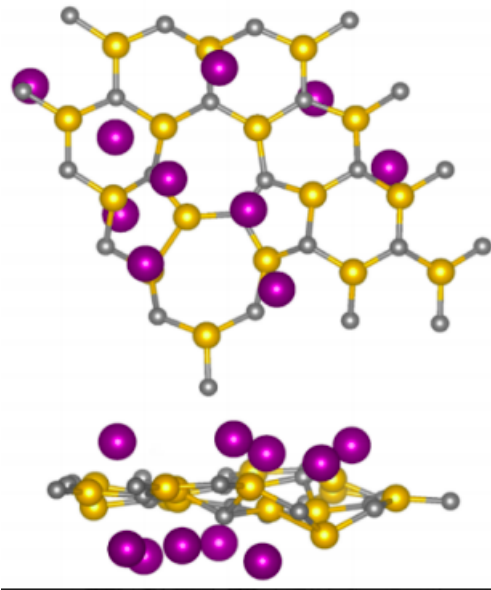
Figure 5.9: Top and side views of SiC with a SW defect which accommodate a total of ten Li atoms above and below the SiC sheet.

of atoms with Li insertion and a maximum of nine Li atoms were added above and below the host defective SiC matrix with least distortion of the lattice. A maximum of eight Li atoms was inserted into the ring structures of bivacancy defective configurations with negative adsorption energy for all the studied cases. In the case of SW, the maximum Li atoms inserted was around twelve and the adsorption energy showed negative for all the cases (see Fig. 5.9). All the studied configurations show superior capacity (see Table 5.5) as compared to the conventional graphite anode (372 mAh/g), MoS2/graphene (338 mAh/g), Ti3C2 monolayer (320 mAh/g), and Mo2C (526 mAh/g) (see also Appendix D) (Dahn et al. 1995, Sun et al. 2016, Tang et al. 2012, David et al. 2014). Among all the defects, Si-monovacancy showed highest capacity with maximum adsorption of nine Li atoms in the stiochiometry Li9Si8C9. Least value of binding energy for Si monovacancy corresponding to the highest value of capacity. The average open circuit voltage (OCV) obtained in the case of all the configurations are also tabulated in Table 5.5 which is in accordance with the LIBs requirements. The capacity of the above studied defective SiC being superior and low OCV and its successful experimental synthesis would make it an appropriate forthcoming material for the anode of future Li-ion batteries. However, the basic understanding of mechanical properties, electrical conduction, and adsorption energy along with the defect formation energy

78

point towards the possibility of Stone-Wales defect induced 2D-SiC to be a superior candidate among all the configurations under consideration. To understand the dynamical stability of Stone-Wales defective configuration, a density functional perturbation theory (DFPT) calculation was carried and the post processing of the data was carried out using PHONOPY code. The phonon dispersion curve obtained from the calculation showed real frequencies of all phonon modes for all the wave vectors implying the dynamical stability of Stone-Wales introduced SiC configuration. The graph representing the phonon-dispersion curve is given as Fig. 5.10.

	E_{bind} (eV)	Capacity (mAh/g)	OCV (V)
M1	-3.03	725	0.33
M2	-1.41	691	0.46
B1	-1.81	616	0.66
B2	-2.27	637	0.33
B3	-0.94	668	0.10
SW	-0.60	501	0.11

Table 5.5: Binding energy, theoretical capacity and average OCV for all the defective configurations.
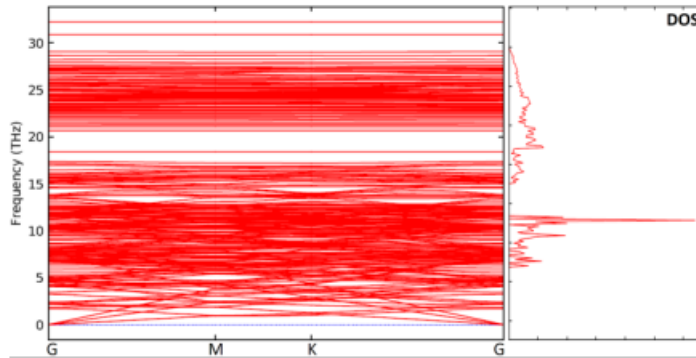
Figure 5.10: Phonon dispersion spectrum and the density of states of SiC monolayer with a Stone-Wales defect.

In order to further understand the Li ion movement mechanism and the corresponding diffusion barriers, a nudged elastic band method was carried out only for Stone-Wales (SW) configuration. The NEB pathway is as represented in Fig. 5.11. We investigated
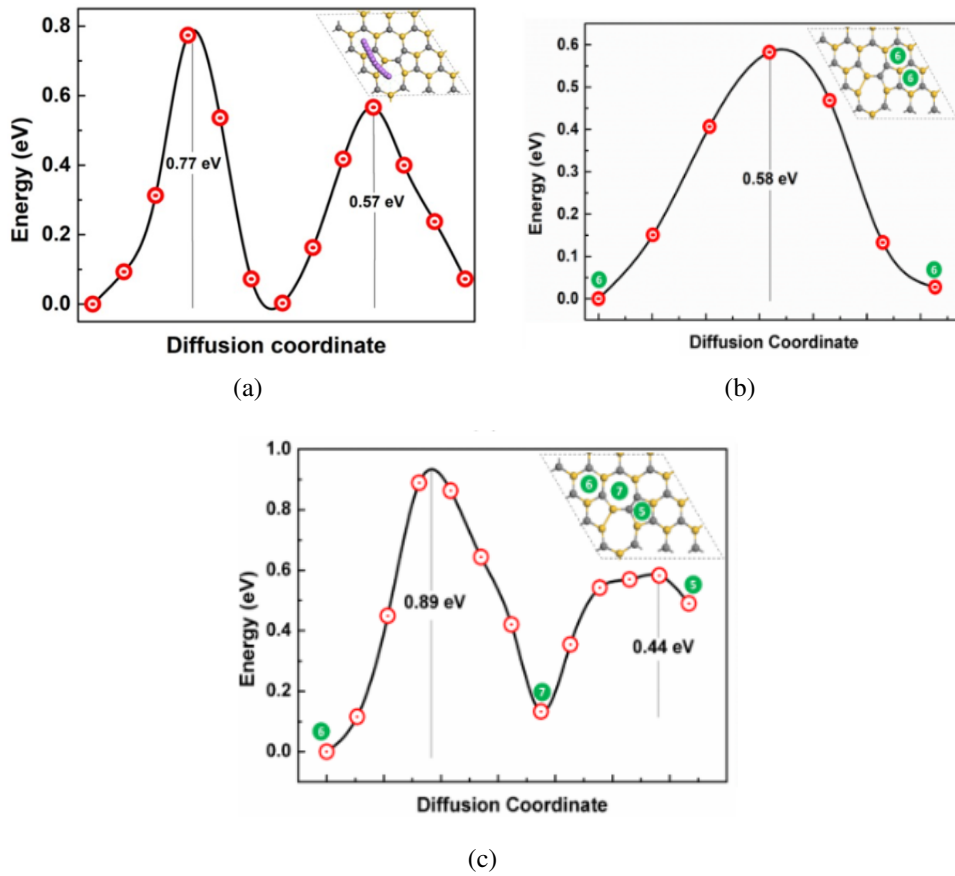
Figure 5.11: Minimum energy path for the diffusion of Li atom through (a) Si-monovacancy, (b) C-bivacancy and (c) Stone-Wales defect.

the Li migration through different ring positions (5,6, and 7 membered rings corresponding to the pentagon, hexagon and heptagon in the SW defect) and found there exist slight distortion to the host SiC, The computed diffusion barrier heights from 6 to 5 is 0.77 eV and 5 to 7 is 0.57 eV which is slightly higher than that of graphene (0.31 eV) but lower than that of other two dimensional materials like phosphorene, defective silicene, BC3 nanotubes, etc. (Setiadi et al. 2013, Hardikar et al. 2014, Zhao et al. 2014, 2005). We also considered all other possible diffusion paths through SiC- SW (Fig. 5.11) and found that the Li may prefer the most stable and lowest energy barrier path (0.57 eV) during the diffusion process.

We also investigated the average volume change in the xy plane of SiC with Stone-Wales defect in the fully lithiated state and found that the volume change is about 1.49% indicating an insignificant volume change. One of the major benefits of low contraction
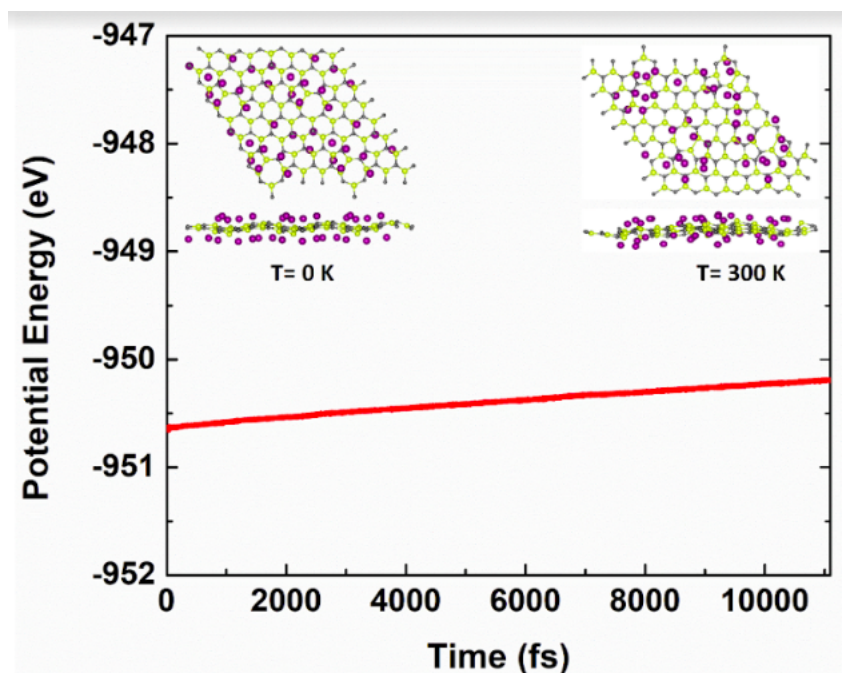
Figure 5.12: (a) The fluctuation of the total potential energy during the AIMD simulation at 300 K for a 2×2 supercell of fully lithiated SiC with Si monovacancy (M1). The snapshots of the top and side views of the structure at the (b) beginning and (c) at the end of AIMD simulation.

in electrode materials upon Li intercalation or low volume changes is that a large number of charge/discharge cycles can be attained along with negligible capacitance loss. Since the insertion of Li atoms into the defective structure showed buckling, an ab-initio molecular dynamics (AIMD) simulation was performed to understand the thermal stability of the Li added configuration only for the case of Stone-Wales defect type (SW). A supercell containing a total of 168 atoms (64 Silicon, 64 Carbon, and 40 Lithium) for 10 picoseconds were considered to carry out the simulation. The fluctuation of the total potential energy during the AIMD simulation at 300 K was computed using the NVT ensemble with the Nose-Hoover heat bath method (See Fig. 5.12). We found that the fully lithiated SiC monolayer with Stone-Wales defect type is energetically and thermally stable with energy fluctuations within 1 eV. Also after heating up the system at 300K for 10 ps, the Li atoms are well dispersed on both sides of the fully lithiated SiC monolayer (see insets of Fig. 5.12). This observation suggests its structural integrity and further LIB application in the battery operating temperature.

81

Chapter 6

SUMMARY, CONCLUSIONS AND FUTURE WORK

This chapter summarizes the important findings along with the major conclusions of the present research work. In addition to that the scope of the future work is also included in the present chapter.

6.1   Summary

From the results and discussions of Chapters 3,4,5, it can be summarized as :

The past two decades have seen tremendous advancements in the prediction and synthesis of two dimensional materials having novel electronic, chemical, mechanical, optical and magnetic properties and their potential applications in various fields including mechanical engineering, electronics, information and energy technologies. In this thesis, an attempt have been done to understand the potential of two dimensional SiC in being the anode of Li-ion batteries along with understanding its behavioural changes with the application of strain. Strain has also been applied to two dimensional SiB and efforts are done to find out if a stable SiB structure could be obtained with the application of strain.

Chapter 3 : Stress was applied on SiC to understand the change in its structural, mechanical and electronic behaviours. SiC is energetically stable in the studied stress

82

range for both compressive and tensile regime. The uniaxial zigzag and armchair stress changes the structure and symmetry of the system from hexagonal to orthorhombic whereas biaxial stress maintains the hexagonal symmetry. The mechanical stability of the system was studied in terms of the magnitudes of second order elastic constants. SiC shows considerable stability with uniaxial zigzag, armchair and biaxial stresses and showed anisotropic behaviour along different directions and along the strain grids from -0.1 to 0.1. The band gap tuning of SiC was achieved using stress thus transforming the material from direct to indirect band gap semiconductor. Application of stress also reduces the band gap making the system metallic. Thus, inducing stress is an efficient way to easily tune the band gap of materials. Charge density plot and Bader analysis confirmed the ionic nature of SiC in two dimension.

Chapter 4 : Here, we propose a new flat conformation of SiB having orthorhombic symmetry. The strain energy and elastic constants data implied anisotropic behavior of SiB in the studied ranges of strained states. The second order elastic constants showed that SiB has superior mechanical strength and ultimate tensile strength compared to its counterpart silicene. SiB in its undeformed state is ionic in nature and becomes covalent with the application of uniaxial zigzag and biaxial strains. SiB in its original pristine form showed dynamical instability but was transformed to a dynamically stable configuration with the application of biaxial tensile strain. The ab-initio molecular dynamics simulation further confirmed the thermal stability of the new flat conformation. This material was also observed to attain stability with the application of uniaxial tensile strains.

Chapter 5 : Density functional theory calculations were done on pristine SiC to check its capability in being the anode of Li-ion batteries. Li was positioned at various points on the surface of SiC and addition of Li onto the pristine SiC implied energetical stability for all the Li positions. Elastic constants for all the configurations implied mechanical robustness. Determination of binding energy suggests the possible candidature of a material and pristine SiC proved to be a poor candidate due to the positive binding energy. This was then introduced with defects and the properties were evaluated. Electronic bands plots for the defective configurations showed improved electrical con-

duction with a transformation from semiconducting to metallic nature thus implying higher electrical conduction. Elastic constants showed mechanical stability of the defective structures along with the indication of presence of anisotropy with the introduction of defects. A remarkable observation in the case of bivacancy configurations was the structural reorientation with the formation of stable 5-8-5 rings healing the vacancy created in the case of C-bivacancy and Si-C-bivacancy making a transition from point defect to topological defect. Li mediated reorientation occurs in Si-bivacancy forming 5-8-5 rings from the 5-10-7 ring structure. Negative binding energy, higher specific capacity, low OCV and low diffusion barrier (0.77 eV) computed for all the configurations gives an outlook for its capability in being the anode of LIBs. Thermal stability of Stone-Wales (computed for SW only) was proved with the insertion of Li atoms on either side of the monolayer sheet through ab-initio molecular dynamics calculations. Therefore, considering all the above results we conclude 2D-SiC in particular SW to be a plausible and competent material to be the anode of next generation Li-ion batteries.

6.2   Conclusions

The major conclusions drawn from the present research work is that SiC is proposed to be a prospective candidate for the anode of future Li-ion batteries because of its mechanical stabilities in varied strain regimes, improved electrical conduction with strain and defects, dynamical and thermal stability, higher specific capacity, low open circuir voltage. Also, the present work proposes a new stable flat configuration of unstable buckled SiB with the introduction of tensile strain.

6.3   SCOPE FOR THE FUTURE WORK

Efforts can be made in future

- Introduce SiB with point and topological defects and identify if this can be a potential candidate to be the anode of Li-ion batteries.

- To understand the effect of uniaxial strain on the monolayer BC_3 which have been

analysed for its response towards biaxial strain.

- Pristine monolayer BC_3 is identified as a candidate for the anode of Li-ion batteries. So, this can be introduced with point and topological defects and their capability in being the anode can be identified.

- Apply strain in all the silicene derivatives which are dynamically unstable and identify if there is any possibility in having a phonon stable structures.

Appendices

Appendix A

Hohenberg-Kohn theorem 1

Statement : The ground state energy determined from the Schrödinger equation is a unique functional of electron density.

Proof : The assumption is that there exist two potentials $V_{ext}^1(\vec{r})$ and $V_{ext}^2(\vec{r})$ which differs by more than a constant and giving same ground state density $n(\vec{r})$. The two potentials have diferent Hamiltonians corresponing to different wavefunctions i.e. $H_{ext}^1(\vec{r})$ and $H_{ext}^2(\vec{r})$ corrsponding to $\Psi_{ext}^1(\vec{r})$ and $\Psi_{ext}^2(\vec{r})$ respectively. No other wavfunction can provide lesser energy than $E^{(}1)$ corresponding to $H_{ext}^1(\vec{r})$ and $\Psi_{ext}^1(\vec{r})$ according to the Variational principle meaning

$$E^{(1)} = \left\langle \Psi^{(1)} \middle| H^{(1)} \middle| \Psi^{(1)} \right\rangle < \left\langle \Psi^{(2)} \middle| H^{(1)} \middle| \Psi^{(2)} \right\rangle$$

The ground state is not degenerate which means this inequality strictly holds. Now, because we have similar ground state density for both Hmailtonians, we can write the expectation value as

$$E^{(1)} < \left\langle \Psi^{(2)} \middle| H^{(1)} \middle| \Psi^{(2)} \right\rangle = \left\langle \Psi^{(2)} \middle| H^{(2)} \middle| \Psi^{(2)} \right\rangle + \int d\vec{r}[V_{ext}^1(\vec{r}) - V_{ext}^2(\vec{r})]n_0(\vec{r})$$

Writing it similarly for $H_{ext}^2(\vec{r})$ gives

$$E^{(2)} < \left\langle \Psi^{(1)} \middle| H^{(2)} \middle| \Psi^{(1)} \right\rangle = \left\langle \Psi^{(1)} \middle| H^{(1)} \middle| \Psi^{(1)} \right\rangle + \int d\vec{r}[V_{ext}^2(\vec{r}) - V_{ext}^1(\vec{r})]n_0(\vec{r})$$

Adding both the equation gives

$$E^{(1)} + E^{(2)} < \left\langle \Psi^{(2)} \middle| H^{(2)} \middle| \Psi^{(2)} \right\rangle + \left\langle \Psi^{(1)} \middle| H^{(1)} \middle| \Psi^{(1)} \right\rangle$$

$$E^{(1)} + E^{(2)} < E^{(2)} + E^{(1)}$$

This is a contradiction proving the first Hohenberg-Kohn theorem which states that there cannot be two potentials yielding the same ground state electron density.

Appendix B

Hohenberg-Kohn theorem 2

Statement : It is the ground state electron density that minimizes the total energy of the system corresponding to the full solution of the Schrödinger equation

Proof : The exact ground state electron density is obtained by minimizing the total energy of the system which is a functional of the ground state electron density. Hohenberg and Kohn defined a universal functional which is valid for any system, regardless of their external potential.

Therefore, for a given external potential $V_{ext}(\vec{r})$, we have the total energy functional E[n] defined as

$$E[n] = F[n] + \int v(\vec{r})n(\vec{r})d\vec{r}$$

Here interaction energy from nuclei is neglected and the universal functional F[n] contains all of the electronic energy :

$$F[n] = T[n] + V_{ee}[n]$$

Where T[n] is the kinetic energy functional and V_{ee}[n] is the potential energy functional from e^--e^- interactions.

For a system with ground state electron density n($\vec{r}$), the ground state energy will be equal to the total energy functional E[n], whicch is the expectation value of the Hamiltonian for the ground state wave function Ψ

$$E = E[n] = \langle \Psi | \hat{H} | \Psi \rangle \tag{6.1}$$

For a different density n'($\vec{r}$) and with Ψ', it follows from the variational principle that the energy corresponding to this state E' would be greater than the ground state energy E

$$E = \langle \Psi | \hat{H} | \Psi \rangle < \langle \Psi' | \hat{H} | \Psi' \rangle = E' \tag{6.2}$$

This means the total energy functional E[n] gives the exact ground state energy only for

the exact ground state density. If one knows the universal functional F[n], then the total energy can be minimised with respect to $n(\vec{r})$ and the exact ground state energy density and total energy can be obtained.

Appendix C

Hellmann-Feynman Theorem

The derivative of energy with respect to any parameter say λ, can be determined by the expectation value of derivative of Hamiltonian with the same parameter λ. Mathematically it can be written as,

$$\frac{\partial E}{\partial \lambda} = \langle \psi(\lambda)| \frac{\partial H}{\partial \lambda} |\psi(\lambda)\rangle \tag{6.3}$$

Proof : Consider a system having a Hamiltonian H which is a function of some parameter say λ. $\psi(\lambda)$ is the eigenfunction and E(λ) is the eigenvalue of the Hamiltonian H(λ). Now we can write

$$H(\lambda) |\psi(\lambda)\rangle = E(\lambda) |\psi(\lambda)\rangle \tag{6.4}$$

Giving

$$E(\lambda) = \langle \psi(\lambda)| H(\lambda) |\psi(\lambda)\rangle \tag{6.5}$$

Differentiating both sides with λ yields,

$$\frac{\partial E}{\partial \lambda} = \langle \frac{\partial \psi}{\partial \lambda}| H(\lambda) |\psi(\lambda)\rangle + \langle \psi(\lambda)| \frac{\partial H}{\partial \lambda} |\psi(\lambda)\rangle + \langle \psi(\lambda)| H(\lambda) |\frac{\partial \psi}{\partial \lambda}\rangle \tag{6.6}$$

The wave function is assumed to be normalized.

$$\langle \psi(\lambda)|\psi(\lambda)\rangle = 1 \tag{6.7}$$

and

$$H |\psi\rangle = E |\psi\rangle$$

Now eq. (6.6) can be written as,

$$\frac{\partial E}{\partial \lambda} = \langle \psi(\lambda)| \frac{\partial H}{\partial \lambda} |\psi(\lambda)\rangle + E \langle \frac{\partial \psi}{\partial \lambda} |\psi(\lambda)\rangle| + E \langle \psi(\lambda) |\frac{\partial \psi}{\partial \lambda}\rangle| \tag{6.8}$$

$$\frac{\partial E}{\partial \lambda} = \langle \psi(\lambda)| \frac{\partial H}{\partial \lambda} |\psi(\lambda)\rangle + E \frac{\partial}{\partial \lambda} \langle \psi(\lambda)| |\psi(\lambda)\rangle \tag{6.9}$$

using eq. 6.7,

$$\frac{\partial E}{\partial \lambda} = \langle \psi(\lambda)| \frac{\partial H}{\partial \lambda} |\psi(\lambda)\rangle \qquad (6.10)$$

Hence proved

Appendix D

	Capacity (mAh/g)	Diffusion Brrier (eV)	OCV (V)
SiC monolayer with SW	501	0.77	0.1
Graphite	372	0.4	-
MoS_2/Graphene	338	-	2.0
Ti_3C_2 monolayer	320	0.07	0.62
Ψ graphene	372	0.31	0.64
Phosphorene	433	0.76	-
2D-Boron	383	0.66	-
Mo_2C	400-526	0.14-0.15	0.68
VS_2	466	0.22	0.93

Table 6.1: Electrochemical properties of few of the studied anodes of Li-ion batteries.

Appendix E

VASP Input File

#1 Startparameter for this Run:

NWRITE = 2 ! LPETIM=F write-flag & timer

ISTART = 0 ! job : 0-new 1-contEcut 2-sameBS

INIWAV = 1 ! 0-jellium 1-random

IWAVPR = 1 ! prediction: 0-non 1-charg 2-wave 3-comb

ICHARG = 2 ! 0-from WF 1-from CHGCAR 2-from atom 11-12-fixed

LWAVE = .FALSE. ! determines whether the wavefunctions are written to the WAVE-CAR file

#2 Electronic Relaxation

NELM = 100 ! number of iterations

EDIFF = 1E-04 ! stopping-criterion for ELM

BMIX = 3.00 ! sets the cutoff wave vector for Kerker mixing for the magnetization density

ENCUT = 500 ! Cut-Off Energy

#3 Electronic Relaxation

IALGO = 48 ! algorithm for the e-relax

LDIAG = T ! sub-space diagonalisation

LREAL = auto ! real-space projection

PREC = normal ! accuracy

NBANDS = 30 ! number of bands for diagonalization

#4 Ionic Relaxation

NSW = 200 ! number of steps for IOM

NBLOCK = 1 ! inner block

KBLOCK = 10 ! outer block

IBRION = 2 ! ionic relax: 0-MD 1-quasi-New 2-CG

ISIF = 4 ! ion&cell relax: 0-MD 2-ion&stress 3-ion&cell&stress

ISYM = 2 ! switch symmetry stuff ON (1 or 2) or OFF (0)

SYMPREC = 1e-6 !

LCORR = T ! Harris-correction to forces

EDIFFG = -0.04 ! Criterion for geom opt (eV/Ang)

POTIM = 0.50 ! time-step for ionic motion (fs)

SMASS = 3.00 ! Nose mass-parameter (am)

#5 DOS related values

ISMEAR = 0 ! Broadening methode -5-tet -1-fermi 0-gaus 1-mp 2-mp2

SIGMA = 0.05 ! Broadening in eV

LORBIT = 11 ! l-decomposed DOS

RWIGS = 1.63 1.00 ! Wigner-Zeits radius

EMIN = ! Minimum energy for DOS

EMAX = ! Maximum energy for DOS

NEDOS = 1001 ! Number of DOS points

NELECT = 100 ! Total number of electrons

NUPDOWN = 2 ! Difference between UP&DOWN electrons

#6 Parallelizationoption

LPLANE = T ! Parallelization for PWs

NCORE = 8 !

LSCALU = F !

NSIM = 4 !

ISPIN = 1 ! spin polarized = 2, non spin polarized = 1

MAGMOM = 12*0.6 16*0.6 16*0.6 !

#7 optB86b-vdW functional requires vdwkernel.bindat

GGA = MK !

PARAM1 = 0.1234 !

PARAM2 = 1.0000 !

$LUSE_V DW = .TRUE.$!

#$AGGAC = 0.0000$!

#8 TS calculation ! default:Nudged Elestic Band method

ICHAIN = 0 ! Method (0=NEB, 1=Dynamical matrix, 2=Dimer, 3=Lanczos)

SPRING = -5 ! in eV/Ang*2 (sping constant)

IMAGES = 3 ! Number of images btw Reactant & Product

LCLIMB = .true. ! cNEB: driven up to the saddle point

LTANGENTOLD = .true. ! Old central difference tangent

LDNEB = .true. ! Modified doubble nudging

NEBCELL = .true. ! NEB for variable cell (w/ ISIF=3)

#9 Dipole Correctionoption

IDIPOL = 3 !

LDIPOL = !

#10 lda+uparameters

LMAXMIX = 4 !

LDAU = .TRUE. ! or .FALSE.

LDAUTYPE = 2 ! or 1

LDAUL = 2 2 2 !

LDAUU = 0 0 0 !

LDAUJ = 0 0 0 !

#11 vdWcorrections

IVDW = 12

Bibliography

Acun, A., Zhang, L., Bampoulis, P., Farmanbar, M., van Houselt, A., Rudenko, A., Lingenfelder, M., Brocks, G., Poelsema, B., Katsnelson, M., et al. (2015). Germanene: the germanium analogue of graphene. *Journal of physics: Condensed matter*, 27(44):443002.

Ahn, G. H., Amani, M., Rasool, H., Lien, D.-H., Mastandrea, J. P., Ager III, J. W., Dubey, M., Chrzan, D. C., Minor, A. M., and Javey, A. (2017). Strain-engineered growth of two-dimensional materials. *Nature communications*, 8(1):1–8.

Ajayan, P. M. (1999). Nanotubes from carbon. *Chemical reviews*, 99(7):1787–1800.

Ajiki, H. and Ando, T. (1993). Electronic states of carbon nanotubes. *Journal of the Physical Society of Japan*, 62(4):1255–1266.

Akinwande, D., Brennan, C. J., Bunch, J. S., Egberts, P., Felts, J. R., Gao, H., Huang, R., Kim, J.-S., Li, T., Li, Y., et al. (2017). A review on mechanics and mechanical properties of 2d materials—graphene and beyond. *Extreme Mechanics Letters*, 13:42–77.

Anees, P., Valsakumar, M., and Panigrahi, B. (2015). Temperature dependent phonon frequency shift and structural stability of free-standing graphene: a spectral energy density analysis. *2D Materials*, 2(3):035014.

Ashcroft, N. and Mermin, N. (1976). Solid state physics (philadelphia, pa: Saunders).

Baroni, S., Giannozzi, P., and Testa, A. (1987). Green's-function approach to linear response in solids. *Physical Review Letters*, 58(18):1861.

Beaulieu, L., Eberman, K., Turner, R., Krause, L., and Dahn, J. (2001). Colossal reversible volume changes in lithium alloys. *Electrochemical and Solid-State Letters*, 4(9):A137–A140.

Bekaroglu, E., Topsakal, M., Cahangirov, S., and Ciraci, S. (2010). First-principles study of defects and adatoms in silicon carbide honeycomb structures. *Physical Review B*, 81(7):075433.

Bezugly, V., Kunstmann, J., Grundkotter-Stock, B., Frauenheim, T., Niehaus, T., and Cuniberti, G. (2011). Highly conductive boron nanotubes: transport properties, work functions, and structural stabilities. *ACS nano*, 5(6):4997–5005.

Bom, M. and Huang, K. (1954). Dynamical theory of crystal lattices. *Clarendon, Oxford*.

Butler, K. T., Gautam, G. S., and Canepa, P. (2019). Designing interfaces in energy materials applications with first-principles calculations. *npj Computational Materials*, 5(1):19.

Cahangirov, S., Topsakal, M., Aktürk, E., Şahin, H., and Ciraci, S. (2009). Two-and one-dimensional honeycomb structures of silicon and germanium. *Physical review letters*, 102(23):236804.

Ceder, G. (2010). Opportunities and challenges for first-principles materials design and applications to li battery materials. *MRS bulletin*, 35(9):693–701.

Ceperley, D. M. and Alder, B. (1980). Ground state of the electron gas by a stochastic method. *Physical Review Letters*, 45(7):566.

Chabi, S., Chang, H., Xia, Y., and Zhu, Y. (2016). From graphene to silicon carbide: ultrathin silicon carbide flakes. *Nanotechnology*, 27(7):075602.

Cline, C. F. and Sands, D. E. (1960). A new silicon boride, sib4. *Nature*, 185(4711):456.

Combes, J.-M., Duclos, P., and Seiler, R. (1981). The born-oppenheimer approximation. In *Rigorous atomic and molecular physics*, pages 185–213. Springer.

Cooper, R. C., Lee, C., Marianetti, C. A., Wei, X., Hone, J., and Kysar, J. W. (2013). Nonlinear elastic behavior of two-dimensional molybdenum disulfide. *Physical Review B*, 87(3):035423.

Crabtree, G., Glotzer, S., McCurdy, B., and Roberto, J. (2010). Computational materials science and chemistry: accelerating discovery and innovation through simulation-based engineering and science. Technical report, USDOE Office of Science (SC)(United States).

Dahn, J. R., Zheng, T., Liu, Y., and Xue, J. (1995). Mechanisms for lithium insertion in carbonaceous materials. *Science*, 270(5236):590–593.

David, L., Bhandavat, R., and Singh, G. (2014). Mos2/graphene composite paper for sodium-ion battery electrodes. *ACS nano*, 8(2):1759–1770.

Ding, Y. and Wang, Y. (2013). Density functional theory study of the silicene-like six and xsi3 (x= b, c, n, al, p) honeycomb lattices: The various buckled structures and versatile electronic properties. *The Journal of Physical Chemistry C*, 117(35):18266–18278.

Fagan, S. B., Baierle, R., Mota, R., da Silva, A. J., and Fazzio, A. (2000). Ab initio calculations for a hypothetical material: Silicon nanotubes. *Physical Review B*, 61(15):9994.

Fan, X., Zheng, W., and Kuo, J.-L. (2012). Adsorption and diffusion of li on pristine and defective graphene. *ACS applied materials & interfaces*, 4(5):2432–2438.

Fiolhais, C., Nogueira, F., and Marques, M. A. (2003). *A primer in density functional theory*, volume 620. Springer Science & Business Media.

Franco Gonzalez, A., Yang, N.-H., and Liu, R.-S. (2017). Silicon anode design for lithium-ion batteries: progress and perspectives. *The Journal of Physical Chemistry C*, 121(50):27775–27787.

Giannozzi, P., Baroni, S., Bonini, N., Calandra, M., Car, R., Cavazzoni, C., Ceresoli, D., Chiarotti, G. L., Cococcioni, M., Dabo, I., et al. (2009). Quantum espresso:

a modular and open-source software project for quantum simulations of materials. *Journal of physics: Condensed matter*, 21(39):395502.

Golesorkhtabar, R., Pavone, P., Spitaler, J., Puschnig, P., and Draxl, C. (2013). Elastic: A tool for calculating second-order elastic constants from first principles. *Computer Physics Communications*, 184(8):1861–1873.

Goodenough, J. B. and Park, K.-S. (2013). The li-ion rechargeable battery: a perspective. *Journal of the American Chemical Society*, 135(4):1167–1176.

Gori, P., Pulci, O., Marsili, M., and Bechstedt, F. (2012). Side-dependent electron escape from graphene-and graphane-like sic layers. *Applied Physics Letters*, 100(4):043110.

Gui, G., Li, J., and Zhong, J. (2008). Band structure engineering of graphene by strain: first-principles calculations. *Physical Review B*, 78(7):075435.

Guo, G.-C., Wei, X.-L., Wang, D., Luo, Y., and Liu, L.-M. (2015). Pristine and defect-containing phosphorene as promising anode materials for rechargeable li batteries. *Journal of Materials Chemistry A*, 3(21):11246–11252.

Hafner, J. (2000). Atomic-scale computational materials science. *Acta Materialia*, 48(1):71–92.

Haldane, F. D. M. (1988). Model for a quantum hall effect without landau levels: Condensed-matter realization of the" parity anomaly". *Physical Review Letters*, 61(18):2015.

Hansson, A., de Brito Mota, F., and Rivelino, R. (2012). Metallic behavior in low-dimensional honeycomb SiB crystals: A first-principles prediction of atomic structure and electronic properties. *Physical Review B*, 86(19):195416.

Hardikar, R. P., Das, D., Han, S. S., Lee, K.-R., and Singh, A. K. (2014). Boron doped defective graphene as a potential anode material for li-ion batteries. *Physical Chemistry Chemical Physics*, 16(31):16502–16508.

Heine, V. (1970). The pseudopotential concept. In *Solid state physics*, volume 24, pages 1–36. Elsevier.

Henkelman, G., Arnaldsson, A., and Jónsson, H. (2006). A fast and robust algorithm for bader decomposition of charge density. *Computational Materials Science*, 36(3):354–360.

Henkelman, G. and Jónsson, H. (2000). Improved tangent estimate in the nudged elastic band method for finding minimum energy paths and saddle points. *The Journal of chemical physics*, 113(22):9978–9985.

Henkelman, G., Uberuaga, B. P., and Jónsson, H. (2000). A climbing image nudged elastic band method for finding saddle points and minimum energy paths. *The Journal of chemical physics*, 113(22):9901–9904.

Hohenberg, P. and Kohn, W. (1964). Inhomogeneous electron gas. *Physical review*, 136(3B):B864.

Islam, M. S. and Fisher, C. A. (2014). Lithium and sodium battery cathode materials: computational insights into voltage, diffusion and nanostructural properties. *Chemical Society Reviews*, 43(1):185–204.

Jiang, J.-W., Wang, J.-S., and Li, B. (2009). Young's modulus of graphene: a molecular dynamics study. *Physical Review B*, 80(11):113405.

Ju, Z., Xu, L., Pang, Q., Xing, Z., Ma, X., and Qian, Y. (2009). The synthesis of nanostructured sic from waste plastics and silicon powder. *Nanotechnology*, 20(35):355604.

Kochnev, A., Ovid'ko, I., and Semenov, B. (2014). Tensile strength of graphene containing 5-8-5 defects. *Reviews on Advanced Materials Science*, 37.

Kresse, G. and Furthmüller, J. (1996). Efficient iterative schemes for ab initio total-energy calculations using a plane-wave basis set. *Physical review B*, 54(16):11169.

Kresse, G. and Hafner, J. (1993). Ab initio molecular dynamics for liquid metals. *Physical Review B*, 47(1):558.

Kuzubov, A., Eliseeva, N., Krasnov, P., Tomilin, F., Fedorov, A., and Tolstaya, A. (2013). Possibility of a 2d sic monolayer formation on mg (0001) and mgo (111) substrates. *Russian Journal of Physical Chemistry A*, 87(8):1332–1335.

Lee, J. G. (2016). *Computational materials science: an introduction.* Crc Press.

LeSar, R. (2013). *Introduction to computational materials science: fundamentals to applications.* Cambridge University Press.

Li, R., Han, Y., Hu, T., Dong, J., and Kawazoe, Y. (2014). Self-healing monovacancy in low-buckled silicene studied by first-principles calculations. *Physical Review B*, 90(4):045425.

Lin, S. (2012). Light-emitting two-dimensional ultrathin silicon carbide. *The Journal of Physical Chemistry C*, 116(6):3951–3955.

Liu, C.-C., Feng, W., and Yao, Y. (2011). Quantum spin hall effect in silicene and two-dimensional germanium. *Physical review letters*, 107(7):076802.

Liu, F., Shen, C., Su, Z., Ding, X., Deng, S., Chen, J., Xu, N., and Gao, H. (2010). Metal-like single crystalline boron nanotubes: synthesis and in situ study on electric transport and field emission properties. *Journal of Materials Chemistry*, 20(11):2197–2205.

Liu, L., Feng, Y., and Shen, Z. (2003). Structural and electronic properties of h-bn. *Physical Review B*, 68(10):104102.

Manju, M., Ajith, K., and Valsakumar, M. (2018). Strain induced anisotropic mechanical and electronic properties of 2d-sic. *Mechanics of Materials*, 120:43–52.

Meng, Y. S. and Arroyo-de Dompablo, M. E. (2009). First principles computational materials design for energy storage materials in lithium ion batteries. *Energy & Environmental Science*, 2(6):589–609.

Mermin, N. D. and Wagner, H. (1966). Absence of ferromagnetism or antiferromagnetism in one-or two-dimensional isotropic heisenberg models. *Physical Review Letters*, 17(22):1133.

Moissan, H. and Stock, A. (1900). Preparation and properties of two silicon borides: Sib3 and sib6. *CR Acad. Sci.(Paris)*, 131:139–143.

Mortazavi, B., Rahaman, O., Makaremi, M., Dianat, A., Cuniberti, G., and Rabczuk, T. (2017). First-principles investigation of mechanical properties of silicene, germanene and stanene. *Physica E: Low-dimensional Systems and Nanostructures*, 87:228–232.

Mouhat, F. and Coudert, F.-X. (2014). Necessary and sufficient elastic stability conditions in various crystal systems. *Physical Review B*, 90(22):224104.

Nakano, H., Mitsuoka, T., Harada, M., Horibuchi, K., Nozaki, H., Takahashi, N., Nonaka, T., Seno, Y., and Nakamura, H. (2006). Soft synthesis of single-crystal silicon monolayer sheets. *Angewandte Chemie International Edition*, 45(38):6303–6306.

Novoselov, K. S., Geim, A. K., Morozov, S., Jiang, D., Katsnelson, M., Grigorieva, I., Dubonos, S., Firsov, and AA (2005). Two-dimensional gas of massless dirac fermions in graphene. *nature*, 438(7065):197.

Novoselov, K. S., Geim, A. K., Morozov, S. V., Jiang, D., Zhang, Y., Dubonos, S. V., Grigorieva, I. V., and Firsov, A. A. (2004). Electric field effect in atomically thin carbon films. *science*, 306(5696):666–669.

Ozdogan, C., Mukhopadhyay, S., Hayami, W., Guvenc, Z., Pandey, R., and Boustani, I. (2010). The unusually stable b100 fullerene, structural transitions in boron nanostructures, and a comparative study of α-and γ-boron and sheets. *The Journal of Physical Chemistry C*, 114(10):4362–4375.

Pauling, L. and Wilson, E. B. (2012). *Introduction to quantum mechanics with applications to chemistry*. Courier Corporation.

Peng, Q., Ji, W., and De, S. (2012a). Mechanical properties of the hexagonal boron nitride monolayer: Ab initio study. *Computational Materials Science*, 56:11–17.

Peng, Q., Liang, C., Ji, W., and De, S. (2012b). A first principles investigation of the mechanical properties of g-tln. *Model Numer Simul Mater Sci*, 2:76–84.

Peng, Q., Liang, C., Ji, W., and De, S. (2013a). A first principles investigation of the mechanical properties of g-zno: the graphene-like hexagonal zinc oxide monolayer. *Computational Materials Science*, 68:320–324.

Peng, Q., Wen, X., and De, S. (2013b). Mechanical stabilities of silicene. *Rsc Advances*, 3(33):13772–13781.

Perdew, J. P., Burke, K., and Ernzerhof, M. (1996). Generalized gradient approximation made simple. *Physical review letters*, 77(18):3865.

Perdew, J. P., Chevary, J. A., Vosko, S. H., Jackson, K. A., Pederson, M. R., Singh, D. J., and Fiolhais, C. (1992). Atoms, molecules, solids, and surfaces: Applications of the generalized gradient approximation for exchange and correlation. *Physical review B*, 46(11):6671.

Pistoia, G. et al. (1994). *Lithium batteries: new materials, developments and perspectives*, volume 5. Elsevier Amsterdam.

Ponomarenko, L., Schedin, F., Katsnelson, M., Yang, R., Hill, E., Novoselov, K., and Geim, A. (2008). Chaotic dirac billiard in graphene quantum dots. *Science*, 320(5874):356–358.

Roman, R. E. and Cranford, S. W. (2014). Mechanical properties of silicene. *Computational Materials Science*, 82:50–55.

Ryu, J. H., Kim, J. W., Sung, Y.-E., and Oh, S. M. (2004). Failure modes of silicon powder negative electrode in lithium secondary batteries. *Electrochemical and solid-state letters*, 7(10):A306–A309.

Sa, B., Li, Y.-L., Qi, J., Ahuja, R., and Sun, Z. (2014). Strain engineering for phosphorene: the potential application as a photocatalyst. *The Journal of Physical Chemistry C*, 118(46):26560–26568.

Sahin, H., Sivek, J., Li, S., Partoens, B., and Peeters, F. M. (2013). Stone-wales defects in silicene: Formation, stability, and reactivity of defect sites. *Physical Review B*, 88(4):045434.

Saito, T. (2013). *Computational materials design*, volume 34. Springer Science & Business Media.

Semenoff, G. W. (1984). Condensed-matter simulation of a three-dimensional anomaly. *Physical Review Letters*, 53(26):2449.

Setiadi, J., Arnold, M. D., and Ford, M. J. (2013). Li-ion adsorption and diffusion on two-dimensional silicon with defects: a first principles study. *ACS applied materials & interfaces*, 5(21):10690–10695.

Shemella, P., Zhang, Y., Mailman, M., Ajayan, P. M., and Nayak, S. K. (2007). Energy gaps in zero-dimensional graphene nanoribbons. *Applied Physics Letters*, 91(4):042101.

Shevlin, S. and Guo, Z. (2007). Hydrogen sorption in defective hexagonal bn sheets and bn nanotubes. *Physical Review B*, 76(2):024104.

Shi, Z., Zhang, Z., Kutana, A., and Yakobson, B. I. (2015). Predicting two-dimensional silicon carbide monolayers. *ACS nano*, 9(10):9802–9809.

Shinde, P. P. and Kumar, V. (2011). Direct band gap opening in graphene by bn doping: Ab initio calculations. *Physical Review B*, 84(12):125401.

Splendiani, A., Sun, L., Zhang, Y., Li, T., Kim, J., Chim, C.-Y., Galli, G., and Wang, F. (2010). Emerging photoluminescence in monolayer mos2. *Nano letters*, 10(4):1271–1275.

Stone, A. J. and Wales, D. J. (1986). Theoretical studies of icosahedral c60 and some related species. *Chemical Physics Letters*, 128(5-6):501–503.

Sun, Q., Dai, Y., Ma, Y., Jing, T., Wei, W., and Huang, B. (2016). Ab initio prediction and characterization of mo2c monolayer as anodes for lithium-ion and sodium-ion batteries. *The journal of physical chemistry letters*, 7(6):937–943.

Sun, X., Wang, Z., and Fu, Y. Q. (2015). Defect-mediated lithium adsorption and diffusion on monolayer molybdenum disulfide. *Scientific reports*, 5:18712.

Susi, T., Skákalová, V., Mittelberger, A., Kotrusz, P., Hulman, M., Pennycook, T. J., Mangler, C., Kotakoski, J., and Meyer, J. C. (2017). 2d silicon carbide: computational insights and the observation of sic nanograin assembly. *arXiv preprint arXiv:1701.07387*.

Tang, H. and Ismail-Beigi, S. (2007). Novel precursors for boron nanotubes: the competition of two-center and three-center bonding in boron sheets. *Physical review letters*, 99(11):115501.

Tang, H. and Ismail-Beigi, S. (2010). First-principles study of boron sheets and nanotubes. *Physical Review B*, 82(11):115412.

Tang, Q., Zhou, Z., and Shen, P. (2012). Are mxenes promising anode materials for li ion batteries? computational studies on electronic properties and li storage capability of ti3c2 and ti3c2x2 (x= f, oh) monolayer. *Journal of the American Chemical Society*, 134(40):16909–16916.

Thomas, S., Ajith, K., Chandra, S., and Valsakumar, M. (2015). Temperature dependent structural properties and bending rigidity of pristine and defective hexagonal boron nitride. *Journal of Physics: Condensed Matter*, 27(31):315302.

Thomas, S., Jung, H., Kim, S., Jun, B., Lee, C. H., and Lee, S. U. (2019). Two-dimensional haeckelite h567: A promising high capacity and fast li diffusion anode material for lithium-ion batteries. *Carbon*, 148:344–353.

Thomas, S., Madam, A. K., and Zaeem, M. A. (2020). Stone–wales defect induced performance improvement of bc3 monolayer for high capacity lithium-ion rechargeable battery anode applications. *The Journal of Physical Chemistry C*, 124(11):5910–5919.

Thomas, S. and Zaeem, M. A. (2020). A new planar bcn lateral heterostructure with outstanding strength and defect-mediated superior semiconducting to metallic properties. *Physical Chemistry Chemical Physics*, 22(38):22066–22077.

Tian, W., Li, W., Yu, W., and Liu, X. (2017). A review on lattice defects in graphene: types, generation, effects and regulation. *Micromachines*, 8(5):163.

Ting, T. and Chen, T. (2005). Poisson's ratio for anisotropic elastic materials can have no bounds. *The quarterly journal of mechanics and applied mathematics*, 58(1):73–82.

Tomanek, D., Wentzcovitch, R. M., Louie, S. G., and Cohen, M. L. (1988). Calculation of electronic and structural properties of bc 3. *Physical review B*, 37(6):3134.

Topsakal, M., Cahangirov, S., Bekaroglu, E., and Ciraci, S. (2009). First-principles study of zinc oxide honeycomb structures. *Physical Review B*, 80(23):235119.

Voon, C., Lim, B., Gopinath, S., Tan, H., Tony, V., Arshad, M. M., Foo, K., and Hashim, U. (2016). Green synthesis of silicon carbide nanowhiskers by microwave heating of blends of palm kernel shell and silica. In *IOP Conference Series: Materials Science and Engineering*, volume 160, page 012057. IOP Publishing.

Wallace, P. R. (1947). The band theory of graphite. *Physical Review*, 71(9):622.

Wang, H., Cao, J., Huang, X., and Huang, J. (2012a). Pressure dependence of elastic and dynamical properties of zinc-blende zns and znse from first principle calculation. *arXiv preprint arXiv:1204.6102*.

Wang, H., Cao, J., Huang, X., and Huang, J. (2012b). Pressure dependence of elastic and dynamical properties of zinc-blende zns and znse from first principle calculation. *Condensed Matter Physics*, 15.

Wang, H., Li, Q., Gao, Y., Miao, F., Zhou, X.-F., and Wan, X. (2016a). Strain effects on borophene: ideal strength, negative possion's ratio and phonon instability. *New Journal of Physics*, 18(7):073016.

Wang, N., Tian, Y., Zhao, J., and Jin, P. (2016b). Co oxidation catalyzed by silicon carbide (sic) monolayer: A theoretical study. *Journal of Molecular Graphics and Modelling*, 66:196–200.

Wang, R., Wang, S., Wu, X., and Liang, X. (2010). First-principles calculations on third-order elastic constants and internal relaxation for monolayer graphene. *Physica B: Condensed Matter*, 405(16):3501–3506.

Wang, S., Yang, B., Yuan, J., Si, Y., and Chen, H. (2015). Large-scale molecular simulations on the mechanical response and failure behavior of a defective graphene: cases of 5–8–5 defects. *Scientific reports*, 5:14957.

Wu, L. and Zhang, J. (2015). Ab initio study of anisotropic mechanical properties of licoo2 during lithium intercalation and deintercalation process. *Journal of Applied Physics*, 118(22):225101.

Yan, J.-A., Gao, S.-P., Stein, R., and Coard, G. (2015). Tuning the electronic structure of silicene and germanene by biaxial strain and electric field. *Physical Review B*, 91(24):245403.

Yu, M., Jayanthi, C., and Wu, S. (2009). Bonding nature, structural optimization, and energetics studies of sic graphitic-like layer structures and single/double walled nanotubes. *arXiv preprint arXiv:0901.3567*.

Zhang, A.-X., Liu, J.-T., Guo, S.-D., and Li, H.-C. (2017). Strain effects on phonon transport in antimonene investigated using a first-principles study. *Physical Chemistry Chemical Physics*, 19(22):14520–14526.

Zhang, P., Ma, L., Fan, F., Zeng, Z., Peng, C., Loya, P. E., Liu, Z., Gong, Y., Zhang, J., Zhang, X., et al. (2014). Fracture toughness of graphene. *Nature communications*, 5:3782.

Zhao, J., Wen, B., Zhou, Z., Chen, Z., and von Ragué Schleyer, P. (2005). Reduced li diffusion barriers in composite bc3 nanotubes. *Chemical physics letters*, 415(4-6):323–326.

Zhao, S., Kang, W., and Xue, J. (2014). The potential application of phosphorene as an anode material in li-ion batteries. *Journal of Materials Chemistry A*, 2(44):19046–19052.

Zou, G., Dong, C., Xiong, K., Li, H., Jiang, C., and Qian, Y. (2006). Low-temperature solvothermal route to 2h–sic nanoflakes. *Applied physics letters*, 88(7):071913.

LIST OF PUBLICATIONS

MANUSCRIPTS IN PEER-REVIEWED JOURNALS

- Manju, M. S., Ajith, K. M. and Valsakumar, M.C. (2018). "Strain dependent anisotropic mechanical and electronic properties of 2D-SiC". Mechanics of Materials, 120: 43–52.

- Manju, M. S., Siby Thomas, Anees, C., Sang Uck Lee and Ajith, K. M. (2020) "Strain induced structural transformation, mechanical and phonon stability in silicene derived 2D-SiB". Journal of Industrial and Engineering Chemistry, 90, 399–406.

- Siby Thomas, Manju, M. S., Ajith, K. M. Sang Uck Lee and Mohsen Asle Zaeem (2020) "Strain-induced work function in h-BN and BCN monolayers". Physica E: Low-dimensional Systems and Nanostructures, 123, 114180-114188.

- Manju, M. S., Siby Thomas, Sang Uck Lee and Ajith, K. M. (2020) "Mechanically Robust, Self Healing Graphene like Defective SiC : A Prospective Anode of Li-ion Batteries". Applied Surface Science, 541, 148417.

- Manju, M. S. and Ajith, K. M. "Anisotropic elastic properties of silicene derived layered material SiC". Submitted.

MANUSCRIPTS IN INTERNATIONAL CONFERENCE PROCEEDINGS

- Manju, M.S., Ajith, K.M. and Valsakumar, M.C. (2018). "Uniaxial Stress Induced Band Structure Changes in h-SiB". AIP Conference Proc., 1953(1): 110027.

- Manju, M.S., Harikrishnan, G. , Ajith, K.M. and Valsakumar, M.C. (2014). "Effect of pressure on the band structure of BC3". AIP Conference Proc., 1731(1): 090015.

PAPERS PRESENTED IN INTERNATIONAL CONFERENCES

- Manju, M.S., Ajith, K.M. and Valsakumar, M.C., "Uniaxial Stress Induced Band Structure Changes in h-SiB"., 2nd International Conference on Condensed Matter & Applied Physics, Govt. Engineering College, Bikaner, Rajasthan, November 24-25, 2017.

- Manju, M.S. and Ajith, K.M., "Mechanical stability and third order elastic constants of BSi_3", International Conference on Advances in Functional Materials, Anna University, Chennai, India, January 6–8, 2017.

- Manju, M.S., Harikrishnan, G., Ajith, K.M. and Valsakumar, M.C., "Effect of Pressure on the Band Structure of BC3", 60th DAE–Solid state physics symposium, Amity University, Noida, Uttar Pradesh, India, December 21–25, 2015. (Oral presentation).

CURRICULUM VITAE

MANJU M S

Permanent Address :

Chengala Variam, (PO) Ramanthali,   Mobile:(+91)-8762246248

Kannur Dist,   E-mail: mm.ph13f02@nitk.edu.in,

Kerala, India-670308   manju0manju@gmail.com.

Academic Qualifications :

Master of Science   Score : 72%
Bangalore University

Bachelor of Science   Score : 89.2%
Kannur University

Research Publications :

Articles in International Journals : 4

Articles in International Proceedings : 2

Papers presented in International Conferences : 3